Title
Quantifying Contributions to Pyroelectricity in Thin-Film Ferroelectric Oxides

Author
Velarde, Gabriel

Publication Date
2020

Peer reviewed|Thesis/dissertation

Quantifying Contributions to Pyroelectricity in Thin-Film Ferroelectric Oxides

by

Gabriel Velarde

A dissertation submitted in partial satisfaction of the

requirements for the degree of

Doctor of Philosophy

In

Engineering-Materials Science and Engineering

in the

Graduate Division

of the

University of California, Berkeley

Committee in charge:

Professor Lane W. Martin, Chair

Professor Ramamoorthy Ramesh

Professor Chris Dames

Fall 2020

Quantifying Contributions to Pyroelectricity in Thin-Film Ferroelectric Oxides

Gabriel Velarde

Abstract

Quantifying Contributions to Pyroelectricity in Thin-Film Ferroelectric Oxides

by

Gabriel Velarde

Doctor of Philosophy in Materials Science and Engineering

University of California, Berkeley

Professor Lane W. Martin, Chair

The field of material science and engineering aims to provide interdisciplinary communities with the physical understanding and control of various material structures and properties to allow for the development of advanced material systems and technology. Key to the developments of ubiquitous energy conversion, enhanced computer logic and memory performance, and artificial intelligence lies an increasing demand for highly-susceptible, next-generation materials which maintain unique functional ability under applied thermal, mechanical, and electrical stimuli. One such class of functional materials poised to address these needs are thin-film, complex-polar oxides which maintain a rich landscape of electromechanical, thermoelastic, and electrothermal properties. As such, although developments in the fields of dielectrics, piezoelectrics, and ferroelectrics have followed, the field of pyroelectrics (*i.e.*, electrothermal response) has remained relatively understudied. Due to the complex material property intercoupling of pyroelectricity to dielectric, ferroelectric, and piezoelectric counterparts, identifying routes to understand and enhance the various contributions to pyroelectric response has continued to limit the field. As a result, pyroelectrics have remained primarily stagnant in the past 30 years, limited to applications only in IR sensor array technology. Without the proper understanding and control of the various material properties that contribute to the overall pyroelectric response needed for enhanced performance in next-generation applications (*e.g.*, waste-heat energy conversion), researchers have traditionally defaulted to perching pyroelectric systems near material phase transitions. Specifically, proximity to the Curie transition temperature (T_C) typically allows for the overall enhancement of pyroelectric response, however, at the cost of small operating temperature windows and increased DC, background temperatures. In this Dissertation, I aim to elucidate the various contributions to pyroelectricity via comprehensive and direct characterization methodologies and provide the community with accessible routes for overall pyroelectric response enhancement. I aim to show that these coupled material properties do not simply follow design rules established in the fields of ferroelectric and piezoelectric materials, and thus require an unintuitive understanding of their interactions.

In this work, I provide various insights into the complex pyroelectric property interplay in prototypical $PbZr_xTi_{1-x}O_3$ and $BaTiO_3$ thin-film ferroelectric oxides. With careful consideration of applied electric fields, temperature oscillations, and device geometry, I show that

pyroelectric contributions may be individually suppressed and decoupled to provide quantitative understanding in overall pyroelectric response. With the engineering of domain architectures in $PbZr_xTi_{1-x}O_3$ systems via underlying substrates, the evolution of ferroelectric, dielectric, and pyroelectric response is investigated to understand and quantify ferroelastic-domain contributions. Typically disregarded in the past, I demonstrate that these subtle extrinsic contributions may account for as much as 35% of the total measured pyroelectric response at room temperature for some films. Furthermore, through the use of applied, high-DC electric fields, I can systematically suppress these extrinsic contributions to understand the evolution of pyroelectric response across the morphotropic boundary of $PbZr_xTi_{1-x}O_3$. Lastly, with the fabrication and synthesis of in-plane electrothermal test platforms and high-quality $BaTiO_3$ thin-films on Si substrates, I systematically investigate the evolution of elastic boundary conditions on the extrinsic and secondary contributions to pyroelectricity. Through the quantification of the various pyroelectric contributions, I more clearly depict the underlying property complexities that have long hindered advancements in the field of pyroelectrics.

To the Velarde Family

Acknowledgments

In chronological order, I'd like to thank the various individuals and parties that have helped mold my academic career.

First, I'd like to thank both my parents, Jose and Daina Velarde, for their continual dedication in the development of my academic studies since my early childhood. They have shown me the rewards of patience, hard work, and self-discipline. Additionally, I'd like to acknowledge all my aunts, uncles, and grandparents that have not only helped me in school but acted as role models for the achievement of higher education.

Additionally, I'd like to thank the Society of Hispanic Professional Engineers (SHPE) for connecting me with my first undergraduate research role during my B.S. degree at the University of Illinois at Urbana-Champaign. This pivotal opportunity allowed me to explore the world of ferroelectrics and inevitably obtain a position here at the University of California, Berkeley. I am eternally grateful for the immense academic and personal support system that SHPE provided me during my rigorous material science and engineering degree.

As my first graduate mentor, I'd like to thank Josh C. Agar for his continuous determination and support of my expertise in the field of complex ferroelectric oxides, both at the undergraduate and graduate level. He has guided me through numerous years of experimental and academic challenges.

I would like to thank Shishir Pandya for all his efforts in the development of my understanding and capabilities in the field of pyroelectrics. For the countless hours spent explaining pyroelectric physics and characterization protocol, I am grateful to have learned from such a knowledgeable individual.

With my time at the University of California, Berkeley, I'd like to thank all past and current members of the Professor Ramesh and Martin research groups. They provided me with a high-performance environment that allowed me to accomplish my research thrusts. A special thanks to David Garcia, Arvind Dasgupta, and Jieun Kim for their extensive interest and support of my work over the years.

Additionally, I'd like to thank Professor Chris Dames, Jason Wu, and Joshua D. Wilbur of the Mechanical and Engineering Department for their crucial expertise in heat transfer, FEA analysis, and microfabrication.

Furthermore, I would like to thank the National Science Foundation and the Army Research Office for their monetary support of my research focuses for over three years of my Ph.D.

I would also like to thank my soon-to-be wife, Brooke, for her continued support during my Ph.D. She has reminded me to maintain a healthy work life balance, and enjoy the simpler, and slower things in life.

Finally, I would like to thank my Ph.D. research advisor, Professor Lane W. Martin, for his invaluable guidance during my undergraduate and graduate career. His attention to detail, scientific integrity, work-ethic, and expertise has consistently challenged me during our time together. Thanks to professor Martin, I have quickly grown into an efficient and thoughtful researcher that now has the skillsets to take on increasingly challenging research thrusts.

Work in this Ph.D. has been supported, in part, by the Army Research Office under Grant W911NF-14-1-0104, the National Science Foundation under via the National Science Foundation Graduate Research Fellowship and under grants DMR-1451219 and DMR-1708615, and the U.S. Department of Energy, Office of Science, Office of Basic Energy Sciences, Materials Sciences and Engineering Division under Contract No. DE-AC02-05-CH11231 (Materials Project program KC23MPfor the development of functional oxide materials and under Award Number DE-SC-0012375 for the development of thin-film ferroelectrics.

Table of Contents

LIST OF FIGURES

Figure 4.9: a) PE hysteresis loops for the various heterostructures. b) Frequency dependence of the dielectric permittivity (left axis) and loss tangent (right axis) for the various heterostructures. Brown, orange, yellow, light green and dark green refer to $TbScO_3$, $GdScO_3$, $SmScO_3$, $NdScO_3$, and $PrScO_3$, respectively.

Figure 4.10: a) Frequency dependence of the pyroelectric coefficient for the variously strained heterostructures. b) DC-bias dependence of the pyroelectric coefficient across the various strain states, depicting traditional "butterfly" loop switching and dielectric contributions to pyroelectricity at increasing fields. c) Theoretically calculated intrinsic (black dashed line) and intrinsic + extrinsic (red open circles) contributions to pyroelectricity as a function of strain. d) Independently plotted magnitude and sign of the extrinsic contribution to pyroelectricity as a function of strain. e) Normalized pyroelectric coefficient as a function of temperature for the various heterostructures at 1 kHz and 0V DC bias.

Figure 5.1: Structural measurements of $PbZr_{1-x}Ti_xO_3$ heterostructures. (a) X-Ray diffraction line scans of x = 0.40, 0.48, and 0.60 heterostructures (bottom to top) about the $GdScO_3$ 220-diffraction condition. Insets display the respective atomic force microscopy surface morphology.

Figure 5.2: (a) Representative X-Ray reflectivity results for x = 0.48 heterostructures. Indicated thickness (t) used for growth rate characterization. (b) Wide angle $\theta - 2\theta$ line scans for as-grown x = 0.60 and x = 0.48, and post-device processed x = 0.40. An expected Pt (111) peak is found due to Pt deposited electrodes and heaters, see single layer $Pt/GdScO_3$ in black for reference. Reciprocal space mapping studies about the off-axis 332-diffraction condition of (c) x = 0.40, (d) x = 0.48, and (e) x = 0.60 heterostructures. The red dashed lines indicate coherently strained in-plane lattice parameter peak positions. (f) Measured dielectric permittivity response under applied dc-electric fields at 1 kHz. (g) Room temperature ferroelectric hysteresis response for the various compositions measured at 1 kHz. (h) Current-voltage response for the various compositions measured on 6.2E-5 cm^2 device areas.

Figure 5.3: Thermal and *secondary* measurements of $PbZr_{1-x}Ti_xO_3$ thin-films. (a) Calculated thermal penetration depth into the $GdScO_3$ substrate used to define the cut-off frequency for secondary contributions. Inset displays a schematic of the heat flux through the thin-film stack where the heater half width is approached at 1 kHz. (b) Temperature oscillation amplitude (left axis) and associated thermal phase lag (right axis) within the ferroelectric film as a function of heating frequency 1ω. (c) Frequency dependence of the π displaying a suppressed *secondary* effect past ~1 kHz.

Figure 5.4: Extraction of the dielectric contribution to π. (a) Prototypical temperature dependence of the dielectric permittivity under applied dc-electric (*E*) fields. (b) Summary of the temperature dependent (23°C, 33°C, and 42°C) ε_r results as a function of applied dc-electric field for all heterostructures (Inset displays magnified results at low fields for x = 0.48). (c) Extracted temperature derivative of ε_r as a function of applied dc bias for the various

heterostructures. (d) Calculated *dielectric* contributions as a function of field (*i.e.*, $\pi_\varepsilon = \varepsilon_0 E \frac{\partial \varepsilon_r(E)}{\partial T}$) for all heterostructures; note all start at zero applied field.

Figure 5.5: Pyroelectric and *intrinsic* DC field dependence of $PbZr_{1-x}Ti_xO_3$ heterostructures. (a) Applied DC-electric-field response of room temperature pyroelectric currents measured at 1 kHz and 10 mA rms heating current. Heating powers for x = 0.40 and 0.48 are scaled to the applied power used for the x = 0.60 and 0.80 heterostructures due to different heater-line resistances. (b) Pyroelectric coefficient results under applied DC bias for the various compositions measured at 1 kHz. (c) *Intrinsic* contribution extraction and DC-electric-field dependence from high-field π. Here, α_i and π_{int} refer to the slope and zero-field value of the field-dependent *intrinsic* contribution.

Figure 5.6: Extraction of the various contributions to π for $PbZr_{1-x}Ti_xO_3$ heterostructures. (a) DC-field dependence of the total π and extracted *extrinsic*, *dielectric*, and *intrinsic* π contributions for x = 0.80 heterostructures. Summarized DC-electric field response of the *intrinsic, dielectric, extrinsic,* and *total* π for (b) x = 0.60, (c) x = 0.48, and (d) x = 0.60 heterostructures. Previously calculated *dielectric* contributions (Figure 5.4d) have been smoothed to reduce noise from measured permittivity results. (e) Summary of the *intrinsic*, *extrinsic*, *secondary*, and total π response as a function of composition across the various $PbZr_{1-x}Ti_xO_3$ chemistries studied herein. Due to the opposing signs of the various contributions, the total net π value is indicated via a solid line for each composition. The *dielectric* contribution displayed here is that measured at an applied dc-electric field of 100 kV cm^{-1}.

Figure 6.1: Phase-field model depicting the polarization direction and phase interconversion (*i.e.*, a_1/a_2 to polar vortex) region within $PbTiO_3/SrTiO_3$ superlattice.

Figure 6.2: a,b,c) X-ray line scans about the $SrTiO_3$ 002, $DyScO_3$ 220, and $SmScO_3$ 220 diffraction condition, respectively. Insets indicate peak locations of the substrate and $PbTiO_3$ thin-film. Additionally, blue and green dashed vertical lines indicate the theoretical bulk and respective strained condition on each substrate.

Figure 6.3: a,b,c) Reciprocal space maps about the $SrTiO_3$ 002, $DyScO_3$ 110, and $SmScO_3$ 110 diffraction condition, respectively. Insets indicate peak locations of the substrate and $PbTiO_3$ thin-film domain structures.

Figure 6.4: a, b, c) Vertical amplitude PFM response from 100-nm-thick $PbTiO_3$ thin-films grown on $SrTiO_3$, $DyScO_3$, and $SmScO_3$ substrates, respectively. d, e, f) Corresponding lateral amplitude PFM response of the $PbTiO_3$ thin-films grown on $SrTiO_3$, $DyScO_3$, and $SmScO_3$ substrates, respectively.

Figure 6.5: a) Top view and b) Cross-sectional view of a typical IDE structure. Here L, D, S, and h refer to center-to-center IDE finger spacing, finger-to-finger spacing, finger width, and film thickness, respectively.

Figure 6.14: a) X-ray diffraction line scan of $BaTiO_3/SrRuO_3$ tri-layer heterostructures grown on 20 nm $SrTiO_3$-buffered Si (001) substrates. b) Polarization-electric field hysteresis loops taken at 1 kHz excitation frequency c) Dielectric permittivity (left axis) and respective loss tangent δ (right axis) under 5 mV AC sensing signal.

Figure 6.15: a) Pyroelectric current as a function of DC bias b) Frequency dependence of π between 5-1000 Hz applied AC heating current frequency and linearly extrapolated secondary pyroelectric contribution. c) DC bias response of π at 1 kHz AC heating current frequency.

Figure 6.16: a) 3-dimensional schematic of the standard electrothermal test platform used in this study and integrated silicon-based etch pit to partially release the pyroelectric center beam. b) Corresponding cross sectional view of the heterostructure and under-etch silicon region.

Figure 6.17: a) Optical images of the developed photoresist mask displaying an exposed Si substrate window. b) Post-XeF_2 Si etch after 7 cycles c) Profilometer height line profile (red dashed line Figure 2b) through the Si etch pit across the pyroelectric test platform. d) SEM image of fully under etched pyroelectric beam. e) Ferroelectric temperature oscillation amplitude as a function of heating current frequency and number of XeF_2 under etch cycles.

LIST OF ABBREVIATIONS

AC	Alternating Current
DC	Direct Current
GLD	Ginzburg Landau Devonshire
MPB	Morphotropic Phase Boundary
PFM	Piezoresponse Force Microscopy
PLD	Pulsed Laser Deposition
TCR	Temperature Coefficient of Resistance

LIST OF SYMBOLS

A	Capacitor Area
D	Dielectric Displacement
d	Film Thickness
d_{ijk}	Piezoelectric Coefficient
E	Electric Field
ε_0	Permittivity of free space
ε_r	Relative Permittivity
I	Electrical Current
J	Current Density
λ	Thermal Penetration Depth
π	Pyroelectric Coefficient
P	Polarization
P_S	Spontaneous Polarization
R	Resistance
T	Temperature
T_C	Curie Temperature
t	time
V	*Voltage*
$V_{3\omega}$	3-Omega Voltage
x	Mechanical Strain
X	Mechanical Stress

CHAPTER 1

Motivation and Outline

This Chapter aims to provide the motivation, goals, and layout of this Dissertation. It aims to stress the importance of the development of the field of pyroelectrics via the understanding of its various contributions and provides the reader with avenues to expand the potential of pyroelectrics into applications such as next-generation waste-heat energy conversion technology. Lastly, the overarching questions and organization of this Dissertation are provided.

1.1 Motivation

Next generation waste-heat energy conversion will require complex functional materials that can efficiently convert heat from a wide range of temperatures, frequencies, and sources. Among the various thermal conversion materials, pyroelectrics, specifically thin-film ferroelectric oxides, have experienced renewed interest due their record-breaking response in thin-film geometries [1]. Unlike conventional thermal-conversion materials (*e.g.*, thermoelectrics) that require competing thermal and electrical conductivities, the maintenance of large spatial temperature gradients, and careful consideration of thermal contacts [2-5], pyroelectrics operate on different design principles. In contrast, pyroelectrics require a time-varying thermal stimulus, and are dependent on device area, rather than material volume which often limits thin-film thermoelectric performance [6,7]. With the increased magnitude of temperature variations and frequency of the oscillations achievable in thin-film pyroelectrics, energy/power densities, and Carnot efficiencies can more readily be made to approach those of modern thermoelectric systems, perhaps allowing for the incorporation of pyroelectrics into thin-film technology such as on-chip, low-grade heat conversion and cooling.

Despite these promising advantages, pyroelectrics do suffer from various limitations. Specifically, there is a lack of understanding in the deterministic control and enhancement of pyroelectric response. Historically, the community has relied on the design rules set and developed by researchers work on dielectric and piezoelectric materials. Following design protocols therein, researchers have situated related pyroelectrics near structural phase instabilities such as the Curie Temperature (T_C), where large dielectric and piezoelectric susceptibilities are readily achieved [8-10]. Although proven to enhance pyroelectric and electrocaloric response, operation at the T_C provides an extremely narrow window of approximately 10-20°C range before the performance sharply falls off. Additionally, T_C for many ferroelectric oxides remain at elevated temperatures which makes application of such energy-conversion materials, specifically for low-grade waste heat, highly inefficient and unstable due to effects of thermal and electrical degradation [11-13].

In order to address these shortcomings, researchers have turned to phenomenological modeling, specifically, Ginsburg-Landau-Devonshire (GLD) models to elucidate pyroelectric response in thin-film systems of various composition, temperatures, and mechanical boundary conditions [14-16]. Although qualitatively insightful, these models are limited to relatively simple systems in which complex domain and defect interactions cannot be sufficiently incorporated. Additionally, GLD modeling requires accurate temperature-dependent values for complex material tensors (*e.g.*, thermal expansion, piezoelectric, elastic compliance etc.) and relatively high-symmetry crystal geometries. Although these models have provided researchers with increased understanding of the various contributions to pyroelectricity, the numerous material property input uncertainties carry error into the models that often mask the complex interplay of contributions in real systems. To further complicate matters, unlike conventional piezoelectric and ferroelectrics, pyroelectrics maintain contributions of not only various magnitudes, but also signs. These tightly coupled, competing contributions, drastically complicate and obscure defined design rules for

enhancing pyroelectric response and are often found in direct contradiction among various reports [17-20].

Furthermore, a lack of unified experimental protocols within the pyroelectric community has often diluted reported findings and promoted large discrepancies in material performance. This is particular troublesome in thin-film materials, where the lack of comprehensive methodologies stem from accurately applied temperature magnitudes and characterization, unaccounted for, spurious, thermally stimulated responses, and bulk and thin-film boundary conditions. From early dynamic and static methodologies [21-23], more than 20 techniques have developed that utilize various excitations and measured signals to extract and estimate pyroelectric response. Only recently have dynamic, periodic heating techniques begun to address and explore the shortcomings of previously established methods, specifically for thin-film geometries [24,25].

In order to quantitively understand pyroelectricity, in addition to the complex interplay of its numerous contributions, a comprehensive study that can accurately and independently suppress these contributions is needed. In this Dissertation, I will use a combination of heating frequency, DC electric fields, and device geometries of electrothermal test platforms to directly elucidate these contributions and provide the community with routes to enhance the overall response while minimizing inevitable material property tradeoffs. Through the evolution of composition across $PbZr_{1-x}Ti_xO_3$ phase instabilities and $BaTiO_3$ mechanical boundary conditions of under-etched substrates, I develop a comprehensive methodology that can accurately decouple and quantify both magnitude and sign of individual contributions.

1.2 Central Questions and Layout of the Dissertation

This Dissertation focuses on the understanding and quantification of various contributions to pyroelectricity in thin-film ferroelectric oxide systems. Specifically, the following goals are established:

1. Understand the sign and magnitude of extrinsic contributions arising from ferroelectric domain structures across various strain states and compositions.
2. Investigate the contribution of secondary effects arising from thermally driven shape changes and thermal-expansion mismatch with substrates via the relaxation of clamped boundary conditions imposed by an underlying substrate.
3. Utilize key insights from the understanding of these pyroelectric contributions to provide guidance on the design of materials with high-performance properties and to enhance pyroelectric waste-heat energy conversion performance.

In this regard, the following chapters will make up the remainder of this dissertation, including: *Chapter 2* which provides an introduction to the field of pyroelectricity and specifically covers aspects of material physics, pyroelectric devices and materials, waste-heat energy conversion, and thin-film epitaxial ferroelectrics. *Chapter 3* then introduces the synthesis of thin-film pyroelectrics *via* pulsed laser deposition in addition to the microfabrication processes used to produce the electrothermal-test platforms. This Chapter also explores the structural, electrical, temperature, and pyroelectric characterization

methods. From there, *Chapter 4* provides an introduction into so-called intrinsic and extrinsic contributions to dielectric, piezoelectric, and ferroelectric susceptibilities. Additionally, routes to control and measure the extrinsic contributions to properties are discussed. Furthermore, this Chapter begins the investigation of extrinsic contributions in pyroelectric systems. Specifically, this Chapter focuses on the study of various ferroelectric domain architectures in the $PbZr_{1-x}Ti_xO_3$ system that determine the extrinsic contributions to pyroelectricity in thin-film heterostructures. With use of a reference mono-domain film, differences between overall measured dielectric, ferroelectric, and pyroelectric response are attributed to the temperature evolution of out-of-plane oriented *c* domains and the in-plane oriented *a* - domains. By controlling both the magnitude and sign of the extrinsic contribution, the overall pyroelectric response can be maximized. Building from this, *Chapter 5* dives further into the elaboration of additional contributions to the total pyroelectric response, including: secondary, dielectric, and intrinsic contributions to pyroelectricity which are studied within various compositions across the morphotropic phase boundary of $PbZr_{1-x}Ti_xO_3$. Through the use of high-DC electric fields and high-frequency heating, the various contributions can be independently suppressed to accurately provide quantification of the various contributions without the need for reference materials with specific domain architectures. *Chapter 6* then discusses the study of in-plane pyroelectric response and extrinsic contributions from various *a* domain configurations in thin-film $PbTiO_3$ heterostructures. Additionally, I introduce the feasibility of PLD-based, $BaTiO_3$ growth upon silicon substrates, wherein high crystallinity and robust ferroelectric properties can be replicated without the need for non-CMOS compatible rare-earth scandate substrates. Through the use of an XeF_2 dry etch, the underlying silicon can be systematically removed from under the $BaTiO_3$ electrothermal test platform to relax the elastic boundary conditions from the substrate. Finally, *Chapter 7* summarizes the findings of this Dissertation, with emphasis on not only the comprehensive pyroelectric contribution extraction methodology developed, but additionally the various insights obtained for enhancing overall pyroelectric susceptibility. Furthermore, future work is proposed in regards to the continued investigation of in-plane pyroelectric response of tensile strained $PbTiO_3$ and more complex systems such as the novel polar vortex superlattices [26]. Finally, the main text is supported by Appendix A and B which provide further discussion on PLD synthesis of $PbZr_{1-x}Ti_xO_3$ and $BaTiO_3$ systems, respectively.

CHAPTER 2

Introduction to Pyroelectricity: Definitions, Properties, and Materials

This Chapter serves to introduce pyroelectricity from both a theoretical, thermodynamic, and experimental perspective. Here, I will discuss the origins of not only pyroelectricity, but of ferroelectric and piezoelectric effects to provide a comprehensive overview of the respective material properties important to this work. Furthermore, I provide introductions to the thin-film material systems constituting most of the work in my dissertation, in addition to their respective properties and applications. Finally, I discuss pyroelectric materials in waste-heat energy technology and the associated limitations and difficulties of implementation.

2.1 Basic Definitions

Among the numerous coupled mechanical, electrical, and thermal material susceptibilities, pyroelectricity defines the thermodynamic intensive-extensive relationship between electrical polarization and temperature, respectively (Figure 2.1a) [1,2]. As such, pyroelectricity is depicted *via* the first rank pyroelectric coefficient tensor (Eq. 2.1),

$$\pi_i = \frac{\delta P_{S_i}}{\delta T} \qquad \text{(Eq. 2.1)}$$

which establishes the thermodynamic temperature (T) dependence of the spontaneous polarization (P_s). Visualized simply, the pyroelectric coefficient defines the slope of P_s as a function of temperature, and can be fundamentally maximized at the ferroelectric transitions (Figure 2.1b) [3-5]. Due to crystal symmetry limitations, pyroelectricity does not exist (*i.e.*, at zero applied electric field) above critical phase transition temperatures such as the Curie transition temperature T_c, where high symmetry structures (*e.g.*, cubic paraelectric) are present. Within Chapters 5 and 6 of this Dissertation, I will expand the thermodynamic formalism of the pyroelectric coefficient tensor to elucidate the various subtle contributions present in thin-film, ferroelectric systems.

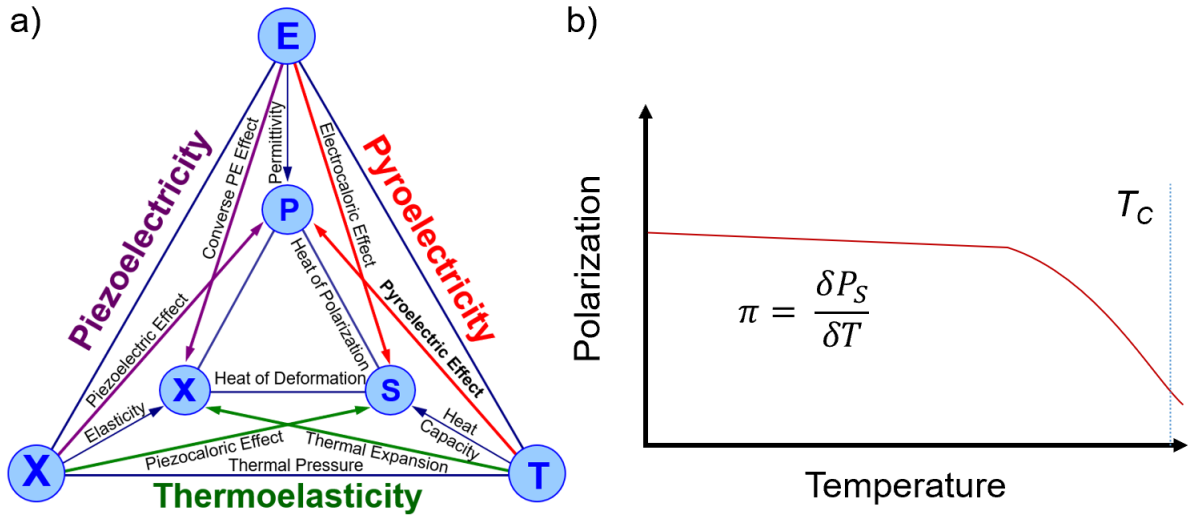

Figure 2.1: a) The Heckmann Diagram depicting the thermodynamic interrelations between stimuli and material response in crystals. b) Conventional polarization response of a second order ferroelectric phase transition with Curie temperature T_C.

2.2 Origins of Piezoelectricity, Pyroelectricity, and Ferroelectricity

Although pyroelectricity is found in a wide set of materials ranging from polymers to semiconductors to ceramics [6-10], crystallographic symmetries restrict the presence of pyroelectricity to a unique subset of materials. Starting from the total available (32) crystal classes, 20 are exhibit polarity when subjected to a stress and thus exhibit piezoelectricity [11,12]. The direct piezoelectric effect is defined by the third rank piezoelectric coefficient tensor (Eq. 2.2) which directly links mechanical stress (σ) and electrical displacement (D) [13].

$$d_{ij} = \frac{\delta D_i}{\delta \sigma_j} \qquad \text{(Eq. 2.2)}$$

Unlike other dielectrics that preserve inversion symmetry, piezoelectrics can maintain an electrical dipole moment under the presence of an applied mechanical stress. Of these (20) non-centrosymmetric, piezoelectric crystal classes, (10) classes maintain a unique polar axis (*i.e.* 1, 2, *m*, *mm*2, 4, 4*mm*, 3, 3*m*, 6, and 6*mm*) and thus define the subset of polar materials known as pyroelectrics [14,15]. Due to the crystal class subset, pyroelectrics can maintain a spontaneous polarization (P_s) without an applied mechanical stress. Moving further down crystal subclasses, if the coercive electric field of a polar/pyroelectric material does not exceed the breakdown field, the spontaneous polarization may be switched between two or more orientational states *via* an applied electric field, thus defining the class of ferroelectrics [16,17]. From the increased symmetry restrictions moving down subclasses, all ferroelectrics thus exhibit piezoelectric, pyroelectric, and dielectric response. Due to the comprehensive susceptibility of ferroelectrics to mechanical stress, temperature, and electric fields, high-performance ferroelectrics are typically chosen for pyroelectric systems [18-20] in which various stimuli, in addition to temperature, may be applied for P_s control.

For the presence of ferroelectricity, the aforementioned crystal symmetry limitations are further augmented by chemical and electronic considerations. Namely, the origin of ferroelectricity includes a complex interplay and balance between short-range repulsions favoring the cubic phase and long-range Coulomb forces favoring the ferroelectric phase [21,22]. Of high relevance to the oxides systems in my Dissertation, I will discuss the origins of ferroelectricity in the context of ABX_3 perovskite crystal structures, specifically, the canonical $PbTiO_3$ and $BaTiO_3$ systems (Figure 2.2) [23]. Although further discussed in the following section, for brevity, perovskites are defined by *B*-site cations residing within an octahedra of *X*-site anions (*i.e.*, oxygen octahedra in the case of oxides) and twelvefold-coordinated *A*-site cations [24,25]. In the case of $PbTiO_3$, studies of the electronic density of states have confirmed the strong overlap of the lead 6*s* and titanium 3*d* states with 2*p* oxygen valence bands, thus confirming the presence and importance of hybridization for ferroelectric stabilization. Similarly, $BaTiO_3$ also exhibits strong titanium and oxygen hybridization which is further supported by the ferroelectric distortion; however, interaction between the barium 5*p* and O 2*p* states is not necessary [26]. In all, ferroelectricity arises from the complex interaction of *B*-site cations and O anions to reduce the short-range repulsions. Primarily, complex oxides maintain *B*-site atoms such as Ti^{4+} and Nb^{5+} where the lowest unoccupied *d* states promote hybridization. In the case of *A*-site cations, modification of the ground state *via* induced ferroelastic strain and hybridization with valence states promotes indirect changes to the primary *B*-site and O interplay [26]. Alternatively, one can think of this from the point of view of phonons since, at

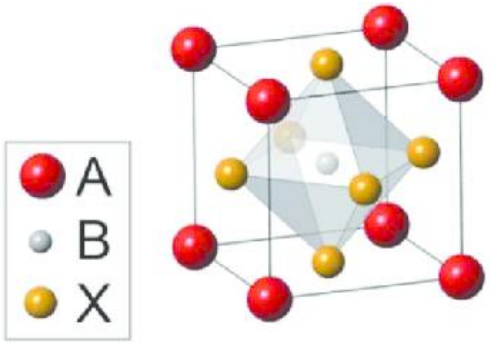

Figure 2.2: Perovskite crystal structure where *B*-site cation lies within an octahedra of *X*-site anions. *A*-site cations maintain corner sharing positions [23].

the foundation of ferroelectricity lies a special class of structural phase transitions in which the condensation of a soft mode (*i.e.*, low frequency) phonon at the Brillouin-zone center occurs. Specifically, the transverse optical phonon mode condenses and "freezes" at $k = 0$, marking the transition across T_C in which a phonon of infinite wavelength and the onset of finite polarization develops [27-29].

2.3 Properties of Ferroelectric and Pyroelectric Materials

Pyroelectrics that exhibit ferroelectric function display electric-field dependence in which polarization orientation may be readily switched. Within Figure 2.3 [30], a classic ferroelectric polarization vs. electric field (PE) hysteresis loop response is displayed, indicating two oppositely poled states at positive and negative electric fields. Through charge integration, the evolution of the polarization can be measured and analyzed as the result of the nucleation and growth of domains which reorient one polarization state over the other. Lastly, the temperature dependence of P_s is depicted as T_C is approached, confirming the negative slope of P_S previously described in Figure 2.1b. Similarly, due to the reorientation of polarization states, pyroelectrics also produce a traditional "butterfly" curve as π is plotted against applied voltage (Figure 2.4) [31]. Here, the two minima of pyroelectric response correspond to the coercive voltage in which oppositely poled orientations become equal in magnitude, thus minimizing P_S dependence on temperature. Contrary to PE loops, the sign of π does not invert sign upon application of voltage since P_S intrinsically decreases with temperature, irrespective of the current polarization state. It is also worth noting that although standard PE measurements provide a first approximation to the quantification of π, more sophisticated protocols are needed as described in Chapter 3 of this Dissertation. Furthermore, pyroelectrics with ferroelectric order maintain a unique anomaly in the temperature dependence of dielectric permittivity as the centrosymmetric, paraelectric phase is approached.

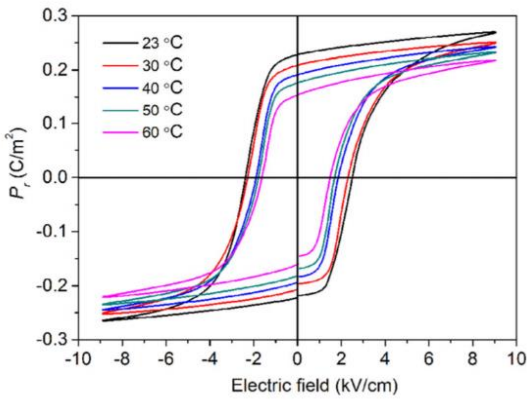

Figure 2.3: Temperature dependence of the polarization hysteresis curve for single crystal relaxor-ferroelectric $PbMnO_3$-$PbTiO_3$ measured at 2 Hz frequency [30].

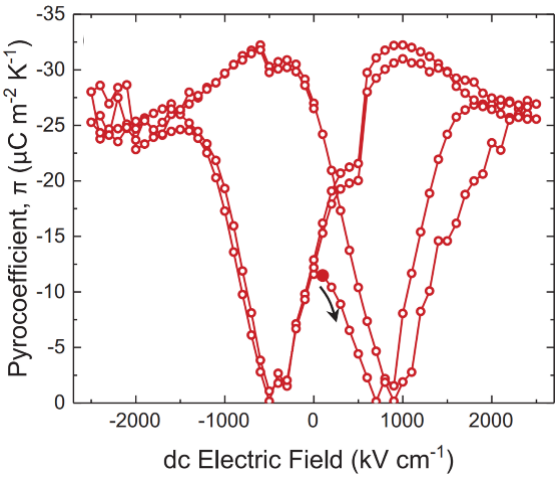

Figure 2.4: Standard "butterfly" curve depicting the evolution of π under applied DC field for 10-nm-thick silicon-doped HfO_2 [31].

$$\chi = \frac{A}{T - T_C} \qquad \text{(Eq. 2.3)}$$

As described *via* the Curie-Weiss Law in Eq. 2.3, the electrical susceptibility χ can be fit linearly to extract the structural phase transition T_c in addition to the phase transition order (*i.e.*, first or second) [32,33]. A prototypical response is provided in Figure 2.5 which depicts the T_c anomaly of $PbZr_xTi_{1-x}O_3$ at various compositions [34]. Since ferroelectrics also maintain mechanical stress and electric field dependencies, both the magnitude and location of the Curie transition may be tuned accordingly.

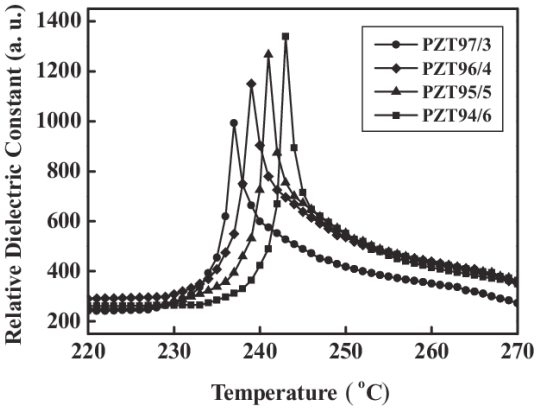

Figure 2.5: Temperature dependence of the dielectric constant of $PbZr_xTi_{1-x}O_3$ at various compositions [34].

2.4 Complex-Oxide Ferroelectric Materials

As previously discussed, robust ferroelectrics are ideal candidates for pyroelectric systems due to highly deterministic control of P_s . As such, I have chosen to focus this Dissertation on two robustly established ferroelectric systems that are accompanied by decades of dielectric, piezoelectric, and ferroelectric property physics.

2.4.1 $PbZr_xTi_{1-x}O_3$

One of the most widely used commercial ferroelectrics is found in the $PbZr_xTi_{1-x}O_3$ system which has experienced over 60 years of study as a candidate material for electromechanical sensors, actuators, ferroelectric-based random access memory (FeRAM), and transducers [35-38]. Consisting of a perovskite crystal structure, relatively displaced *B*-site cations (zirconium and titanium) produce dipole moments under applied electric fields responsible for bulk P_s. The success of $PbZr_xTi_{1-x}O_3$ in commercial applications stems mainly from the wide range of properties and performance at various zirconium/titanium concentrations (Figure 2.6) [39]. Near the vicinity of the morphotropic phase boundary (*i.e.*, intermediate compositional phase separating tetragonal and rhombohedral structures), for example, the degenerate energy landscape of the monoclinic structure promotes robustly enhanced dielectric and electromechanical susceptibilities [40-43]. Additionally, both anti-ferroelectric and ferroelectric phases allow for a rich environment of susceptibilities, transition temperatures (250-450°C), crystal structures (*e.g.*, *P*4*mm*, *R*3*c*, etc.), and ferroelectric-ferroelastic domain architectures [44-47].

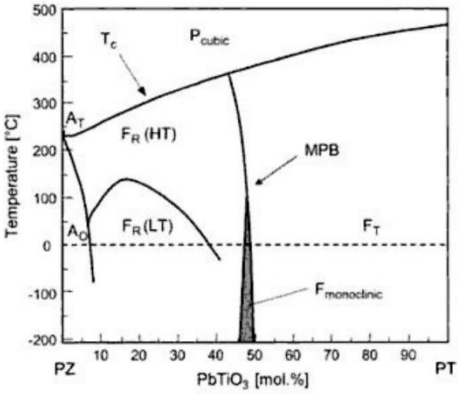

Figure 2.6: Phase diagram of PZT displaying the various structural phases and transition temperatures [39].

2.4.2 $BaTiO_3$

Another ferroelectric workhorse developed in the early 1950s is the perovskite $BaTiO_3$. Generally implemented as a lead-free ceramic in piezoelectric sensor, actuator, transducer, and thermistors applications [48-50], $BaTiO_3$ exhibits robust dielectric constants (>5000) and a relatively low cubic-to-tetragonal T_C (120°C) allowing for enhanced performance near room temperature [51-53]. In contrast to $PbZr_xTi_{1-x}O_3$, $BaTiO_3$ exhibits additional phase transitions (Figure 2.6) at 5°C (tetragonal to orthorhombic) and -90°C (orthorhombic to tetragonal) [54]. Key to the wide-spread use of $BaTiO_3$ is the ability to systematically substitute barium and titanium with a wide array of aliovalent and isovalent dopants, thus allowing for the systematic tuning and enhancement of numerous properties. Specifically, $Ba_xSr_{1-x}TiO_3$ and $BaZr_xTi_{1-x}O_3$ can be used to precisely tune T_C by 3.3 K per at.% and 8 at.%, respectively, in addition to controlling not only the phase transition order, but also the propensity for ferroelectric-relaxor behavior [55]. Although the dielectric, piezoelectric, and ferroelectric properties are well established for the canonical PZT and BTO systems, pyroelectric response has remained relatively understudied.

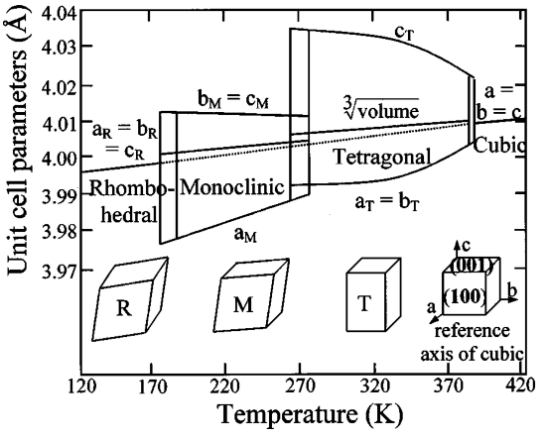

Figure 2.5: Unit cell parameters of $BaTiO_3$ depicting the various transition temperatures and crystal structures [54].

2.5 Epitaxial Ferroelectric Thin-Films

With advances in synthesis capabilities over the past two decades, thin-film ferroelectric performance has increasingly improved toward single-crystal limits. With immense dielectric constants, robust ferroelectric hysteresis, and enhanced fatigue cycling resistance, thin-films allow for new levels of performance and unique properties not present in bulk form [56-58]. At the forefront of thin-film property enhancement lies the introduction of boundary conditions imparted by underlying substrates. Unlike the case for bulk ferroelectrics, epitaxial thin films can sustain substantially greater magnitudes of mechanical strains (>3%), allowing for the accessibility of a relatively untouched realm of property physics. Here, novel domain architectures and phases can be engineered via the systematic consideration of strain states, substrate orientations, compositional gradients and more [59-62]. Additionally, thin films allow for order of magnitude smaller coercive voltages, power consumption, and switching speeds, allowing for the integration into CMOS technology as FeRAM and NVRAM components [63,64]. Despite the renowned achievements and understanding in thin-film control of dielectric, piezoelectric, and ferroelectric properties, pyroelectrics have remained relatively understudied.

As a result, the introduction of pyroelectrics in thin film form remains extremely appealing due to the numerous unexplored competing mechanical, thermal, and electrical boundary conditions. With the simplification of heat transport models and reduced thermal masses in thin films, pyroelectrics are suitable for high frequency, high electric field heating cycles,

allowing for the exploration of new performance regimes, and on-chip integration not possible in bulk. Despite these advantages, thin-film pyroelectrics introduce a new set of challenges to researchers. First, unlike bulk pyroelectrics that are relatively decoupled from underlying substrates, pyroelectric response can be heavily dominated by the mechanical boundary and thermal boundary conditions of underlying substrates. In this sense, accurate characterization of pure pyroelectricity is often convoluted and diminished by large substrate effects. Additionally, relatively trivial indirect characterization methods utilized in bulk pyroelectrics now require direct methods where thermodynamic Maxwell relations no longer hold. Furthermore, due to the complex interplay of piezoelectric and ferroelectric susceptibilities, measuring the true intrinsic thin-film pyroelectric response becomes excessively challenging while combating opposing, and often larger additional contributions to pyroelectricity.

2.6 Pyroelectric Applications

With the ability to generate voltages under applied temperature changes from absorbed radiation, pyroelectrics have gained popularity with IR sensors since the early 1970s. Unlike quantum detectors that operate *via* the photoelectric effect and require high quality semiconductors, precise bandgap control, and low operating temperatures (77 K); pyroelectric thermal detectors provide a low-cost alternative with fast response (picosecond), low power, and wide temperature/sensitivity ranges [65-68]. Due to the frequency dependence of the pyroelectric effect (Eq. 2.4) [2],

$$i_p = \pi A \frac{\partial T}{\partial t} \qquad \text{(Eq. 2.4)}$$

where i_p, π, A, T, and t denote the pyroelectric current, pyroelectric coefficient, area, temperature, and time, respectively, pyroelectric detectors often require light choppers to produce the temperature variation needed to detect immobile objects. As such, with the integration of pyroelectric detectors into 2D arrays, applications such as thermal imaging, burglar alarms, IR spectrometers, flame/fire detectors, laser detectors and pollution monitors are possible [65,68].

As we approach new achievements in thin-film pyroelectrics, novel applications within the field of waste-heat energy conversion have recently evolved. Through the incorporation of waste-heat energy cycles (Ericsson cycles), isoelectric and isothermal steps allow for the generation of pyroelectric current from ambient temperature changes (Figure 2.6) [69,70]. Due to the development of enhanced pyroelectric coefficients, thermal frequency cycling, and applied electric field

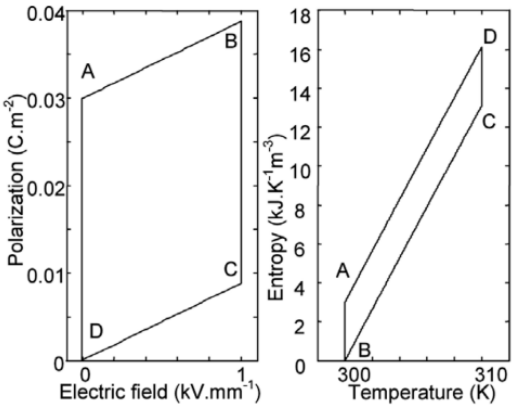

Figure 2.6: Depiction of isoelectric and isothermal steps of the Ericsson cycle on polarization vs field (left) and entropy vs temperature axes (right) [69].

limits, thin-film pyroelectrics have shown robust energy/power densities and scaled Carnot efficiencies [71,72], comparable to state-of-the-art thermoelectric performance. In all, pyroelectrics stand poised to deliver next-generation energy conversion performance as I investigate the rich and untouched landscape of property physics and thin-film synthesis capabilities.

Chapter 3

Synthesis, Processing, and Characterization of Electrothermal Test Platforms

In this Chapter, I describe the processes related to the synthesis, electrothermal device processing/integration, and wide range of applied thin-film metrologies to elucidate the material physics of such complex ferroelectric oxides. With control of each processing step, from raw material powders to final test platforms, I demonstrate the stringent considerations needed in achieving sub-nanoampere measurement capabilities on electrically insulating, high crystallinity, and chemically homogenous ferroelectric thin-film systems.

3.1 Synthesis of Ferroelectric Thin-Film Heterostructures

The synthesis of complex oxide pyroelectric and ferroelectric thin films requires sufficient control and understanding of thermodynamic deposition conditions, especially with growth rates on the order of fractions of angstrom per second. Here, I discuss the fundamental physics, various strengths and weaknesses, and the numerous growth parameters of pulsed laser deposition needed to obtain the desired epitaxial thin-films.

3.1.1. Pulsed-Laser Deposition

Throughout this work, I utilized pulsed-laser deposition (PLD) to systematically synthesize complex thin-film oxides with various associated material properties and responses. As compared to other physical vapor deposition methods (*e.g.*, molecular beam epitaxy and magnetron sputtering), PLD also allows for the stochiometric transfer of excited oxidizing species when utilized correctly all while maintaining relatively simpler initial setup, extensive success in complex oxide compound deposition, and compatibility from UHV up to 1 Torr gas environments [1]. The PLD deposition process for oxides, metals, and semiconductors primarily consists of three steps. Namely, a laser is first incident upon a deposition target of desired chemistry, followed by the excitation of a plasma plume directed at a heated substrate, and concludes with the deposition and annealing of the respective species upon the substrate surface (Figure 3.1) [2]. With an impinging ultraviolet laser, a target of the desired stoichiometry is ablated, thus allowing for the expulsion of a multi-cation flux. The production and chemistry of the resulting plume is determined by both the laser fluence (*i.e.*, time integral of the laser intensity over pulse duration in units of J/m^2) and the optical absorption coefficient of the target. Without careful consideration of laser wavelength and the required ablation threshold of the target (0.1-1 J cm^{-2}), only thermal evaporation occurs, typically with a chemistry limited by the vapor pressures of the target constituents [3]. Through the incorporation of gases during the deposition process, a reactive species is provided to the multi-cation flux in addition to the attenuation of kinetic energies of the ablated species (*i.e.*,1 eV to >100 eV). By controlling the target to substrate separation, background gas pressure, and laser fluence, deposition rates may be controlled down to the sub-monolayer level [4]. Furthermore, with use of reflection high-energy electron diffraction (RHEED), these sub-monolayer film thickness can be accurately quantified, *in situ*, in real time. With collected low-angle electron diffraction signals and associated oscillation intensities, crystallinity, smoothness, and growth rate can be extracted [5-7]. As a result, RHEED-assisted PLD depositions have been increasingly used in the synthesis and investigation of thin-film interfaces and superlattice

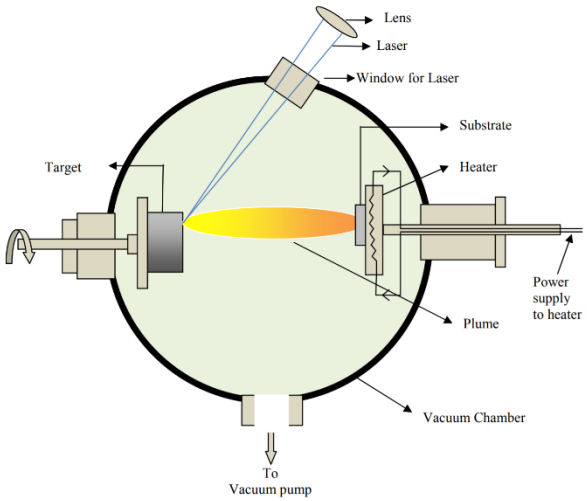

Figure 3.1: Schematic of pulsed laser deposition chamber and process depicting incident laser, plume, and substrate deposition [2].

heterostructures [8-10]. Although primarily advantageous for academic research, PLD is inevitably limited by its fundamental simplicity. Namely, with incident laser spot areas on the order of <3 cm^{-2}, only relatively small plume volumes are possible, often limiting the size of substrates to small sub-inch coupons rather than standard silicon wafer sizes used in semiconductor fabrication [11]. Additionally, PLD is often hindered by knock-off damage from high-energy adatoms in the plume, "splashing" of micron sized particles due to increased laser penetration depth, and nanoparticle deposition unless all deposition parameters are carefully tuned [12].

In this work, I utilized a KrF excimer laser (Compex, Coherent) operating at 248 nm wavelength with deposition frequencies of 5-15 Hz and laser fluences between 0.8-1.5 J cm^{-2}. During growth, the substrate temperature (for the materials in my studies) ranged between 550-750°C with oxygen partial pressures on the order of 100-150 mTorr, symmetric parallel plate geometry heterostructures were deposited in series. Successful synthesis via PLD requires reliable operating procedures and accurate thermodynamic process control. To begin, all single-crystalline substrates (Cyrstec, GmbH; rare-earth scandates) were pre-screened via atomic force microscopy to confirm both smooth initial surface morphology (RMS roughness <500 pm) and low defect particle densities (<10^{-2} particles per μm^2). After an acetone and isopropanol alcohol ultrasonication bath (10 min.), substrates were mounted and cured (80°C for 5 min.) to a sanded metallic PLD heater with use of silver paint (Leitsilber 200, Ted Pella, Inc.) to ensure sufficient thermal contact at low pressures and high temperatures. After the ceramic targets of required stoichiometry were sanded and mounted into the PLD chamber, the system was pumped down to a base pressure of (at least) $5x10^{-6}$ Torr. At this point, a variable leak valve is used to introduce an dynamic oxygen environment of the required pressure. Once the growth temperature is reached with a 30°C min^{-1} ramp rate, each target is pre-ablated (i.e., shutter closed) at the given growth laser frequency and energy to ensure the target surface area and microstructure has reached the desired equilibrium. To achieve a more homogenous deposition, targets are rastered and rotated to maximize ablated surface area, while minimizing variations during growth such as deposition rates and or laser fluence. With control over oxygen pressure, laser energy, laser frequency, and substrate temperature, each layer of any given tri-layer heterostructure was independently optimized for the correct crystal structure, phase, surface morphology, and electrical properties. Lastly, the epitaxial thin-films were cooled in a static oxygen pressure (700 Torr) back to room temperature at a reduced rate (5°C min^{-1}) to minimize adverse thermal stress effects to the resultant domain structure and crystal structure.

3.1.2 Ceramic Oxide Pellet Processing

In my work, I synthesized various complex oxide materials, including the $PbZr_xTi_{1-x}O_3$ and $BaTiO_3$ systems. For brevity, I will discuss the synthesis of the prototypical $PbZr_xTi_{1-x}O_3$ system. As mentioned previously, PLD relies on the stoichiometric transfer of a multi-cation flux from a (typically) ceramic target. To obtain the desired chemistry, I synthesized numerous 1 inch diameter ceramic targets of their respective chemistry for use in PLD. To begin, carefully measured ceramic oxide powders of Pb(II)O, ZrO_2, Ti(IV)O_2 (99.99% purity) were first weighed and homogenously mixed to the desired composition based off the respective molar mass. For the case of lead-based oxides, an additional 10 mol% lead was

incorporated to offset any lead-loss during processing or growth due to high volatility and vapor pressure (>10^2 mm Hg) [13]. After the as-received powder particle size was reduced via traditional mortar and pestle grinding (1 hr.), the final powder mixture was loaded into an Al_2O_3 crucible and reactively calcined below the melting temperature (800°C) in a tube furnace for 2 hours in air. The calcination process is critical in obtaining both the crystallite size and promotion of the solid-state reaction needed to obtain the correct compositional phase from the constituent powders [14]. Following the first heat treatment, the calcined powder was further grinded to further reduce the crystallite size (1 hr.). Next, the powders were transferred into a stainless-steel die and uniaxially mechanically pressed (1 MPa) into 1 in. diameter, 0.25 in.-thick ceramic pellets. With this preliminary preparation, the ceramic targets were then cold isostatically pressed (CIP) at 150 MPa to obtain >90% of the theoretical density of $PbZr_xTi_{1-x}O_3$ (8 g/cm^3) [15]. To minimize lead loss during the sintering step, excess powder from the calcination process was used to cover the exposed surfaces of the target pellet before being placed at 1200°C for 3 hours under an oxygen environment. Finally, the ceramic targets were cooled (10°C min^{-1}) and sanded to remove surface morphology inhomogeneities before being mounted for use. To ensure the stoichiometry of the final target, all processed ceramic pellets were used to deposit room temperature films via PLD and subsequently characterized via Rutherford backscattering spectrometry. With ceramic targets of the required chemistry in hand, stoichiometric thin-film ferroelectric oxides can be successfully synthesized.

3.2 Processing of Electrothermal Test Platforms

Extracting meaningful scientific insights from the complex and convoluted realm of thin-film pyroelectrics requires exceptional temperature control, temperature characterization, and ability to separate out non-pyroelectric signals. Key to the accurate investigation and extraction of both the pyroelectric/ferroelectric response and energy-conversion capability of thin-film ferroelectrics is the use of microfabricated electrothermal test vehicles.

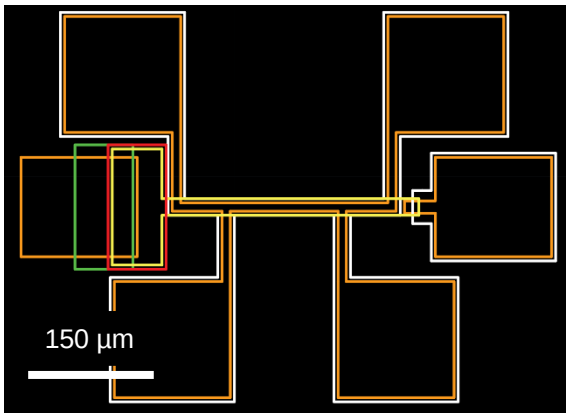

Figure 3.2: The 5-mask patterns used in the fabrication of the electrothermal test platform of this Dissertation. P1(yellow), P2 (Red),P3 (Green), P4 (white), and P5 (Orange) depict the tri-layer pyroelectric heterostructure stack, top electrode etch, bottom electrode Pt sidewall contact, SiN_x electrical insulator, and Pt heater line patterns, respectively.

In this work, I utilized nanofabrication processes to synthesize pyroelectric heterostructure devices with both isolated thermal and electrical circuits that can simultaneously provide temperature and AC/DC electric fields; all the while maintaining the capability of collecting the highly convoluted resultant pyroelectric current. Specifically, I utilized a 6-terminal electrothermal test platform that uses thin-film resistive heating to deliver AC temperature oscillations to an

underlying parallel plate capacitor pyroelectric heterostructure. This device platform requires a complex, 5 mask photolithography process with alignment features down to <2.5 µm. Beginning with an as-grown PLD blanket tri-layer of a conducting bottom and top oxide electrode which symmetrically sandwiches the pyroelectric thin-film layer, the first photolithography step is undertaken (P1; yellow within Figure 3.2). Standard g-line photoresist (OCG 825 35CS) of 1 µm thickness (6000 RPM spin coater speed) is used to ensure that the subsequent process etching does not interact with the active device layers. From this point, the blanket tri-layer is defined into a "lollipop" geometry via ion milling into the underling substrate. With previously characterized milling rates of ~7 nm min^{-1}, the oxide stack is typically milled to a depth of 225 nm while under 10^{-4} Torr argon pressure, 45° incidence angle, 15 RPM stage spin speed, and 300 V/150 mA beam voltage and current, respectively. To minimize possible sidewall redeposition which often plagues the ion-milling processes [16], a high angle 70° side-wall clean is used. Following P1, the second photolithography step (red, Figure 3.2) is used to isolate the active layer of the "lollipop" geometry to only within the stem region. Additionally, adjacent circular capacitors are included to act as an intermediate process check to confirm working ferroelectric devices. Using a 0.1 M $NaIO_4$ solution in DI H_2O, a wet etch of the top $SrRuO_3$ electrode can be completed with high selectivity in the lollipop head region, thus minimizing gouging effects to the underlying pyroelectric. At this point, the electrothermal test platform has a defined, active tri-layer region only within the device stem (310 x 20 µm). Furthermore, with a top $SrRuO_3$ layer already exposed on the stem, contact to the bottom electrode is made through a platinum pad that drapes over the sidewall of the device head (green, Figure 3.2). Due to the wet etch removal of the top electrode at the device head, an open circuit configuration can be ensured, while allowing for ample contact area. With the electrical circuit complete, an isolated thermal circuit must be incorporated to provide the pyroelectric with the necessary AC temperature excitations. To accomplish this, a blanket layer of SiN_x is deposited via plasma enhanced chemical vapor deposition (PE-CVD). This silane (SiH_4) and ammonia (NH_3) -based process is carried out at 950 mTorr and 350°C with use of both low- and high-frequency power, ensuring a high-density nitride film. Although H-based processes have shown to be detrimental to ferroelectric performance during forming gas anneals of commercial transistors, no subsequent affects have been reported to date [17-18]. Due to low dielectric constant (7), low electrical conductivity, and thermal conductivity of ~2 W/m-K of SiN_x [19-20], this SiN_x intermediate layer acts as not only an electrical insulator, but also a

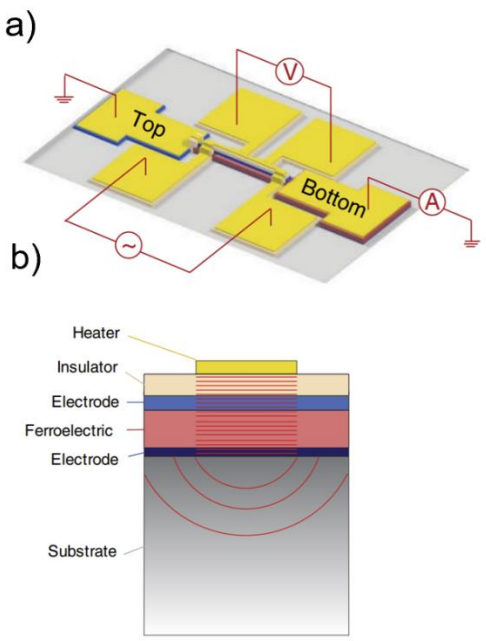

Figure 3.3: a) 3-Dimensional schematic of the fully-processed electrothermal test platform where $\sim$, V, and A refer to connections where applied heating current, measured voltage, and measured pyroelectric current are contacted, respectively. b) Associated cross sectional view depicting the various layers of the heterostructure [60].

thermal conductor between the top electrode and resistive thin-film heater. After the blanket deposition of the insulating nitride, a reactive-ion etch (RIE) based on reactive CH_4 and O_2 gas is used to define the nitride layer into 5 pads (white, Figure 3.2). The defining RIE step is crucial in minimizing lateral heat dissipation and maintaining the necessary thermal boundary conditions needed to accurately quantify the heat transport through the pyroelectric thin-film stack. Lastly, a platinum resistive heater (orange, Figure 3.2) is deposited via a lift off process, allowing four contact pads to the center resistive heating line, in addition to two contact pads for the bottom and top electrodes of the ferroelectric circuit. Through a multi-mask, multi-tool nanofabrication process, thin film electrothermal test platforms can be generated to provide both highly accurate and highly-sensitive pyroelectric response measurements (Figure 3.3).

3.3 Characterization of Pyroelectric Thin-Film Heterostructures

In this section, I review the underlying physics and importance of the various metrologies required in investigating the pyroelectric properties of thin-films. Using X-Ray diffraction studies, scanning-probe techniques, electrical-transport methods, and numerous other material property characterization protocols, I am able to accurately bridge the various resultant material properties and susceptibilities.

3.3.1 Structural and Chemical Analysis

The resultant pyroelectric and ferroelectric properties of thin films are unequivocally coupled to the underlying crystal structure and material chemistry. These material properties provide crucial insights into helping address and explain the various findings of the electrothermal community. Following the PLD synthesis of a given tri-layer pyroelectric stack, X-ray diffraction (XRD) is utilized to quantify the crystal lattice symmetries and provide insights not obtainable from surface sensitive metrologies. For the case of perovskite oxides, features such as material phase, orientation, thickness, crystallinity, mechanical strain, lattice parameter, ferroelectric domain structure, and even composition can be extracted [21-25]. At the foundation of XRD analysis lies the interaction of incident X-Ray photons of a given wavelength with the electrons of a periodic crystal lattice. In this work, I utilized Cu (K_α) radiation with a wavelength of 1.54 Å from a Panalytical Xpert^3 MRD 4-circle diffractometer. To achieve the diffraction condition in which constructive interference is met, Bragg's law must be fulfilled (Equation 3.1) [26]: Å

$$n\lambda = 2d_z sin\theta \qquad \text{(Eq. 3.1)}$$

Here, λ, n, θ , and d refer to the X-Ray wavelength, order of reflection, incidence angle, and out of plane lattice spacing, respectively. Thus, with a standard scan defined as a $\omega - 2\theta$, the incidence angle is coupled to the detector angle to provide a spectrum of diffraction intensities at various ω angles where Bragg's law is satisfied (Figure 3.4). Through the use of powder diffraction files, atomic form factors, and Xpert^3 Data Viewer Software, diffraction

peaks in thin films can be attributed to various crystal orientations. In the case of my work in thin-film oxides, often only a single peak is identified, confirming the single orientation, unlike polycrystalline materials. Attention is also brought to the diffraction peak width, often quantified as a full width at half maximum (FWHM) value. Through use of the Scherrer equation, a degree of mosaicity and grain structure can be extracted from the peak breadth, indicating the slight tilting of various adjacent lattice volumes [27]. An additional standard metrology tool for XRD used in this work is that of reciprocal space mapping (RSM). This technique utilizes the reciprocal space of a crystal lattice to provide a greater degree of in-plane orientation information. As an extension of standard line scans found in $\omega - 2\theta$, RSM introduces a systematic ω-offset for a given 2θ sweep [28].

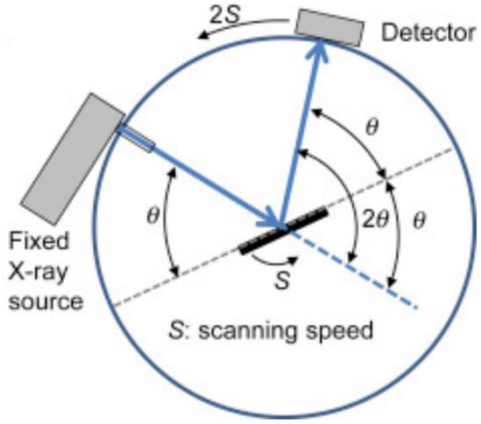

Figure 3.4: XRD geometry used within this Dissertation. X-Ray source remains fixed while the sample stage and detector are coupled to perform the standard $\omega - 2\theta$ scan [20].

Following the confirmation of the required crystal structure, a chemical analysis is needed to ensure materials of the proper chemistry have been synthesized. To accomplish this task, I relied on Rutherford backscattering spectrometry (RBS). This direct metrology (*i.e.*, no dependence on reference standards) is based on the elastic collisions of incident He^{2+} ions and atoms of the material under study (Figure 3.5) [29]. With a quantity of high-energy ions `penetrating the material, an additional fraction is backscattered and collected to provide not only depth profiling information, but insight to the specific elemental collisions present. By accurately quantifying the energy of the secondary ions at a fixed incident angle, the kinematic factor (K) can be used to index elements and their composition within a given material (Eq. 3.2) [30].

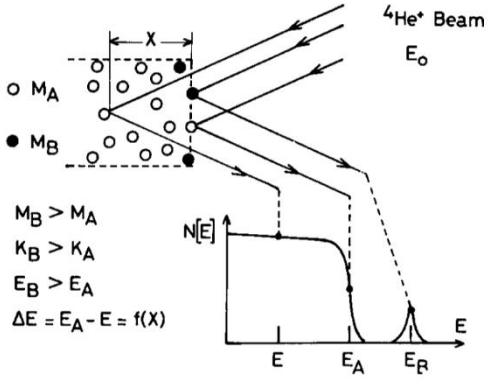

Figure 3.5: Depiction of incident ion interaction with a given atomic lattice of masses (M), kinetic energy (k), penetration depth (X), and total energy (E). The bottom figure displays an associated RBS spectrum with the respective backscattered ion energies [29].

$$K = \frac{M_1^2}{(M_1+M_2)}\left(cos\,\theta \pm \left[\left(\frac{M_2}{M_1}\right)^2 - (sin\,\theta)^2\right]^{1/2}\right)^2 \qquad \text{(Eq. 3. 2)}$$

Here, θ (scattering angle), M_1(mass of backscattered ion), and M_2 (mass of target nucleus) can be equated with incident energy. To accomplish this metrology in my work, I used a pelletron tandem accelerator (National Electrostatics Corp. Model 5SDH) with He^{2+} ions of 3.04 MeV energy. Through use of a Cornell geometry, an incident, exit, and scattering angle of 22.5°, 25.35°, and 168° were used, respectively. All spectra analysis was completed with SIMNRA RBS software (https://home.mpcdr.mpg.de), providing spatial composition insights,

thickness, and density with least-squares method values of >0.99. To maximize the accuracy of RBS to only 1-2% error, careful attention and choice of the underlying substrate and layers is needed to ensure that no critical elemental peaks are overlapped or convoluted with others. In all, both crystal structure and chemistry analysis lie at the foundation of robust PLD synthesis and ferroelectric/pyroelectric material performance. Without control of the underlying lattice, material susceptibility tuning cannot be achieved.

3.3.2 Surface Topography and Domain-Structure Analysis

Through scanning probe methods, specifically atomic force microscopy (AFM) and piezoresponse force microscopy (PFM), deep insights into the underlying material property physics can be obtained. In this work, I utilized both tapping-mode AFM and dual-frequency resonance PFM methods to investigate the surface morphology and domain structures of PLD synthesized thin-film ferroelectrics. Specifically, an MFP-3D (Asylum-Oxford Instruments) system was used in conjunction with platinum/iridium-coated PFM tips (Nanosensor, PPP-EFM) and silicon AFM tips (BudgetSensors, Tap300AL-G). To preface the AFM and PFM results/findings of this Dissertation, I will first briefly discuss the fundamental mechanics and resultant insights gained from such probing methods. Atomic force microscopy was first developed in the mid-1980s, thrusted from the prior developments of scanning tunneling microscopy (STM). Binnig *et al.* utilized the concept of force to image atomic surfaces, dropping the previous limitations of conducting surfaces required by STM [31]. Briefly, all AFM systems maintain 5 basic components. First, a sharp tip of a given radius (<μm) extends from a soft cantilever of a fixed spring constant. Secondly, a system for monitoring the deflection of a cantilever (e.g. photodiode detector) allows an adjacent feedback system to adjust the deflection, thus maintaining a constant interaction force. Lastly, a mechanical translation stage, most commonly piezoelectric-based, allows for areal scanning of a given sample while a display system converts the measured raw data into a resultant scan image. Crucial to the interpretation of AFM results is the understanding that the final obtained image is a convolution of both tip and surface response, and often prone to experimental artifacts if not properly addressed (e.g. electronic noise, surface contamination, scan hysteresis/creep etc.) [32]. Of the various AFM modes (i.e. static and dynamic) I primarily utilized tapping-mode AFM in this Dissertation. Tapping mode is defined as a high amplitude, dynamic mode which closely tracks not only the deflection (i.e. static contact mode), but also the oscillation frequency, phase, and amplitude shift of the cantilever, providing a plethora of new capabilities and accuracy in quantifying tip-surface interactions [33,34]. Unlike static contact modes which promote increased tip and sample surface wear/damage, tapping mode operates on the principle of driving cantilever oscillations via a fixed frequency/amplitude external function generator at a set distance from the sample, incorporating both short-range repulsive and long-range attractive forces [35]. As described by the following function (Eq. 3.3):

$$\varphi = tan^{-1}\left(\frac{m\omega\omega_0}{Q(k-m\omega^2)}\right) \quad \text{(Eq. 3.3)}$$

the phase angle φ can be related to the vibrational frequency of the cantilever (ω), mass (m), spring constant (k), quality factor (Q), and cantilever resonance frequency (ω_0) [36]. As

such, by reducing the tip-sample interaction time, and measuring the resultant sample interaction change of the cantilever oscillation dynamics via lock-in amplifier, reduced lateral tip-sample forces of this mode provide higher resolution capabilities over standard contact methods. AFM plays a pivotal role in investigating PLD growth dynamics (Volmer-Weber island growth to Frank van der Merwe layer-by-layer growth)[37], epitaxial strain relaxation [38], second phase segregation and much more [39]. Although widely applicable to various thin-film oxides, polymers, and even biological materials [40], AFM is intrinsically limited in its ability in elucidating ferroelectric and piezoelectric susceptibilities. To address this, PFM was developed as an adaptation of AFM in which an AC voltage can be applied to a conducting tip, thus allowing for the detection of voltage-induced surface displacement. Namely, the first harmonic component ($A_{1\omega}$) is extracted from the total tip displacement (A) (Eq. 3.4)

$$A = A_0 + A_{1\omega}(\omega t + \varphi) \quad \text{(Eq. 3.4)}$$

where ω, t, and φ refer to the angular frequency, time, and phase, respectively. Thus, under an applied periodic voltage ($V_{tip} = V_{DC} + V_{AC}\cos(\omega t)$), the tip phase values provides key information in regards to the orientation of the underlying excited polarization and domain states [41]. For example, classically down-poled *c*-domains would induce an expansion of the sample surface and thus an associated φ=0 response. On the contrary, an upward oriented *c*-domain would be accompanied by a φ=180 response. Although highly qualitative, PFM response can provide nontrivial quantitative insights. The primary difficulty arises in the convoluted contributions of electrostatic and nonlocal (capacitive cantilever-sample) effects. Despite these subtleties, PFM has long remained a staple in local electromechanical metrology from the early 1990s [41] where the increased electric field susceptibilities of ferroelectrics, pyroelectrics, and piezoelectrics can be probed. In addition to the local nanometer surface morphology capabilities of AFM, PFM allows the ferroelectric community to directly probe not only out-of-plane ferroelectric/ferroelastic domain architectures, but also the in-plane structures. These unique capabilities have allowed for a wide range of material advancements in the past two decades such as the discovery of novel polar-vortex structures [42] and relaxor-ferroelectric nanoscale polar structures [43]. Furthermore, adaptations of PFM have also allowed the investigation of local polarization-hysteresis loop measurements (Piezoresponse Force Spectroscopy), domain patterning/writing in ferroelectrics, and local domain switching kinetics [44]. Without the pivotal physical understandings gained from AFM and PFM studies within the past two decades, the field of thin-film ferroelectrics would have remained at indeterminant stand still.

3.3.3 Electrical Characterization

To accompany the local probe methods of AFM and PFM of this Dissertation, numerous macro-scaled electrical metrologies were utilized to shed light upon the inner dynamics and material physics of ferroelectric materials. Through standard polarization hysteresis, small-signal dielectric, and current-leakage measurements, a self-consistent structure-property relationship can be established.

3.3.3.1 Polarization-Voltage Hysteresis Measurements

One of the most well-known and utilized characterization methods of ferroelectrics is the prototypical polarization-voltage (P-V) hysteresis measurement. In this metrology, an applied triangular voltage waveform of a given frequency (1-10 kHz for this Dissertation) is applied across a ferroelectric capacitor structure. Since polarization can be quantified as the total surface charge density, a P-V measurement integrates the total current density (j) with respect to time as

$$P = \int j dt \quad \text{(Eq. 3.5)}$$

As such, P-V measurements quantify various parameters such as the saturation polarization (high field) and remanent polarization (zero field) to elucidate features such as switching and relaxation polarization. Additionally, the coercive voltage (V_c) and slope of the P-V response at the V_c can be extracted to indicate the ease of switching and ferroelectric-domain dynamics (Figure 3.6). Like all electrical measurements, P-V loops are prone to artifacts that may be convoluted with the true ferroelectricity [45]. In this work, I used a Precision Multiferroic Tester (Radiant Technologies Inc.) with a virtual ground-based transimpedance amplifier to accurately characterize the various ferroelectric materials. It should also be noted that P-V hysteresis measurements have been utilized previously for pyroelectric characterization but suffer from spurious electrical leakage currents that cannot be separated out [46].

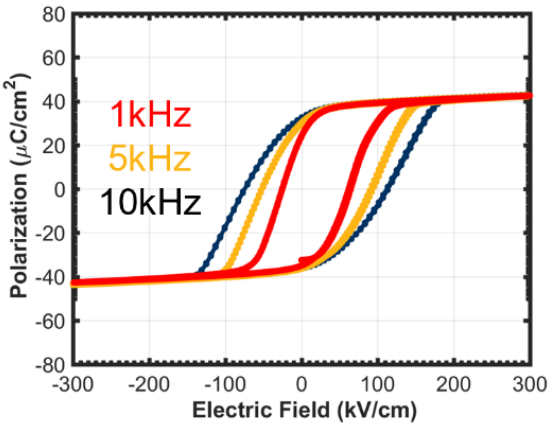

Figure 3.6: PE hysteresis loop frequency dependence of V_c for 100-nm-thick $PbZr_{.52}Ti_{0.48}O_3$ pyroelectric.

3.3.3.2 Dielectric Measurements

In order to investigate the complex dielectric susceptibility of the various material systems, I turned to the use of impedance spectroscopy. Impedance spectroscopy is generally used to quantify capacitance, dielectric loss, and impedance of given dielectric device structures. As a small-signal measurement, an AC excitation (5-20 mV) is applied over various frequencies and background DC biases. Capacitance (C) can then be extracted from the resultant in-phase and out-of-phase current as:

$$C = \frac{I}{dV/dt} \quad \text{(Eq. 3.6)}$$

Due to the highly coupled dielectric, ferroelectric, and pyroelectric susceptibilities, impedance spectroscopy can be used to probe phase transitions, minimize leakage current effects that often plague and convolute P-V tests, characterize intrinsic vs. extrinsic dielectric response, and provide preliminary insights into other coupled material susceptibilities [47,48]. In this work, I primarily investigated the dielectric permittivity as a function of DC bias, frequency, and temperature with an auto-balancing bridge impedance analyzer (E4990A, Keysight Technologies). In order to maintain the small-signal nature of this

measurement, AC excitation voltages were maintained below V_c and nonreversible regimes identified with standard Rayleigh measurements [49].

3.3.3.3 Current-Voltage Measurements

Current-voltage measurements were used in this work to confirm the various electrode contact types (Ohmic vs. Schottky) in tri-layer heterostructures, leakage densities, and resistance trends across various material compositions [50]. With use of an applied unswitched triangular waveform where a poling pre-pulse is applied in the same polarity of the following triangular voltage ramp, leakage density can be extracted. In this work, I used a precision Multiferroic Tester (Radiant Technologies, Inc.) to apply voltages between 1-4 V with delay, measurement, and soak times on the order 100 ms each.

3.3.4 Thermal Characterization

At the foundation of any pyroelectric characterization technique is the necessity for accurate temperature metrology and application. Here, I used thin-film resistive platinum heaters that can accurately deliver AC heating amplitudes between 3-30 K at various frequencies (10-10000 Hz) and background DC temperatures (5-500 K). To accurately quantify the resultant temperature delivered to an underlying thin-film stack by a resistive heater, a two-step, thermal coefficient of resistance and 3-omega based measurement is necessary. Finally, through careful consideration of thermal boundary conditions and thermophysical properties of an electrothermal test platform, the temperature and phase within any given underlying stack of a given depth can be extracted.

3.3.4.1 Temperature Coefficient of Resistance (TCR)

The first key thermal characterization measurement needed in quantifying applied temperature excitations to an underlying thin-film pyroelectric heterostructure is a relationship between applied AC heating current and resultant temperature response. To synthesize this bridge between the electrical and temperature phase spaces, the temperature of coefficient of resistance (TCR) must be quantified. Defined as the associated resistance change between two temperatures, the TCR value, denoted as α, can be defined within Eq. 3.7 [51] where R, T, and 0 subscripts refer to resistance, temperature, and initial value measured at 20 °C, respectively.

$$R(T) = R_0[1 + \alpha(T - T_0)] \qquad \text{(Eq. 3.7)}$$

Simply stated, by quantifying the slope of an R vs. T plot, α can be extracted. Despite this simplicity, attention must be given to extracting the zero-current resistance values to ensure additional joule heating is not incorporated into the measured resistance change. To carry out this measurement, I first applied a series of heating currents (20-120 mA) through a 3-omega based V-I converter circuit (discussed in the following section) across a 4-terminal resistive heater line and measured the resultant first harmonic voltage response at a given temperature. The applied voltage (*i.e.*, current via V-I converter) and corresponding voltage drop across the heater line were applied and measured via lock-in amplifier (Stanford Research Systems; Model SR830). The temperature of the sample was modulated *via*

conductive PLD substrate heater (Neocera) and measured by an adjacent substrate of equal thermal conductivity with a surface-mounted K-type thermocouple *via* silver-paint. Furthermore, to isolate electrical crosstalk between the measured TCR sample and underlying conducting PLD heater, both substrates were mounted and cured onto an Al_2O_3 10 x 10 mm substrate via silver paint. As such, the corresponding power dissipation could be calculated for any given applied heating current ($P = IV$) at a given temperature, which was then extrapolated back to I = 0 to reduce effects of joule heating arising solely during the measurement. After completing this process over a range of temperatures (25-40 °C), α was extracted for the platinum heater line. A platinum-based heater line was used due to its relatively linear R vs. T response across the 0-500°C temperature regime.

3.3.4.2 3-Omega Characterization Method

With the quantification of the TCR, further thermal characterization is needed to capture not only the resultant temperature change, but crucial phase information between the applied heating current and the resultant thin-film resistive heater temperature. To achieve this goal, I turned to well established methods of the thermal community, specifically, an adapted 3-omega method. The 3-omega method has been widely and traditionally used in the thermal community in the investigation of thermal conductivities (k) and volumetric specific heat (c) of thin-film materials [52-54]. In an effort to utilize such advanced thermophysical understandings of the community, I applied an adapted 3-omega method that can be used to quantify the temperature change of a thin-film heater line, in addition to necessary phase information for extracting the true pyroelectric response. The 3-omega method earns its name from the extraction of thermal information at the third harmonic of measured voltage. Namely, when applying an AC heating current to a circuit at a first harmonic $I_{1\omega}$, the resultant resistance change $R_{2\omega}$ arises at the second harmonic and thus temperature response (Joule heating) follows with the square of applied heating current. As such, by multiplying the current and resistance, one obtains a final voltage at the third harmonic, thus providing the link between the electrical and thermal regimes. To define this analytically and more generally, the $V_{n\omega}$, R, and I can be related *via* accordingly [55].

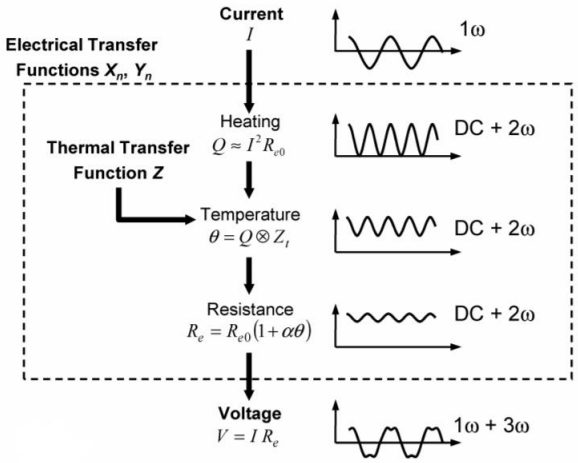

Figure 3.7: Flow diagram depicting the incident heating current (I) and resultant heating, temperature, resistance, and voltage response with accompanied sinusoidal functions [55].

$$\frac{V_{n\omega,rms}}{2\alpha R_0^2 I_{1,rms}^3} = X_n(\omega_1, \eta) + jY_n(\omega_1, \eta) \quad \text{(Eq. 3.8)}$$

Here, X_n and Y_n represent the in-phase and out of phase electrical transfer functions. Key to the power of such 3-omega-based methods is that the third harmonic electrical transfer functions are directly related to the thermal transfer functions (Z), thus providing the crucial

link between heating current and resultant temperature (Figure 3.7). To capture the necessary electrical-transfer functions, the third-harmonic voltage is measured across a range of incident heating current frequencies. Using the thermal circuit geometry described previously (orange, Figure. 3.2), the two top outer probe pads are used to deliver the required heating current while the two bottom inner probe pads are used to measure the resultant voltage across the heater line. With a home-built 3-Omega measurement circuit I fabricated for this work (Figure 3.8), five main components are needed. First, the measurement circuit consists of two operational amplifiers (OPA551), two signal conditioning chips (AD7541A), and a potentiometer located between the operational amplifiers. The operational amplifiers and signal conditioning chips are used as the V-I transducer and single line outputs necessary for compatibility with the lock-in amplifier. In the case of the potentiometer, this component is used to null a bridge in order to minimize the large $V_{1\omega}$ signal that can often interfere with the relatively small $V_{3\omega}$ response.

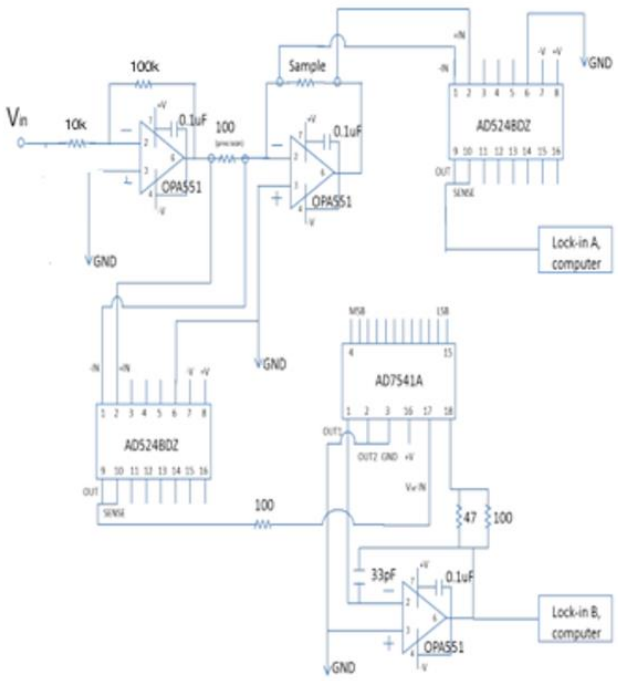

Figure 3.8: Electrical circuit diagram of the 3-Omega based method for quantifying both resultant AC temperature phase and amplitude for a thin-film resistor [56].

Following the collection of the in-phase and out-of-phase $V_{3\omega}$ response, the previously established TCR value is used to calculate the final AC temperature oscillation amplitude and phase of the heater line at each given frequency. With this information in hand, the temperature amplitude and phase within any given layer of the underlying pyroelectric must also be calculated. Using the solution to the heat-diffusion equation, a 1-dimensional heat transport assumption can be maintained with the given heater half width (b) and film thickness geometry (*i.e.*, b>>0.5um) of the thermal circuit. Using the steady, periodic solution of the heat-diffusion equation [57], heat transport across a single domain can be calculated by the following matrix relation:

$$\begin{bmatrix}\theta_d \\ q_d\end{bmatrix} = \begin{bmatrix} cosh\,(\gamma d) & \frac{-1}{k\lambda} sinh\,(\gamma d) \\ -k\lambda sinh\,(\gamma d) & cosh\,(\gamma d)\end{bmatrix}\begin{bmatrix}\theta_0 \\ q_0\end{bmatrix} \qquad \text{(Eq. 3.9)}$$

where θ, q, d, k, and γ refer to the temperature amplitude, heat flux, layer thickness, thermal conductivity, and $\gamma = \sqrt{j\omega/D}$, respectively ($D$ is the thermal diffusivity and $j = \sqrt{-1}$). As a result, with quantification of the initial temperature amplitude and heat flux, an underlying layer can also be quantified with the necessary thermophysical properties. Recursively applying this solution to multiple domains (*i.e.*, multiple thin-film layers in a pyroelectric

heterostructure) allows one to quantitatively "walk" down a thin-film stack and quantify temperature amplitude in the desired layer depth. Lastly, to account for the atomically pristine interfaces between *insitu* deposited thin-film layers, a 1-nm interface was inserted into the model between heterostructure layers with thermal conductivity and heat capacity of 1 W m^{-1}- K^{-1} and 10^5 J m^{-3} K, respectively.

3.3.4.3 Thin-Film Pyroelectric Characterization

Since the 1950s, more than twenty pyroelectric measurement protocols have been developed taking advantage of various excitation/measurement signals and required device and material specifications (*i.e.*, area, thermal conductivity, specific heat capacity, etc.) that have offered varying abilities to separate out spurious effects such as thermally stimulated currents [58]. The relative lack of advanced study on thin-film pyroelectrics is primarily related to the fact that direct (and accurate) measurements of applied temperature changes are difficult. The small thermal mass/area of thin-film devices and the presence of underlying substrates lead to non-trivial boundary conditions where the film loses heat to the substrate at relatively short time scales [59]. In general, pyroelectric measurements can be classified as either "direct" or "indirect" depending on how the temperature dependence of P is extracted. Direct measurements involve characterization of the temperature dependence of P directly via the pyroelectric current or voltage. In the case of a closed-circuit configuration of a parallel-plate device used in this work, the temperature stimulus and the concomitant change in P result in a flow of current through the external circuit due to a change in the compensating charges of the electrodes. By monitoring the pyroelectric current in response to the applied temperature, the pyroelectric coefficient can be extracted directly,

$$\pi = \frac{i_p}{A * dT/dt} \qquad \text{(Eq. 3.10)}$$

where i_p is the pyroelectric current, A is the capacitor area, and t is the time. In contrast, indirect measurements are accomplished via multiple isothermal measurements of polarization-electric field hysteresis loops as a function of temperature. The temperature dependence of polarization ($\partial P/\partial T$) is then extracted to obtain π. Indirect measurements are simpler to implement, but can lead to an overestimation of π due to electric-field-induced leakage currents and insensitivity to various contributions to pyroelectricity (*e.g.*, *extrinsic*, *secondary*, or field-dependent effects) which can be particularly significant for thin-films. While direct measurements offer a higher degree of accuracy, they are also more difficult to implement. Rapidly and uniformly applying temperature variations, measuring those temperature changes accurately in complex material stacks, and measuring the potentially small currents (voltages) that result from the pyroelectric effect is non-trivial. In thin films, these challenges are further exacerbated due to the reduced lateral sizes of devices (rendering traditional thermocouple-based studies nearly impossible) and the small signal pyroelectric response itself which can be beyond the resolution of off-the-shelf instruments. The key, however, is that the approach must be able to address potentially spurious contributions to the response including thermally stimulated or leakage currents.

To overcome these various challenges, I utilize the microfabricated electrothermal test platforms introduced in Section 3.2 of this work to directly extract the pyroelectric response with an AC, phase-sensitive technique [60]. With use of a 10 μm x 270 μm thin-film resistive platinum heater (80-nm-thick), a sinusoidally varying temperature can be homogeneously applied to the underlying pyroelectric thin-film at frequencies of 5 Hz-5 kHz (Figure 3.3). Using an AC-current source (Keithley 6221), 10 mA RMS current $I_{0H}\cos(\omega_H t)$ is driven across the heater line at the desired frequency (ω_H). With the current source trigger referenced to a lock-in amplifier (Stanford Research Systems, SR830), the resultant total electrical current is measured at the second harmonic ($2\omega_H$) where the temperature oscillations due to joule heating are being delivered to the thin-film. To minimize capacitive effects, the bottom electrode of the test platform is connected to the current input (10^6 V/A gain) of the lock-in amplifier while the top electrode is routed to a waveform function generator (Keysight 33500B) where the potential is kept at ground. Additionally, this function generator can be used to apply DC voltages when investigating the electric field dependence of the pyroelectric response. Key to the accuracy of this AC, phase-sensitive method is the ability to measure not only the total collected current from the test platform due to AC heating, but the ability to extract the necessary phase information from the various sinusoidal current and temperature signals. Due to the time-derivative dependence of temperature, one can effectively separate out the true pyroelectric current (which is 90° out-of-phase with the input heating signal) from thermally stimulated currents (TSCs) [61,62] that arise from thermally excited trapped charges (which are in-phase with the input heating signal). As compared to pyroelectric current, TSC has a large relaxation time (orders of magnitude longer than pyroelectric currents) and therefore depends more on the actual temperature and less on its time derivative. This distinguishing feature arms the pyroelectric measurement with phase selectivity during periodic (AC) heating. Thus, combining the previously defined temperature amplitude and phase information from the 3-omega and TCR methods, the true pyroelectric current component can be extracted.

In all, accurately investigating the complex and convoluted pyroelectric response of thin-film oxides requires control of numerous parameters associated with material processing, synthesis, device fabrication, and phase-sensitive metrology. From synthesis of the primary ceramic oxide pellets used for PLD, resultant thin-films are screened for the required stoichiometry, crystal structure, material phase, surface/domain morphology, and electrical properties. Furthermore, integration of PLD-grown heterostructures into electrothermal test platforms necessary for pyroelectric characterization consists of numerous photolithography steps, material deposition methods (PE-CVD and PVD), and etching techniques (ion beam etch and reactive ion etch). Once completed, further thermal characterization is used to quantify the applied temperature amplitude and phase lag between applied heating current and resultant temperature response (TCR and 3-omega). With critical phase-sensitive characterization and thermal modeling, the pyroelectric response of thin-films can be accurately extracted. This nontrivial path of material synthesis, processing, and characterization is what challenges the investigation of thin-film pyroelectric response. Nonetheless, when the proper measurement protocols are applied, a rare look into the deep structure-property physics of pyroelectrics can be obtained.

Chapter 4

Intrinsic and Extrinsic Contributions to Susceptibilities in Ferroelectrics

In this Chapter, I introduce the concept of both intrinsic and extrinsic components to the total response of dielectrics, piezoelectrics, and pyroelectrics. Building from the work and learning in studies of dielectric and piezoelectric materials, I adapted methodologies to quantitatively extract the extrinsic (*i.e.*, domain-wall based) contribution to pyroelectricity and elucidate the evolution across various ferroelectric domain architectures induced by varying epitaxial strain states.

4.1 Intrinsic and Extrinsic Contributions in Dielectrics and Piezoelectrics

Before we begin to understand the various complex contributions to the total pyroelectric response, I will first describe how analogous effects in dielectric and piezoelectric responses came to be defined by their respective communities. Dielectric ceramics comprise a large and actively growing portion of the micro- and nano-electronic fields (*e.g.*, capacitors, transducers, memristors, and transistors) where the increasingly high electrical insulating properties and dielectric polarization under applied electric fields can be readily utilized [1]. Furthermore, due to the material class hierarchy previously introduced in Chapter 2, dielectric susceptibility inherently accompanies the complex ferroelectric and pyroelectric oxides of this work. As such, the relatively unique properties of ferroelectrics introduce a diverse set of unconventional dielectric property response which can be readily tuned while present in thin-film form. One key distinguishing aspect of epitaxial, thin-film ferroelectrics is the presence of ferroelectric and ferroelastic domain structures in response to the applied mechanical strain induced via underlying substrates. Unsurprisingly, the given domain architecture can have profound effects on the resulting dielectric response as compared to monodomain counterparts, specifically under applied DC electric fields [2,3], temperatures [4], and electrical excitation frequencies [5,6]. To distinguish ferroelectric domain-driven effects from the measured dielectric susceptibility, the concept of intrinsic and extrinsic contributions has been introduced by the community.

$$\varepsilon_{total} = \varepsilon_{extrinsic} + \varepsilon_{intrinsic} \quad \text{(Eq. 4.4)}$$

In this context, the intrinsic contribution to dielectric permittivity arises due to the bulk polarization response (within a domain, for example) of a given material under applied electric fields. Specifically, in the case of prototypical ferroelectrics such as $BaTiO_3$, intrinsic dielectric response refers to the increased average dipole moment *via* cation-anion and electron displacement from equilibrium perovskite crystal positions. Additionally, in the case of dielectric systems that maintain polar order, the subsequent field-induced domain-wall motion and corresponding reorientation of polarization is defined as the extrinsic contribution . In general, there are two primary routes to quantify and investigate extrinsic contributions in ferroelectric systems. To begin, we must understand that domain-wall motion is an energetically activated process. As such, through the reduction of thermal energy in a system at low temperatures (5-10 K), domain-wall motion can be effectively quenched; allowing for intrinsic dielectric response to be measured independently [7,8]. Furthermore, an additional route to quench domain-wall motion arises from the application of large DC electric fields. These high applied fields dependent on material saturation polarization voltage)) act to drive the system towards monodomain configurations or domain configurations not susceptible to small AC-field perturbations of dielectric measurements , and thus similarly allow for the independent measurement of the intrinsic response [9,10]. By carefully measuring the

frequency response of the dielectric permittivity under various applied DC fields, two distinct permittivity regimes can be identified, confirming the suppression of extrinsic effects at high fields. Nonetheless, to further probe the extrinsic effects in dielectrics, numerous studies have relied on Rayleigh-based methods that utilize small AC signal excitations to perturb dielectric response [11,12]. In this methodology, the Rayleigh Law

$$\varepsilon_r = \varepsilon_{init} + \alpha E_0 \qquad \text{(Eq. 4.5)}$$

can be used to suitably describe the non-linear, and hysteretic nature of dielectric response in ferroelectric systems. Here, E_0, ε_{init}, and α refer to the AC applied electric field amplitude, reversible (linear), and irreversible (non-linear) domain-wall components to the total extrinsic response, respectively. To quantify these components, and thus the overall presence of extrinsic contributions to dielectric permittivity, the applied electric field in the linear regime is plotted against the total measured response and fit to extract the necessary Rayleigh coefficients (Figure 4.1). To further provide insights to extrinsic dielectric contributions, previous studies have also turned to combining both low-temperature and AC-perturbation Rayleigh studies [13].

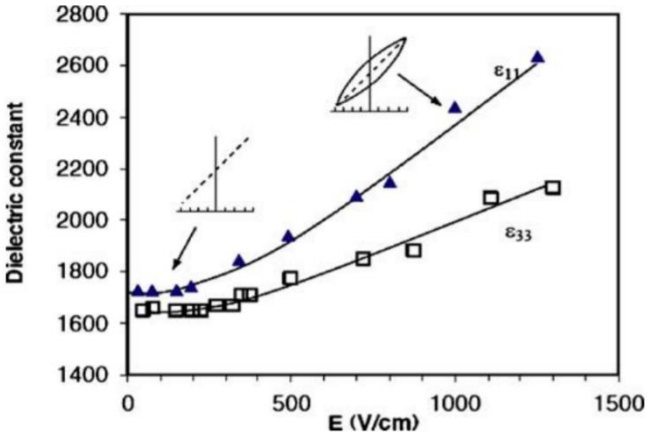

Figure 4.1: Dielectric permittivity (ε_{11}, ε_{33}) as a function of applied AC electric field for a $PbZrTiO_3$ ceramic. A low-field and high-field regime are present, indicating a reversible and non-reversible domain-wall response [11].

Similar to its dielectric counterpart, piezoelectrics also exhibit intrinsic and extrinsic contributions to the total measured response. Rather than changes to dielectric permittivity, however, these various contributions affect the resultant piezoelectric coefficient of the material ($d_{ij} = \frac{\partial P}{\partial X}$) which is thermodynamically defined by the applied mechanical stress X and resultant polarization P change. In this case, the Rayleigh law may still be universally applied to define both the reversible and irreversible components of d,

$$d' = d_{init} + \alpha_d E_0, \qquad \text{(Eq. 4.3)}$$

where, similar to dielectrics, d_{init} and α_d now refer to the reversible and irreversible domain-wall contributions to d. Using the methodologies developed by the dielectric community, the extrinsic contribution to piezoelectricity cannot only be characterized via AC-electric field excitation (E_0) and the application of low temperatures [11,14-16], but also AC mechanical stresses (X_0) that act to pin the movement of thermally and mechanically active domain walls [17]. As a result, the main distinguishing factor between extrinsic contributions to piezoelectricity and dielectrics is the type of active domains and domain walls present in the material. Namely, in order for a domain to be "extrinsically" active in a piezoelectric, a concomitant change in volume and, subsequently, strain is required. Therefore, purely

ferroelectric (180°) domains do not contribute to extrinsic piezoelectricity as they do in dielectrics, but rather only ferroelastic (non-180°) domains with associated strain [18,19].

Unsurprisingly, increased efforts have aimed to harness control of the domain architecture of thin-film ferroelectrics to systematically tune and enhance both dielectric and piezoelectric response. Fundamentally, ferroelectric and ferroelastic domain formation in epitaxial thin films is a direct result of the minimization of free energy, specifically balancing both electrostatic and elastic energies [20]. With this in mind, the community has turned towards controlling both the strain state and electrical boundary conditions of ferroelectrics to define the desired domain structure. In regard to the applied strain state, introducing lattice mismatch between epitaxial thin films and underlying substrates one can impose >±1% strain, allowing for the deterministic formation of ferroelectric and ferroelastic domains [21]. In the case of the PZT- and BTO-based systems of this Dissertation, accompanying Ginzburg-Landau-Devonshire (GLD) phenomenological modeling has paved the way to understanding the various types of domain states and the respective dependence on temperature [22-24]. In general, there are two conventional domain states found in prototypical PZT-based film grown on (001)-oriented substrates. Briefly, *c* domains consist of regions within the ferroelectric that maintain out-of-plane oriented polarization (normal to the substrate) while *a* domains maintain in-plane oriented polarization (in the plane of the film) (Figure 4.2 Insets) [25,26]. To bridge the elastic energy costs across applied strain regimes, thin-film systems additionally exhibit mixed-domain regions where combinations of *c* and *a* domains may coexist simultaneously [27]. Through substrate- or compositional-gradient-induced strain engineering, novel domain architectures can be synthesized to extrinsically tune and enhance built-in potentials [28], switching kinetics [29], piezoelectric response [30], and the dielectric permittivity over orders-of-magnitude [31]. With devoted efforts towards thin-film engineering and ferroelectric-domain control for both dielectric and piezoelectric response, the question arises whether thin-film pyroelectrics also maintain such susceptibilities.

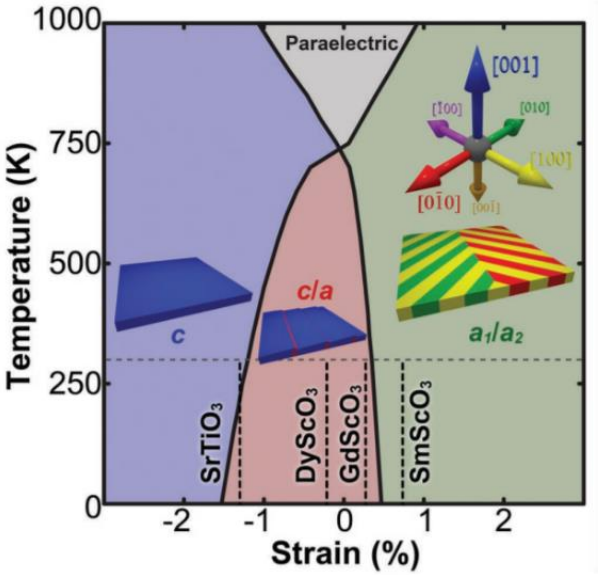

Figure 4.2: Phenomenological model of thin-film domain structure dependence on epitaxial strain and temperature for $PbTiO_3$ systems. Insets display 3-dimensional depictions of *c*- and *a*-domain orientation in addition to the strain applied by various substrates [24].

4.2 Low-Temperature Dielectric and Pyroelectric Response

To harness the extrinsic contribution extraction methodologies developed by the dielectric and piezoelectric communities, I initially explored the use of low temperature pyroelectric measurements with the intent of "freezing out" domain wall motion, and thus suppressing extrinsic contributions to pyroelectricity. In order to access the temperatures needed to minimize domain wall motion (<20 K) [13], I turned to the use of a physical property measurement system (PPMS), which is traditionally used to study both the magnetic and electrical transport properties of materials (Cryogenic Ltd.). Making use of its cryogenic cooling capabilities (able to go to ~2 K), I mounted and wire bonded the top and bottom electrode connections from the pyroelectric test platforms of Chapter 3 onto a ceramic 10 mm square die, leadless chip carrier (Kyocera Spec AS-1004) using .001-inch gold wire. In this study of extrinsic domain-wall response, I used a 120-nm-thick $PbZr_{0.2}Ti_{0.8}O_3$ film sandwiched between a bottom and top $Ba_{0.5}Sr_{0.5}RuO_3$ electrode (20-nm-thick) grown on $GdScO_3$ substrate via PLD. With an average biaxial strain of -1.02% imposed by the underlying $GdScO_3$ substrate, a *c*/*a* domain structure is theoretically expected [24]. To ensure sufficient thermal contact, the post-processed heterostructure was mounted to the chip carrier via silver paint and cured at 80°C. Before implementing the AC, phase-sensitive pyroelectric measurement methodology, both the ferroelectric and dielectric properties were first measured. Within Figure 4.3a, the remanent polarization (P_r) extracted from PE loops (1

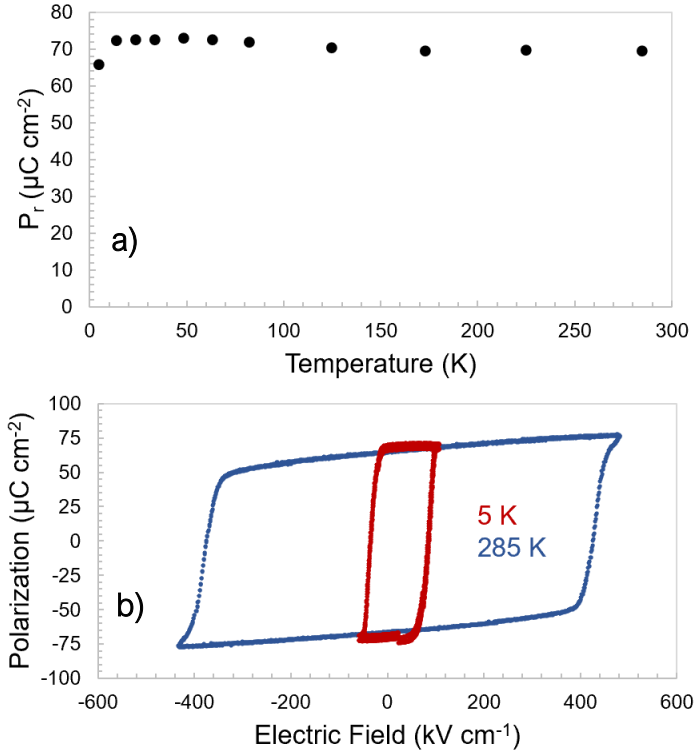

Figure 4.3: Temperature dependence of both a) remanent polarization P_r and b) PE hysteresis loop for a 120-nm-thick $PbZr_{0.2}Ti_{0.8}O_3$ pyroelectric film measured at 5 kHz frequency.

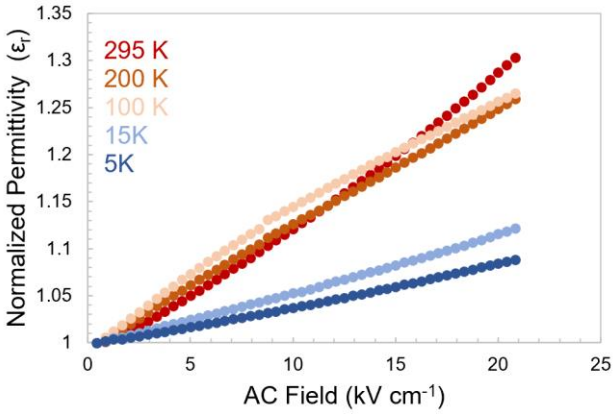

Figure 4.4: Normalized dielectric permittivity as a function of applied AC electric field and temperature for 120-nm-thick $PbZr_{0.2}Ti_{0.8}O_3$ pyroelectric.

kHz, Figure 4.3b) are plotted as a function of temperature. Here, we see not only an increasing V_c at reduced temperatures which follow previous reports [13], but additionally a slight decrease of P_r below ~30 K. We can understand the increase of V_c at lower temperatures from an energetic standpoint. Namely, V_c denotes the necessary voltage threshold to invert, and thus switch the polarization direction within a ferroelectric. This threshold can be physically understood as the stability and resistance of domain walls to an applied electric field. As a result, an increasing applied voltage is needed to compensate for the lowered thermal energy of the system at lower temperatures. This phenomenon, although to a lower degree, has also similarly been seen through the frequency dependence of V_c during PE hysteresis loop measurements where a longer applied voltage (*i.e.,* lower frequency) can effectively switch ferroelectric domains at a lower energy cost, thus lower V_c (Chapter 3). Next, I began the investigation of the temperature dependence of the dielectric permittivity. With proper care to minimize line and stray capacitance of the PPMS, the permittivity of the chip-mounted electrothermal test platform could be measured *via* an impedance analyzer. As described in Figure 4.4, the normalized permittivity as a function of applied AC electric field is observed, similarly to previous methods of Xu *et al.* [13]. As expected, the slope of dielectric response is found to decrease at lower temperatures as extrinsic contributions are suppressed. Additionally, it is evident that extrinsic suppression is minimal at and above the 100 K regime where domain-wall motion is still relatively active.

With the validation of expected ferroelectric and dielectric susceptibility response at lower temperatures, I next directed attention towards understanding the extrinsic pyroelectric response. With the thin-film $PbZr_{0.2}Ti_{0.8}O_3$-based electrothermal test platform used in the previous dielectric study, additional gold wirebonds were fabricated to allow access to the 4-terminal resistive platinum heater line. Applying 10 mA RMS heating current at 1 kHz, the pyroelectric current i_p was collected at various temperatures down to 5 K as a function of various applied DC biases (Figure 4.5). It was observed, similar to the PE hysteresis response, that the magnitude of pyroelectric current decreased and the V_c increased at reduced temperatures. Following analogous arguments for ferroelectric response, the remanent pyroelectric current, which is proportional to π, is expected to decrease upon cooling due to the reduction of domain-wall contributions in addition to the intrinsic reduction of $\frac{\partial P}{\partial T}$ as one approaches 0 K which is most commonly depicted as the slope of polarization in ferroelectric P vs. T diagrams. In terms of the temperature dependence of V_c, the previously defined argument of thermal activation of domain-wall motion still holds. In order to convert the collected pyroelectric current into π,

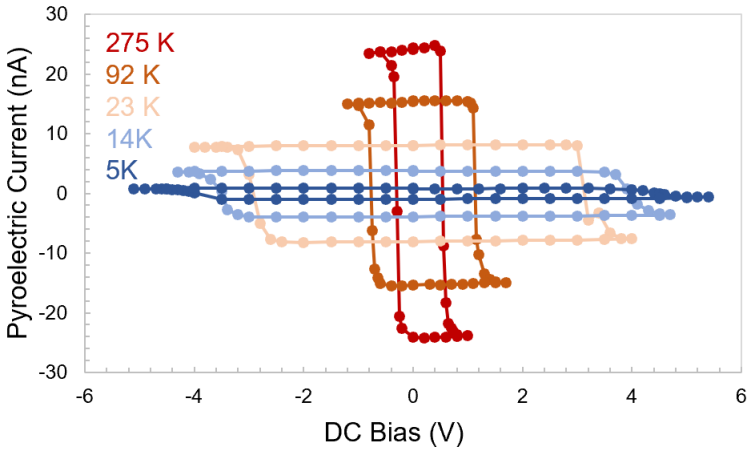

Figure 4.5: Collected pyroelectric current hysteresis loops from 120-nm-thick $PbZr_{0.2}Ti_{0.8}O_3$ pyroelectric as a function of applied DC bias and temperature.

the TCR and 3-omega based measurements of Chapter 3 would have to be applied. Unfortunately, at temperatures below ~50 K, a few challenges arise in accurately characterizing the AC temperature amplitude of a thin-film resistive heater line. First, as the TCR is measured at increasingly lower temperatures, non-linearities in platinum resistance (arising from the residual resistance of the metal) in addition to increasing contributions of joule heating during calibration occur (Figure 4.6). Furthermore, both the AC and DC temperature amplitudes must now also be considered. Namely, under an applied AC heating current, both a resultant increase of DC temperature and AC temperature amplitude are present. Intuitively, if an AC temperature amplitude is applied at a given background temperature, the magnitude of temperature oscillation cannot fall below the starting background temperature (*i.e.,* cooling is not possible). This resultant increase of background temperature arises from the DC component of the applied heating current and can be analytically determined from the in-phase components of $V_{1\omega}$ and $V_{3\omega}$ [31].

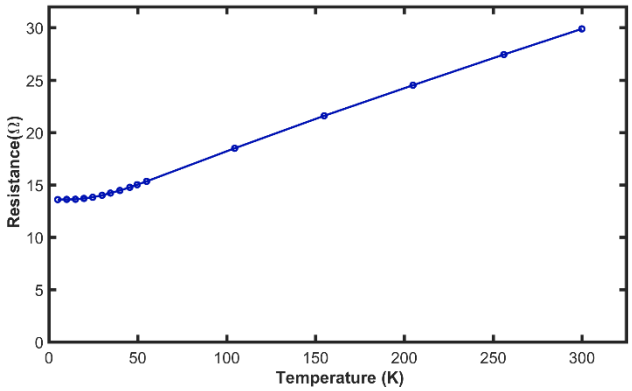

Figure 4.6: Temperature dependence of 4-point probe resistance on 80-nm-thick platinum thin-film resistive heater line.

$$\theta_{DC} - \frac{1}{\sqrt{2}}\theta_{2\omega,cos,rms} = \frac{V_{1\omega,rms,in\ phase} - I_{1\omega,rms}R_0}{\alpha I_{1\omega,rms}R_0} \qquad \text{(Eq. 4.4)}$$

At room temperature heating, the DC component comprises only a small fraction of the total background temperature. As compared to temperatures near 5 K, the introduction of even a nominal AC temperature amplitude (*e.g.*, 4 K peak-to-peak) can inadvertently introduce a 2 K DC temperature rise which amounts to almost a 50% increase of background DC temperature. With this in mind, in order to achieve true pyroelectric measurements at DC temperatures at or below 5 K, not only would a sub-5 K DC temperature need to be obtained, but only minute AC temperature amplitudes could be applied; limiting pyroelectric current responses to well below measurable values (< pA). Evidence of these effects can be clearly identified when the collected pyroelectric current is normalized to a nominal applied temperature oscillation amplitude ($T_{osc} = 0.32\ K$) as a function of temperature oscillation amplitude (Figure 4.7). Unlike the linear trends of 23 K and above, the 5 K normalized pyroelectric

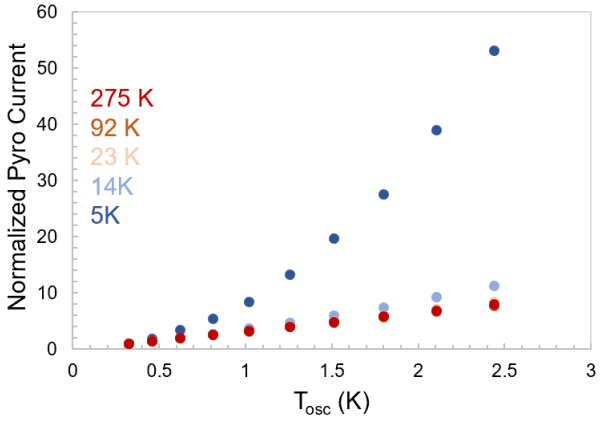

Figure 4.7: Normalized pyroelectric current as a function of applied temperature oscillation amplitude of $PbZr_{0.2}Ti_{0.8}O_3$ thin film.

current shows a nonlinear response, indicative of increasing DC temperature components at higher applied AC temperature oscillations. In all, with the established methodologies of extrinsic contribution extraction from both the piezoelectric and dielectric communities, the field of pyroelectrics stands poised to investigate and control the domain-wall mediated contributions to pyroelectric response. Although the application of AC, phase sensitive metrology introduces non-trivial challenges to extrinsic contribution suppression at low temperatures, other, more accessible routes must be explored.

4.3 Effect of Ferroelastic Domains on Pyroelectricity in $PbZr_{0.2}Ti_{0.8}O_3$ Thin Films

4.3.1 Introduction

The coupled and complex interaction of temperature and polarization in ferroelectric materials allows for a plethora of next-generation applications such as waste-heat energy conversion [2,3] and solid-state cooling [32,33]. Key to the realization of such advanced developments lies in the ability to accurately control and enhance pyroelectric response. Traditionally, efforts have aimed at perching pyroelectrics near temperature or compositional phase transitions, similarly to dielectric and piezoelectric counterparts, where respective susceptibilities diverge and are maximized [34-38]. Only within the past two decades have advances in thin-film engineering, specifically epitaxial strain, been used to manipulate ferroelectric order, ferroic susceptibilities [39-41], and domain structures [25,42,43]. As a result, although dedicated efforts have been focused on experimentally elucidating such domain-based effects to dielectric and piezoelectric response, the field of pyroelectrics has primarily been limited to only computation and modeling insights due to the complexities of accurate experimental metrologies. As such, with phenomenological Ginzburg-Landau-Devonshire-based (GLD) methods, the extrinsic contribution to polydomain ferroelectrics, which have traditionally been neglected, have now been calculated to appreciable magnitudes. Similar to the polarization instabilities of phase transitions, GLD efforts have confirmed that domain-structure boundaries between c to c/a and c/a to a_1/a_2 maintain enhanced susceptibilities [44,45]. Nonetheless, in order to elucidate the true nature of extrinsic effects to pyroelectricity within thin-film, polydomain ferroelectrics, a systematic experimental investigation spanning the entire strain-induced phase space is required.

In this work, an alternative methodology was applied to extract the extrinsic contribution to pyroelectricity without the complications that arise at low temperature, AC phase-sensitive techniques. Here, the contribution of ferroelastic domains to pyroelectric response is experimentally investigated within the $PbZr_{0.2}Ti_{0.8}O_3$ prototypical tetragonal ferroelectric. With control of the applied epitaxial strain from underlying substrates, a diverse set of ferroelastic polydomain structures can be stabilized. Using temperature-dependent scanning-probe microscopy, and AC phase-sensitive pyroelectric measurements described in Chapter 3, the reconfiguration of domain architectures under temperature perturbations can be quantitatively investigated. As a result, domain-wall based (*i.e.* extrinsic) contributions to pyroelectricity due to the interconversion of various domain populations is elucidated as a function of epitaxial strain. Findings confirm that under compressive strain, temperature- and electric field-driven domain interconversion works to reduce pyroelectric response while tensile strains work in the exact-opposite effect to enhance the extrinsic effects to pyroelectricity.

4.3.2 Domain Evolution Under Various Strain States

To capture the strain and temperature evolution of ferroelectric/ferroelastic domain structures, this work (completed together with my colleague S. Pandya) focused on the canonical (001)-oriented tetragonal $PbZr_{0.2}Ti_{0.8}O_3$ which has demonstrated a diverse set of equilibrium domain configurations [46,47]. Namely, 120 nm $PbZr_{0.2}Ti_{0.8}O_3$/ 20 nm $Ba_{0.5}Sr_{0.5}RuO_3$ / $TbScO_3$ (110), $GdScO_3$ (110), $SmScO_3$ (110), $NdScO_3$ (110), and $PrScO_3$ (110) heterostructures were grown using PLD. These substrates provide an anisotropic in-plane lattice mismatch (ε_{xx} and ε_{yy}) with the room-temperature $PbZr_{0.2}Ti_{0.8}O_3$ and $Ba_{0.5}Sr_{0.5}RuO_3$ pseudocubic lattice parameters [48]. To simplify the elastic constraints imposed by the underlying substrates, an average biaxial strain ($\varepsilon_m = 0.5(\varepsilon_{xx} + \varepsilon_{yy})$) will be used to describe the $TbScO_3$ (-1.26%), $GdScO_3$ (-1.02%), $SmScO_3$ (-.02%), $NdScO_3$ (-

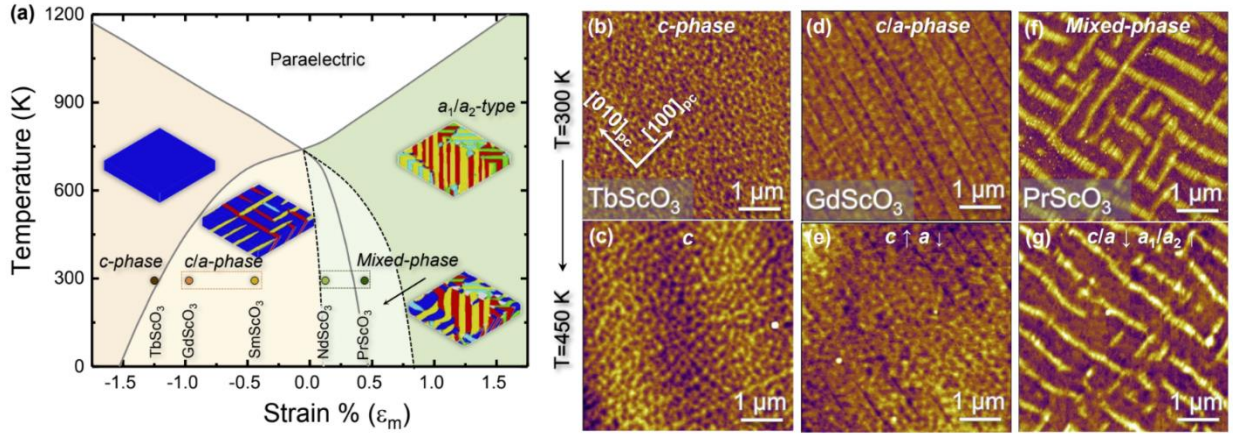

Figure 4.8: a) GLD-based temperature-strain phase diagram depicting the various equilibrium domain structures for $PbZr_{0.2}Ti_{0.8}O_3$ (*i.e., c*, *c*/*a*, and *a*1/*a*2). The dots indicate the pseudocubic strain positions for the substrates of this work.b, d, f) AFM topography of the $PbZr_{0.2}Ti_{0.8}O_3$ film grown on TbScO3 (b), GdScO3 (d), and PrScO3 (e) at 300 K. c, e, g) AFM topography of the $PbZr_{0.2}Ti_{0.8}O_3$ film grown on TbScO3 (c), GdScO3 (e), and PrScO3 (g) at 450 K.

.02%), and $PrScO_3$ (+0.26%) strain states. Through the support of experiments and phenomenological/phase-field models, it has been consistently observed that an evolution of purely out-of-plane oriented *c*-domains at compressive strains to a purely in-plane oriented a_1/a_2 domain configuration at highly tensile strains may be achieved. To bridge these two orthogonal domain structures, intermediate strain states have additionally exhibited polydomain *c*/*a* and mixed phase coexistence of both *c*/*a* and a_1/a_2-domain structures (Figure 4.8a) [25]. Nonetheless, based off these thermodynamic formalisms, key differences in the temperature dependence of each domain regime can be identified. Namely, within the *c*-phase, it is clear that upon heating from room temperature; no changes in domain configurations are expected. Contrarily, while perched in the *c*/*a* phase, increase temperatures lead to an interconversion to a purely monodomain *c* phase. In the same sense, heating of the mixed-phase tensile regime induces a transition toward the purely in-plane oriented a_1/a_2 phase. Lastly, under high tensile strains, no domain configuration interconversion is expected during heating. To confirm these phenomenological trends, the room-temperature domain structure of each strain state was imaged via atomic force microscopy. As displayed at 300 K (Figure 4.8b), the heterostructures grown on $TbScO_3$

(110) exhibit a conventional monodomain, out-of-plane polarized *c*-domain structure that remains unaltered at higher temperatures (450 K, Figure 4.8c). Furthermore, both the $GdScO_3$- and $SmScO_3$-based heterostructures ($GdScO_3$ shown for brevity) exhibit a *c*/*a* configuration (Figure 4.8d) that reveal a decreasing *a*-domain fraction upon heating (Figure 4.8e). Transitioning towards the tensile regime, both the $NdScO_3$ and $PrScO_3$ heterostructures ($PrScO_3$ shown for brevity) confirm the presence of a mixed-phase regime where both the *c*/*a* and a_1/a_2 domain configurations coexist simultaneously (Figure 4.8f). As expected, during heating to 450K the interconversion to a_1/a_2 structures at the expense of *c*/*a* is evident through the reduction of orthogonal, yellow-white surface morphology regions (Figure 4.8g). In all, the polydomain phenomenological model provides a self-consistent description of equilibrium domain states at various applied mechanical strains and temperatures.

4.3.3 Strain Evolution of Ferroelectric and Dielectric Properties

Confirming the equilibrium domain configurations on the various heterostructures, in addition to the respective temperature evolution, attention was next directed towards exploring these

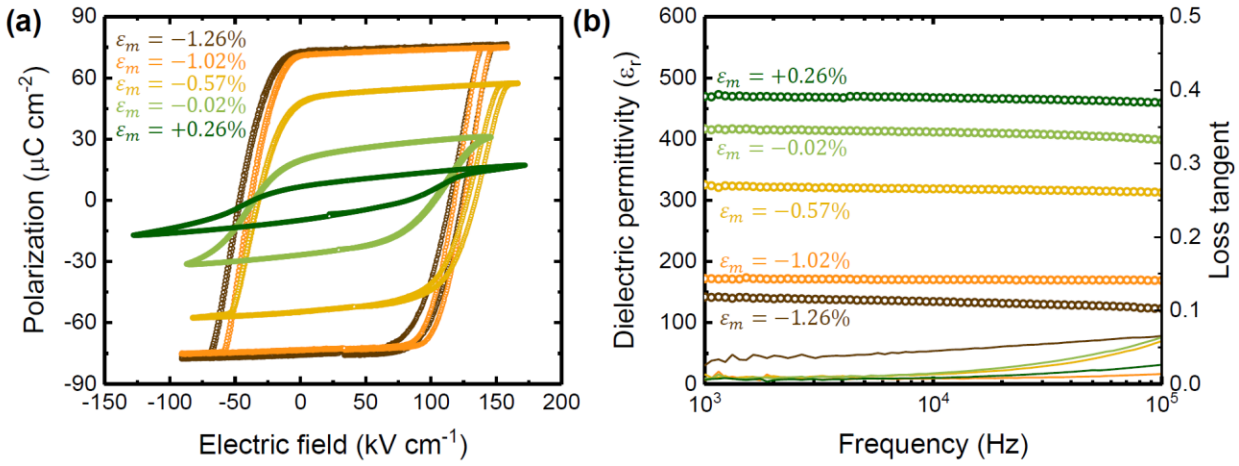

Figure 4.9: a) PE hysteresis loops for the various heterostructures. b) Frequency dependence of the dielectric permittivity (left axis) and loss tangent (right axis) for the various heterostructures. Brown, orange, yellow, light green and dark green refer to $TbScO_3$, $GdScO_3$, $SmScO_3$, $NdScO_3$, and $PrScO_3$,

various extrinsic effects to ferroelectric and dielectric susceptibility. Utilizing the established processes of Chapter 3, all heterostructures were integrated into thin-film electrothermal test platforms. Using only the top and bottom electrode connections initially, ferroelectric PE hysteresis loops and dielectric permittivity as a function of AC frequency were measured (Figure 4.9). Following the trend of out-of-plane oriented *c*-domain density, remanent polarization is seen to decrease as the tensile a_1/a_2 regime is approached. Conversely, due to the enhancement of dielectric permittivity from in-plane oriented *a*-domains, maximum response is exhibited by the $NdScO_3$ and $PrScO_3$ mixed-phase heterostructures [49].

4.3.4 Strain Evolution of Extrinsic Contributions to Pyroelectricity

To begin investigating the extrinsic effects to pyroelectricity, knowledge of the other additional contributions must be obtained to ensure the proper deconvolution methodologies. As described in part above, the total measured pyroelectric response consists of contributions not only from domain-wall motion (extrinsic), but additionally from thermal expansion mismatch to underlying substrates (secondary) and bulk polarization response of the system (intrinsic). To independently characterize and isolate only the extrinsic response, suppression of the secondary response was first explored. During the application of a periodically oscillating temperature amplitude from a thin-film resistive heater,

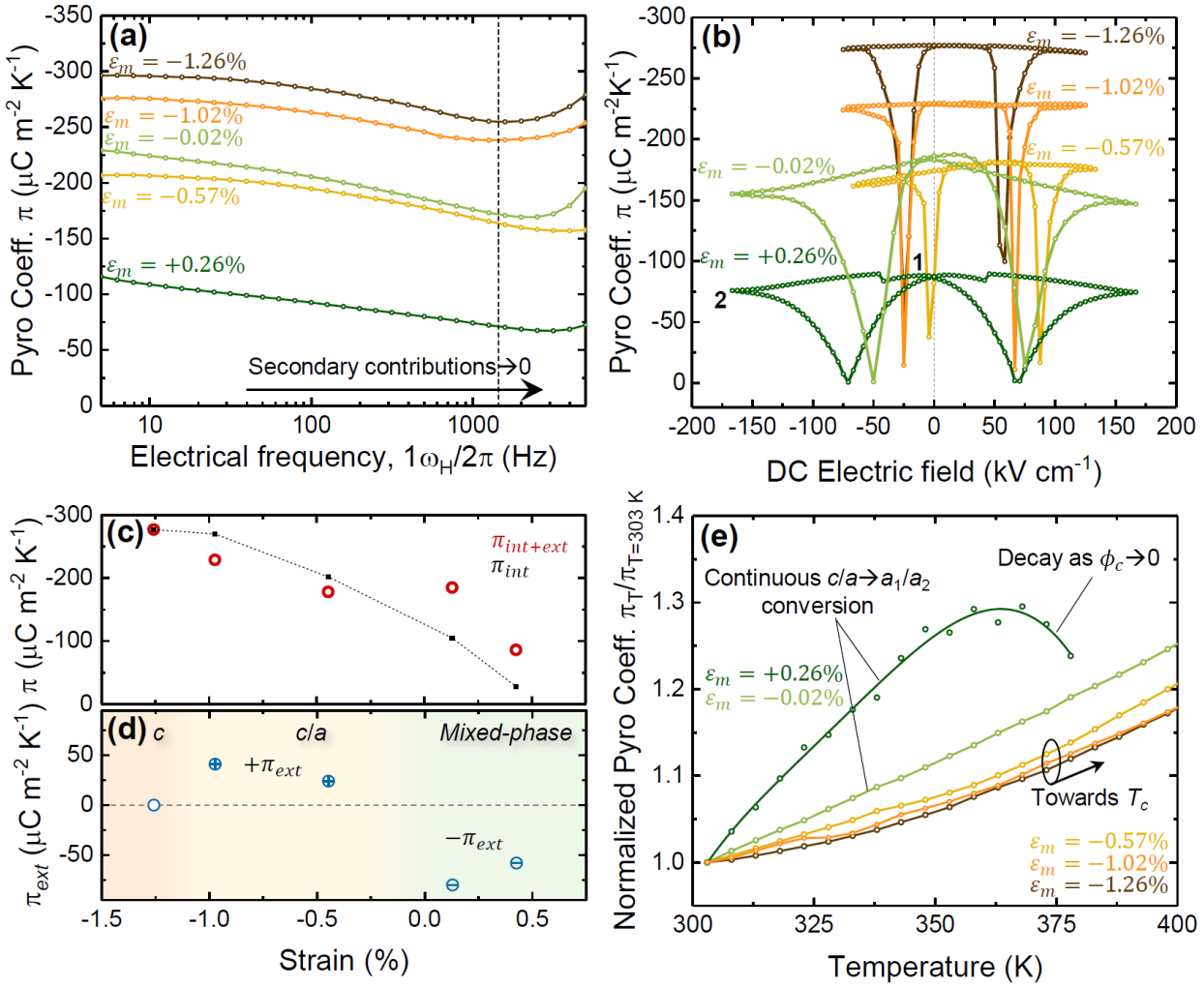

Figure 4.10: a) Frequency dependence of the pyroelectric coefficient for the variously strained heterostructures. b) DC-bias dependence of the pyroelectric coefficient across the various strain states, depicting traditional "butterfly" loop switching and dielectric contributions to pyroelectricity at increasing fields. c) Theoretically calculated intrinsic (black dashed line) and intrinsic + extrinsic (red open circles) contributions to pyroelectricity as a function of strain. d) Independently plotted magnitude and sign of the extrinsic contribution to pyroelectricity as a function of strain. e) Normalized pyroelectric coefficient as a function of temperature for the various heterostructures at 1 kHz and 0V DC bias.

a characteristic penetration depth into an underlying material ($\lambda = \sqrt{\frac{2D}{\omega}}$) can be defined where D and ω refer to the thermal diffusivity and radial frequency of the material and applied temperature amplitude, respectively. This inversely, frequency-dependent depth defines the distance before the magnitude of an initial applied temperature amplitude has significantly (>60%) decayed. As a result, through the frequency-dependent investigation of the pyroelectric response (Figure 4.10a), signatures of secondary contribution suppression become evident. Namely, all heterostructures display a decreasing pyroelectric coefficient as higher heating frequencies are obtained. This phenomenon can be explained *via* the reduction of the thermal penetration depth into the substrate. At low frequencies, a finite volume of the substrate, and thus thin films are able to thermally expand, producing a finite secondary contribution. However, with reduced heating of the substrate at higher frequencies, the reduction of thermal expansion mechanically restricts the clamped thin-film heterostructure, thus suppressing piezoelectric-based secondary contributions. With attention to frequencies above 1.4 kHz, a change of slope to a saturated regime suggests the secondary effects at lower frequencies are no longer active. As such, all further measurements depicted in this work were characterized above 1.4 kHz to ensure any secondary contributions could be minimized. Furthermore, an additional dielectric contribution (π_ε) must also be considered under applied electric fields (E) ($\pi_\varepsilon = \varepsilon_0 E \frac{\partial \varepsilon_r(E)}{\partial T}$), where ε_0 and ε_r refer to the permittivity of free space and relative permittivity, respectively. As depicted in Figure 4.10b, pyroelectric coefficient loops, similar to piezoelectric-strain based "butterfly" loops, display two oppositely poled polarization directions, mediated by a V_c in each polarity direction where π approaches 0. In addition to the trend of decreasing zero-field π at increasing tensile strains seen previously in the frequency-dependent measurements, another feature at non-zero fields becomes apparent. Specifically, the slope of the pyroelectric response as larger DC electric fields are reached provides validation of the presence of increasing temperature-induced dielectric contributions to pyroelectricity. Due to the inherently competing signs of $\pi_\varepsilon \sim \frac{\partial \varepsilon_r}{\partial T} > 0$ and $\pi_{total} \sim \frac{\partial P}{\partial T} < 0$, the enhanced dielectric response of the in-plane oriented heterostructures manifests as a larger decrease in total pyroelectric response at higher applied fields.

Furthermore, with secondary and dielectric contributions suppressed at 1 kHz and 0V applied bias, respectively, attention was next turned to characterizing the pure intrinsic response to pyroelectricity. In this study, the inclusion of a purely monodomain, *c*-oriented heterostructure allows for the investigation of a system without temperature-dependent domain wall contributions, *i.e.* extrinsic effects. As such, from the zero-field remanent polarization of the monodomain heterostructure on $TbScO_3$ ($P_{r,-1.26\%}$), the intrinsic contribution for any given average biaxial strain ε_m may be calculated as follows if sufficient distance (>400 K) from the nonlinear response of the Curie Phase transition is maintained.

$$\pi_{int,\varepsilon_m} = \pi_{int,-1.26\%} \frac{P_{r,\varepsilon_m}}{P_{r,-1.26\%}} \quad \text{(Eq. 4.5)}$$

By referencing pyroelectric response to a zero-extrinsic contribution reference heterostructure, with all remaining contributions held constant (*i.e.* secondary and dielectric

contributions), the extrinsic response to pyroelectricity can be extracted. Within Figure 4.10c, the calculated intrinsic response is plotted across strain states (black, dotted). Similarly, the total remaining pyroelectric contributions of intrinsic + extrinsic (red, open circles) depict the deviation from the purely monodomain reference heterostructure. When the extrinsic contribution is plotted independently (Figure 4.10d), both the magnitude and sign may finally be extracted. Here we notice two key findings. First, the sign of the extrinsic contribution within the compressive strain regimes (>0) works against the total pyroelectric response while the sign within the tensile strain regimes (<0) work towards enhancing the total pyroelectric response. This feature is consistent with the findings of phenomenological models and temperature-dependent scanning probe methods (Figure 4.8) where-in compressively-strained domain configurations convert to increased out-of-plane domain densities at higher temperatures ($\frac{\partial P}{\partial T} > 0$) and tensile-strained domain configurations convert to decreased out-of-plane domain densities ($\frac{\partial P}{\partial T} < 0$). Finally, the magnitude of these extrinsic effects, specifically the mixed phase, in-plane orientated domain structures, may account up to 35% of the total pyroelectric response, allowing for an undeveloped route of thin-film pyroelectric response enhancement.

To further probe this unprecedented, mixed-phase extrinsic response, the temperature dependence of the normalized total pyroelectric coefficient was investigated (Figure 4.10e). With the exception of the two mixed phase heterostructures ($SmScO_3$ and $PrScO_3$), the compressively strained pyroelectric response displays a relatively linear trend as *c*/*a* fractions convert to pure *c*-domain configurations and pre-existing *c*-domain regions increase in polarization magnitude as the Curie transition temperature is approached. Contrarily, the response of the mixed phase heterostructures show a more pronounced increase of pyroelectric response and may be attributed to the significant domain reconfiguration and phase competition between *c*/*a* and a_1/a_2. Due to the negative extrinsic contribution, this effect initially adds to the intrinsic response, promoting the increased steepness at elevated temperatures. Nonetheless, after the interconversion to a primarily in-plane oriented domain configuration, the total pyroelectric response is seen to sharply decay.

From this work, it has become evident that extrinsic effects to pyroelectricity can no longer be neglected and may play a significant role in tuning the overall pyroelectric response in thin-film ferroelectrics. Through the application of compressive strain from underlying substrates, $PbZr_{0.2}Ti_{0.8}O_3$ heterostructures maintain a positive (>0) extrinsic contribution that works against the negative intrinsic response as *c* and *c*/*a* domain structures convert to purely *c*-domain configurations. In the exact opposite fashion, tensile-strained heterostructures promote the conversion of mixed-phase *c*/*a* and a_1/a_2 to purely in-plane orientated configurations that further increase the intrinsic response. Strain-engineering offers the pyroelectric community a new route of introducing phase-instabilities that promote enhanced pyroelectric response without the limitations and challenges of high temperature operation near Curie phase transitions. Finally, this newly developed high-frequency, AC phase-sensitive methodology systematically allows for the suppression and deconvolution of various contributions to pyroelectricity which have remained relatively elusive to date.

Chapter 5
Comprehensive Quantification of Pyroelectric Contributions

In this Chapter, I introduce a comprehensive characterization technique used to independently quantify the *intrinsic*, *extrinsic*, *secondary,* and *dielectric* contributions to the measured pyroelectric response. With application of high-frequency heating and high DC electric fields, the often coupled contributions to the total pyroelectric response can be systematically and independently characterized to unveil both magnitude and sign (*i.e.,* <0 or >0).

5.1 Introduction

While considerable advances in controlling both dielectric (E) and piezoelectric (X) responses have been made, there are limited developments over the past few decades in the understanding of routes to enhance π. Although there are a number of commercial applications for pyroelectrics (*e.g.*, infrared sensors for thermal imaging, pollutant detection, *etc*.[3-4]), these typically rely on materials such as $LiTaO_3$, $LiNbO_3$, and triglycine sulfate which have rather unremarkable room-temperature π values, but other features (*e.g.*, low dielectric permittivity) that make them useful for some applications. In turn, the development of new materials with large π or routes to enhance π in existing materials has led to reports of enhanced electrothermal responses, generally accomplished by placing the material in proximity to a temperature-induced phase boundary [5]. While this provides for impressive values of π, the effects are enhanced only in a narrow temperature regime (*e.g.*, near the ferroelectric-to-paraelectric phase boundary occurring at the Curie temperature, T_C). Nonetheless, there is considerably less work on the same phenomena in proximity to chemically-induced phase boundaries. While it is well known that both dielectric and piezoelectric response can be enhanced in the vicinity of features like the morphotropic phase boundary (MPB) [6-9], few, and often conflicting, reports have addressed the evolution of pyroelectric responses at such features [10-13]. In this Chapter, I identify the magnitude and sign of the *intrinsic*, *extrinsic*, *dielectric*, and *secondary* pyroelectric contributions to the total pyroelectric response as a function of chemistry in thin-films of the canonical ferroelectric $PbZr_{1-x}Ti_xO_3$ (x = 0.40, 0.48, 0.60, and 0.80) across the morphotropic phase boundary. Using phase-sensitive frequency and applied DC-bias methods, the various pyroelectric contributions were measured. It is found that the total pyroelectric response decreases systematically as one moves from higher to lower titanium contents. This arises from a combination of decreasing *intrinsic* response (-232 μC m^{-2} K^{-1} to -97 μC m^{-2} K^{-1}) and a sign inversion (33 μC m^{-2} K^{-1} to -17 μC m^{-2} K^{-1}) of the *extrinsic* contribution upon crossing the morphotropic phase boundary. Additionally, the measured *secondary* and *dielectric* contributions span between -70 and -29 μC m^{-2} K^{-1} and 10-115 μC m^{-2} K^{-1} under applied fields, respectively, following closely trends in the piezoelectric and dielectric susceptibility. These findings and methodologies provide novel insights into the understudied realm of pyroelectric response enhancement.

5.2 Understanding the Various Contributions to Pyroelectricity

Among the various interrelationships of electrical, mechanical, and thermal properties of polar materials, electrothermal effects have remained relatively understudied as a result of limited materials physics understanding, insufficient access to well-controlled materials, and inadequate measurement protocols [1]. Therefore, future work must address the lack of in-depth understanding of the various contributions to pyroelectric response, how and why π varies in magnitude and sign with material chemistry, strain, *etc*. and, in turn, what can be done outside tuning T_C to produce large pyroelectric effects near room temperature. Such a discussion requires that one understands the potential contributions to pyroelectric response. In general, one may express the total pyroelectric response as:

$$\pi = \pi_{Int} + \pi_{Ext} + \pi_{Sec} + \pi_{\varepsilon} + \pi_{Ter}$$
$$= \phi\left(\frac{\partial P_s}{\partial T}\right)_x + P_s\left(\frac{\partial \phi}{\partial T}\right)_x + \left(\frac{\partial P_s}{\partial X}\right)_T \left(\frac{\partial X}{\partial x}\right)_T \left(\frac{\partial x}{\partial T}\right)_X + \varepsilon_0 E\left(\frac{\partial \varepsilon_r(E)}{\partial T}\right)$$
$$+ \pi_{Ter} \quad \text{(Eq. 5.1)}$$

where ϕ is the fraction of ferroelectric domains contributing to the pyroelectric response, x is the strain, ε_0 is the permittivity of free space, and ε_r is the relative permittivity. Here, the *primary* contribution is defined by the combination of both the *intrinsic* (π_{Int}, first term) and *extrinsic* (π_{Ext}, second term) effects, similar to that of dielectrics [14-16]. The *intrinsic* contribution arises from the temperature dependence of P_s (*i.e.*, within the ferroelectric domains), while the *extrinsic* contribution arises from the temperature dependence of the domain structure (*i.e.*, thermally-induced domain-wall motion) [14]. The *secondary* contribution (π_{Sec}, third term), in general, arises from the fact that all pyroelectric materials are also piezoelectric. Thus, temperature-induced volume changes are commensurate with piezoelectric polarization changes. Furthermore, complications arise in thin-film geometries where the thermal-expansion mismatch between the film and substrate provides additional induced stress by confining the free in-plane thermal expansion of the film, and thus can induce additional changes in P_s *via* the piezoelectric effect. To encompass all these coupled subtleties, the *secondary* contribution includes material properties such as the piezoelectric coefficient, elastic stiffness, and the thermal-expansion coefficient [14,17,18]. Furthermore, under applied electric fields, a *dielectric* contribution (π_{ε}, fourth term) arises from the temperature and electric-field dependence of ε_r. Lastly, the *tertiary* contribution (π_{Ter}, fifth term) arises via the piezoelectric effect from inhomogeneous heating that induces nonuniform stresses [19]. This effect typically only pertains to bulk materials and may be neglected if uniform heating is achieved; which is typically the case in thin films. To date, outside of a limited number of phenomenological-modeling treatments [14,15,20] and indirect-property measurements [21], there have been few attempts to directly extract these various contributions to electrothermal response [22,23].

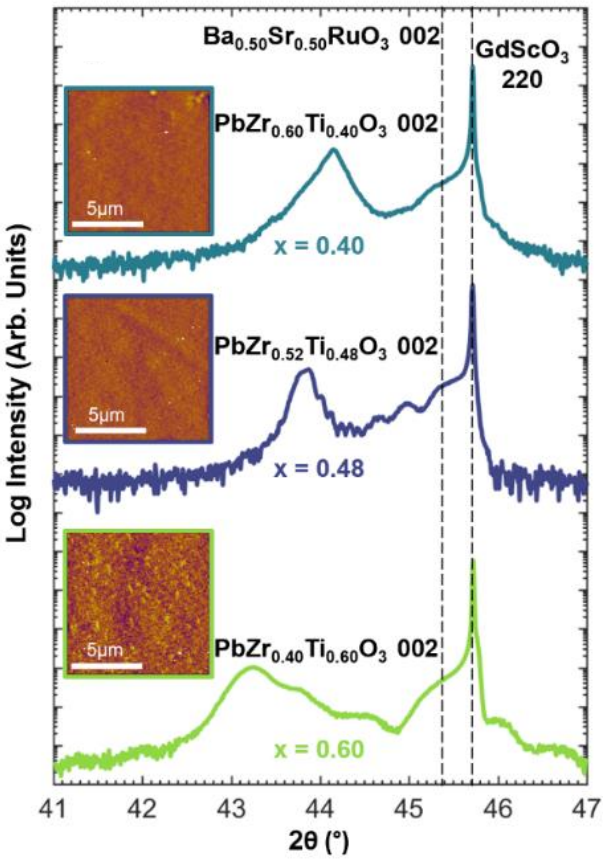

Figure 5.1: Structural measurements of $PbZr_{1-x}Ti_xO_3$ heterostructures. (a) X-Ray diffraction line scans of x = 0.40, 0.48, and 0.60 heterostructures (bottom to top) about the $GdScO_3$ 220-diffraction condition. Insets display the respective atomic force microscopy surface morphology.

5.3 $PbZr_{1-x}Ti_xO_3$ Synthesis and Device Integration

In order to systematically investigate the various pyroelectric contributions as one transitions across the MPB, a composition series of 100-140-nm-thick $PbZr_{0.60}Ti_{0.40}O_3$, $PbZr_{0.52}Ti_{0.48}O_3$, $PbZr_{0.40}Ti_{0.60}O_3$, and $PbZr_{0.2}Ti_{0.8}O_3$ thin films (henceforth referred to as x = 0.40, 0.48, 0.60, and 0.80 heterostructures, respectively), were grown on 20 nm $Ba_{0.50}Sr_{0.50}RuO_3/GdScO_3$ (110) single-crystal substrates via pulsed-laser deposition [24]. It is also noted that the 120-nm-thick x = 0.80 heterostructures were used in prior studies and are included here for additional comparison and to validate the overall measurements and direct extraction methodologies developed herein [25]. θ-2θ X-ray diffraction and atomic force microscopy studies (Figure 5.1) confirm that, in all cases, the heterostructures are epitaxial and of high surface topography quality (root mean square roughness < 600 pm). Additionally, due to deposited thickness and the relatively large lattice mismatch (1-3%) between the films and the underlying substrates, all heterostructures were found to be single-phase and grown in a relaxed-strain state from reciprocal space mapping studies (Figure 5.2a-e). Preliminary X-ray diffraction, dielectric, and ferroelectric studies for the x = 0.80 heterostructures are reported elsewhere [25]. In total, I have a systematic set of $PbZr_{1-x}Ti_xO_3$ films varying only in chemistry that can be used to probe the evolution of pyroelectric response.

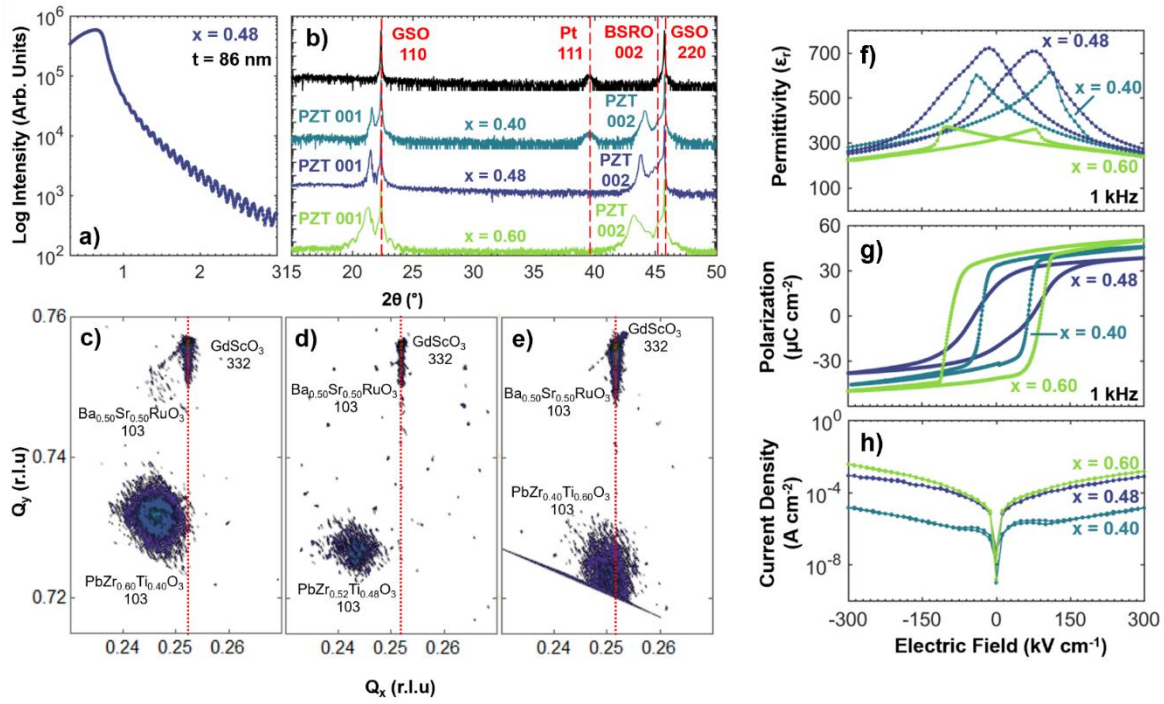

Figure 5.2: (a) Representative X-Ray reflectivity results for x = 0.48 heterostructures. Indicated thickness (t) used for growth rate characterization. (b) Wide angle $\theta - 2\theta$ line scans for as-grown x = 0.60 and x = 0.48, and post-device processed x = 0.40. An expected Pt (111) peak is found due to Pt deposited electrodes and heaters, see single layer $Pt/GdScO_3$ in black for reference. Reciprocal space mapping studies about the off-axis 332-diffraction condition of (c) x = 0.40, (d) x = 0.48, and (e) x = 0.60 heterostructures. The red dashed lines indicate coherently strained in-plane lattice parameter peak positions. (f) Measured dielectric permittivity response under applied dc-electric fields at 1 kHz. (g) Room temperature ferroelectric hysteresis response for the various compositions measured at 1 kHz. (h) Current-voltage response for the various compositions measured on 6.2E-5 cm^2 device areas.

Following the preliminary structural studies, electrothermal devices were fabricated [22,25] and were then used to probe the evolution of dielectric, ferroelectric, and pyroelectric properties. First, the dielectric permittivity as a function of background DC bias (for brevity shown at 1 kHz), further confirms the quality of the heterostructures and begins to provide insight into the variations in material response (Figure 5.2f). The dielectric permittivity is expected, and is measured, to be the largest in heterostructures with MPB chemistry (x = 0.48) and then to drop off, first to the x = 0.40 heterostructures (with rhombohedral structure) and then to the x = 0.60 heterostructures (with tetragonal structure) [6]. Likewise, as expected, the x = 0.48 heterostructures also showed the largest dielectric tunability (~69%). Additionally, polarization-electric-field hysteresis loops (again, for brevity, reported at 1 kHz) were measured and, as expected, the largest P_s value was observed for the x = 0.60 heterostructures, while the x = 0.48 heterostructures exhibited the lowest (Figure 5.2g). The insulating properties of these thin films were further confirmed via studies of current density with applied DC voltage (*i.e.*, leakage studies), where symmetric response with low-leakage currents (< 10^{-2} A cm^{-2}), that improve with increasing zirconium content, were observed (Figure 5.2h). In all, the $PbZr_{1-x}Ti_xO_3$ composition series exhibits the crystal structure and dielectric and ferroelectric properties desired and which are consistent with previous reports [26].

5.4 Extraction of Secondary Contributions to Pyroelectricity

Armed with this set of high-quality heterostructures, I proceeded to explore the evolution of the pyroelectric response. As previously defined, the *secondary* contribution to pyroelectricity in thin films arises from the elastic-boundary conditions of the substrate that confines the in-plane thermal expansion of the film, and thus induces a stress that drives a piezoelectric response. With the thin (100 nm) platinum resistive heater geometry used in this work, a characteristic thermal-penetration depth (λ) into the $GdScO_3$ substrate may be expressed as

$$\lambda = \sqrt{\frac{D}{2\omega}} \qquad \text{(Eq. 5.2)}$$

where D and ω refer to the thermal diffusivity ($m^2\,s^{-1}$) and heating current oscillation angular frequency (rad s^{-1}), respectively [27]. By adjusting the angular frequency of the input heating current $I_{1\omega}$ to the resistive line, I was able to control the λ between approximately 5-150 μm (Figure 5.3a). In turn, by investigating the frequency response of λ, it is possible to identify two regimes of response. At low frequencies (<10 Hz), ~30% of the total substrate thickness (500 μm) is effectively being heated, allowing for local thermal expansion of the substrate, and thus a *secondary* contribution from thermal expansion mismatch with the heated film. At high frequencies (>1 kHz), however, λ becomes comparable to the half-heater width (5 μm), and only ~1% of the substrate thickness is heated. This small, heated fraction of the total substrate thickness is clamped by the surrounding ~99% of unheated substrate and thus has negligible thermal expansion. Within this regime, both the in-plane thermal expansion of the semi-infinite substrate and, in turn, *secondar*y contribution in the system are effectively

suppressed [28]. By limiting λ to a negligible fraction of the substrate, I have identified a route to obtain negligible *secondary* contributions (inset, Figure 5.3a).

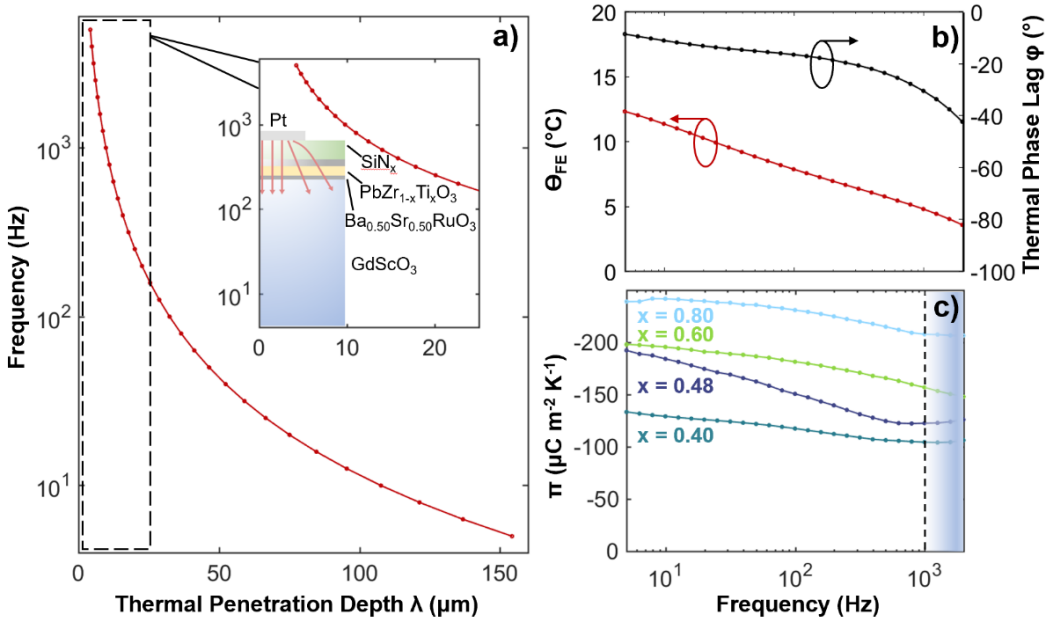

Figure 5.3: Thermal and *secondary* measurements of $PbZr_{1-x}Ti_xO_3$ thin-films. (a) Calculated thermal penetration depth into the $GdScO_3$ substrate used to define the cut-off frequency for secondary contributions. Inset displays a schematic of the heat flux through the thin-film stack where the heater half width is approached at 1 kHz. (b) Temperature oscillation amplitude (left axis) and associated thermal phase lag (right axis) within the ferroelectric film as a function of heating frequency 1ω. (c) Frequency dependence of the π displaying a suppressed *secondary* effect past ~1 kHz.

To quantitatively estimate the frequency cut-off regime for the *secondary* contribution, the peak-to-peak sinusoidal temperature oscillation amplitude of the ferroelectric θ_{FE} ($°C_{pk\text{-}pk}$) and the thermal-phase lag to the input heating current $I_{1\omega}$ were characterized (Figure 5.3b) [22]. From this, the total π could be calculated as a function of heating input frequency (Figure 5.3c). As the frequency of the measurement is increased, π decreases and begins to flatten out at ~1 kHz, indicative of a suppression of the *secondary* contribution [28]. There are two important observations to be made from this data. First, as the titanium content (x) decreases, so does the overall π (from -242 μC m^{-2} K^{-1} to -129 μC m^{-2} K^{-1} at 10 Hz for x = 0.8 and 0.4 heterostructures, respectively). Second, this trend remains even when the *secondary* contribution is suppressed at high frequency. Subtracting the total π at 1 kHz from that at 10 Hz to extract the effective *secondary* contribution in this frequency range, a reduction of magnitude 29, 70, 41, and 34 μC m^{-2} K^{-1} for the x = 0.40, 0.48, 0.60, and 0.80 heterostructures can be seen, respectively. Additionally, I note that this effective *secondary* contribution is specific only to this frequency regime (*i.e.*, it could be, slightly, larger in some cases) since full saturation of π at low frequencies is limited by the noise floor of the collected pyroelectric current (i_p). The greatest *secondary* contributions are found closer to the MPB, consistent with the expected enhanced effective piezoelectric coefficient d^*_{jkl} in those materials. Due to the systematic use of $GdScO_3$ substrates (*i.e.*, an equivalent elastic-boundary condition across all heterostructure compositions), differences in *secondary*

response may be primarily attributed to varying piezoelectric responses. In total, it is possible to identify frequency regimes where *secondary* effects may be effectively suppressed, thus providing experimental boundaries for the following electrothermal measurements.

5.5 Extraction of Dielectric Contributions to Pyroelectricity

Having effectively shown that one can suppress (and therefore quantify) the *secondary* contribution, my attention shifted to understanding the *dielectric* contribution to pyroelectricity. To separate out this effect, we recall that the *dielectric* contribution is defined as $\varepsilon_0 E \left(\frac{\partial \varepsilon_r(E)}{\partial T}\right)$ and requires knowledge of both the field- *and* temperature-dependence of ε_r (Figure 5.4a). To obtain this information, I measured the capacitance as a function of field (E = 0-500 kV cm^{-1}) at three temperatures (*i.e.*, 23°C, 33°C, and 42°C) (Figure 5.4b) and extracted the derivative of the curve in the temperature regime of interest (Figure 5.4c). Such data for the x = 0.40, 0.48, 0.60, and 0.80 heterostructures reveals that all compositions experience a reduction of permittivity with increasing bias which is explained via the suppression of the extrinsic domain-wall contributions at high fields (Figure 5.4b) [23]. Within a temperature regime similar to that applied for the pyroelectric studies (ΔT = 19°C), the largest dispersion in permittivity is found at lower fields (for brevity, representative data for the x = 0.48 heterostructures is provided; inset, Figure 5.4b). In turn, I can extract values of $\frac{\partial \varepsilon_r(E)}{\partial T}$ for the various heterostructures as a function of DC bias (Figure 5.4c) to be used to quantify the *dielectric* contribution to pyroelectricity. Due to enhanced dielectric susceptibility, the x = 0.48 heterostructures are found to have the highest *dielectric* contribution to pyroelectricity, followed first by the x = 0.40, and then the x = 0.60 and 0.80 heterostructures – following the trend in overall dielectric permittivity. Additionally, all *dielectric* contributions begin to asymptotically approach 0 K^{-1} past ~300 kV cm^{-1}. Thus, by taking the derivative $\frac{\partial \varepsilon_r(E)}{\partial T}$ at each given applied DC field, and multiplying by $\varepsilon_0 E$, the total *dielectric* contribution may

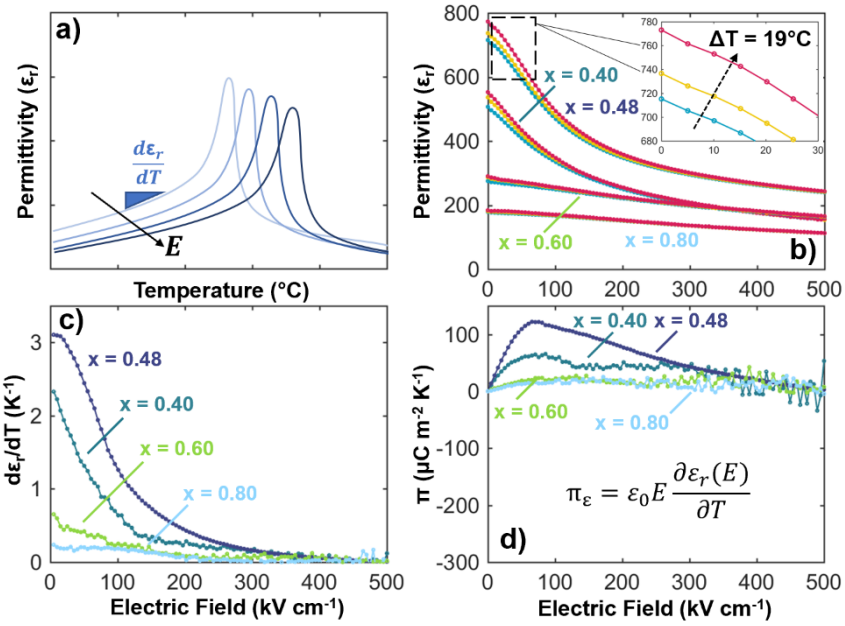

Figure 5.4: Extraction of the dielectric contribution to π. (a) Prototypical temperature dependence of the dielectric permittivity under applied dc-electric (E) fields. (b) Summary of the temperature dependent (23°C, 33°C, and 42°C) ε_r results as a function of applied dc-electric field for all heterostructures (Inset displays magnified results at low fields for x = 0.48). (c) Extracted temperature derivative of ε_r as a function of applied dc bias for the various heterostructures. (d) Calculated *dielectric* contributions as a function of field (*i.e.*, $\pi_\varepsilon = \varepsilon_0 E \frac{\partial \varepsilon_r(E)}{\partial T}$) for all heterostructures; note all start at zero applied field.

be extracted as a function of field (Figure 5.4d). As such, the *dielectric* contribution begins at 0 μC m^{-2} K^{-1} when there is no applied electric field [since $(\varepsilon_0 E \frac{\partial \varepsilon_r(E)}{\partial T})$] and rises at intermediate fields, and finally decrease towards zero at higher fields as $\frac{\partial \varepsilon_r(E)}{\partial T}$ is suppressed. Thus, by simply obtaining the temperature dependence of the dielectric permittivity under various applied DC biases, one can quantify (and subtract) this *dielectric* contribution (π_ε).

5.6 Extraction of Total Intrinsic Contributions to Pyroelectricity

Bringing this all together, I can complete DC-bias-dependent pyroelectric measurements in such a fashion that it allows us to account for the various remaining *total* and *intrinsic* contributions. First, the *secondary* contribution can be obtained by completing the measurements as a function of frequency and comparing the results at low (*i.e.*, ~10 Hz) and high (*i.e.*, ~1 kHz) frequency where the secondary contribution is quenched. Second, DC-bias dependence provides us the ability to quench the *extrinsic* contribution at high DC biases. Finally, the additional field- and temperature-dependence studies of ε_r noted above (Figure 5.4) allow us to quantify and decouple the *dielectric* contribution induced by the applied bias. The DC-bias evolution of i_p for the various heterostructures is provided, shown here scaled to the heater powers used for the x = 0.80 and 0.60 heterostructures to enable direct comparison (Figure 5.5a). All heterostructure variants display a characteristic i_p hysteresis loop, indicating two oppositely poled polarization states. In turn, the *total* π can then be extracted as a function of DC bias (note that π values are negative), and, again, a decrease in the maximum π is observed as the titanium content (x) is decreased (Figure 5.4b). Similar to previous reports [25,33], a butterfly-like response is observed, where the minima in pyroelectric response occur at the coercive field. Evidence of the *dielectric* contribution is observed in the positive slope of the *total* π as the magnitude of the applied electric field is increased. Due to the fact that $\frac{\partial \varepsilon_r(E)}{\partial T}$ remains intrinsically positive below T_C (Figure 5.4a), this contribution opposes the overall negative π values.

Furthermore, with the total response measured, attention was next directed towards extracting the *intrinsic* response. Similar to intrinsic contribution extraction methodologies in

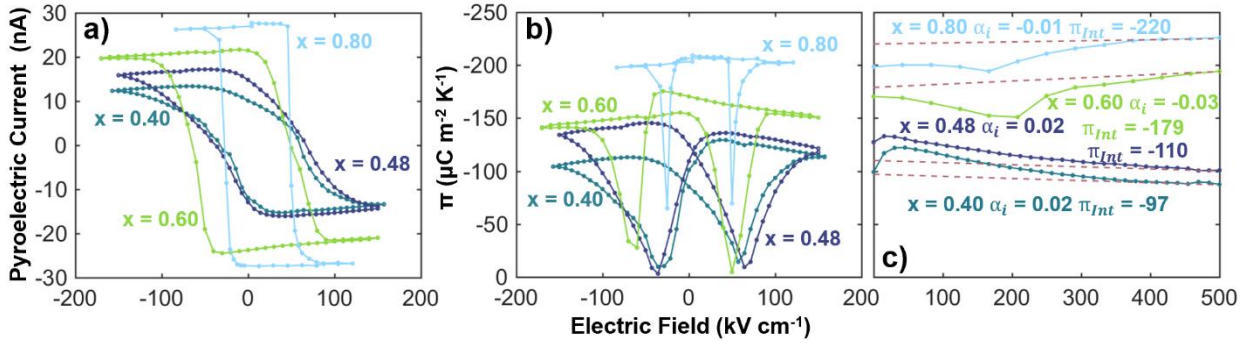

Figure 5.5: Pyroelectric and *intrinsic* DC field dependence of $PbZr_{1-x}Ti_xO_3$ heterostructures. (a) Applied DC-electric-field response of room temperature pyroelectric currents measured at 1 kHz and 10 mA rms heating current. Heating powers for x = 0.40 and 0.48 are scaled to the applied power used for the x = 0.60 and 0.80 heterostructures due to different heater-line resistances. (b) Pyroelectric coefficient results under applied DC bias for the various compositions measured at 1 kHz. (c) *Intrinsic* contribution extraction and DC-electric-field dependence from high-field π. Here, α_i and π_{int} refer to the slope and zero-field value of the field-dependent *intrinsic* contribution.

dielectrics [30,31], I utilized high-field π response to fit and extract the zero-field *intrinsic* contribution. Specifically, by extending the field-dependent pyroelectric response studies (Figure 5.5b) to higher DC-electric fields (500 kV cm^{-1}), the *dielectric* and *extrinsic* contributions can be effectively suppressed. Following the approach used in dielectric studies, I can then extrapolate back to zero bias to extract the zero-bias *intrinsic* response. Using the slope of π from the high-field regime (*i.e.*, 450-500 kV cm^{-1}), one can extrapolate the linear response to zero field for the various compositions (Figure 5.5c). All heterostructure variants exhibit a nearly field independent *intrinsic* response (slope α_i), similarly seen to the intrinsic contribution extraction for dielectric response [30,31]. Specifically, zero-field *intrinsic* values (π_{Int}) of -220, -179, -110, and -97 μC m^{-2} K^{-1} are extracted for the x = 0.80, 0.60, 0.48, and 0.40 heterostructures, respectively. Here, a decreasing contribution to the overall response with decreasing titanium composition (x) can be seen; consistent with previous phenomenological predictions [14].

5.7 Extraction of Extrinsic Contributions to Pyroelectricity

The *extrinsic* contribution has long eluded the pyroelectric community and refers to the temperature-dependent change in the domain structure whereby a change in temperature induces domain-wall motion as more temperature-stable domain structures grow at the expense of less stable structures [15]. Similar to the contribution domain structure plays in piezoelectric and dielectric susceptibilities [29], *extrinsic* effects can comprise a large percentage (>35%) of the total pyroelectric response [25], and thus are an essential contribution to understand and control. In the study of dielectric response, there are various approaches that have been demonstrated to separate out *extrinsic* effects. One, for example, aims to suppress domain-wall motion, and thus *extrinsic* contributions, *via* low-temperature measurements. Prior work [29] focused on low temperature (~5 K) AC electric-field studies to elucidate the contributions and suppression of *extrinsic* effects where domain-wall motion is no longer thermally activated. Another approach aims to suppress domain-wall motion via high applied DC-electric fields. Prior work on $PbZr_{1-x}Ti_xO_3$ thin films identified DC-field regimes >200 kV cm^{-1} wherein domain walls become electrically "pinned," thus suppressing *extrinsic* contributions and diminishing the overall dielectric response [30-31]. To date, no equivalent methodologies have been developed for pyroelectric response.

As such, I initially explored analogous approaches. First, focusing on low-temperature studies, a clear suppression of the total i_p response was found as expected; however, extraction of π *via* Eq. 4 (Chapter 2) remained challenging due to the reduced temperature dependence of the platinum-heater-line resistance and associated DC temperature rises at temperatures <20 K (*i.e.*, where domain-wall motion is suppressed). In turn, the applied AC-temperature oscillations and material DC temperature could not be accurately characterized and easily controlled in the thin-film 3ω method applied herein [27,32]. Based on this observation, I turned to high-DC-bias techniques to attempt to suppress domain-wall contributions. From a naïve point of view, simply completing pyroelectric studies as a function of dc bias should provide a way to quench (at high biases) the *extrinsic* contributions. While this is true, it is also convoluted with any potential *dielectric* contributions that arise from applied bias. To begin to explain the total composition dependence of π, a detailed methodology of contribution extraction is demonstrated, as an example, on the x = 0.80

heterostructures which were previously characterized using a monodomain (*i.e.*, zero *extrinsic* contribution) reference sample [25]. Namely, using the measured *total* (Figure 6.5b), *intrinsic* (Figure 5.5c), *dielectric* (Figure 5.4d), and *secondary* (Figure 5.3c) contributions, the *extrinsic* contribution can be solved for in a self-consistent fashion according to Eq. 5.1. Again, the *secondary* contribution can be quenched by operating at high frequencies (1 kHz) thus allowing direct quantification of this value. The *intrinsic* contribution can then be extracted from the zero-field intercept of a line with the slope of the high-field *total* pyroelectric response (similar to approaches used in dielectrics [30]). The measured *dielectric* response is extracted from *C-V* methodologies and is zero at zero field. Likewise, the *extrinsic* contribution should approach 0 μC m^{-2} K^{-1} at high fields as domain-wall motion is quenched. Armed with this evolution, one can self-consistently solve for the *extrinsic* contribution to the *total* response. Specifically, using the full-range (*i.e.*, 0-500 kV cm^{-1}) DC-bias dependence of the *total* π , I can identify where the *extrinsic* response asymptotes to 0 μC m^{-2} K^{-1} such that it fulfills the conditions above. For the x = 0.80 heterostructures, the *extrinsic* response is found to approach zero near 300 kV cm^{-1} (Figure 5.6a). Again, to quantify the *extrinsic* contribution from Eq. 5.1, response is extracted at 1 kHz and zero field, where *secondary* and *dielectric* contributions can be excluded. Compared to recent work [25], the *intrinsic* (~250 μC m^{-2} K^{-1}) and *extrinsic* (~40 μC m^{-2} K^{-1}) values align quite closely at E = 0 kV cm^{-1}; thus confirming the validity of this methodology. Due to the AC nature of the pyroelectric measurements, DC-leakage currents induced by applied DC biases do not contribute to the collected i_p. The major advantage of this proposed methodology is that it allows researchers to extract *extrinsic* contributions without the need for free-standing geometries, intricate knowledge of piezoelectric/thermal properties, and/or

monodomain-reference samples (something that may not be possible to achieve for all ferroelectric systems) [25,34-36].

Applying the same methodology to the other compositions (Figure 5.6b-d), a comprehensive comparison of all π contributions may be made (Figure 5.6e). Here, both the *total* and *intrinsic* contributions display decreasing values as the titanium content (x) is decreased. This trend may be explained, in part, via the intrinsic polarization axis moving away from the out-of-plane [001] for the titanium-rich, tetragonal phases towards the [111] cube diagonal for the titanium-poor, rhombohedral phases, thus contributing less to the out-of-plane *total* measured response. Furthermore, the *secondary* contribution not only depends on the thermal-expansion mismatch between the film and substrate, but additionally on the piezoelectric coefficient d^*_{jkl} of the film. Due to the use of $GdScO_3$ substrates across all compositions, the systematic increase and maximum of the *secondary* in proximity to the MPB is thus attributed to the enhanced piezoelectric susceptibility since the thermal

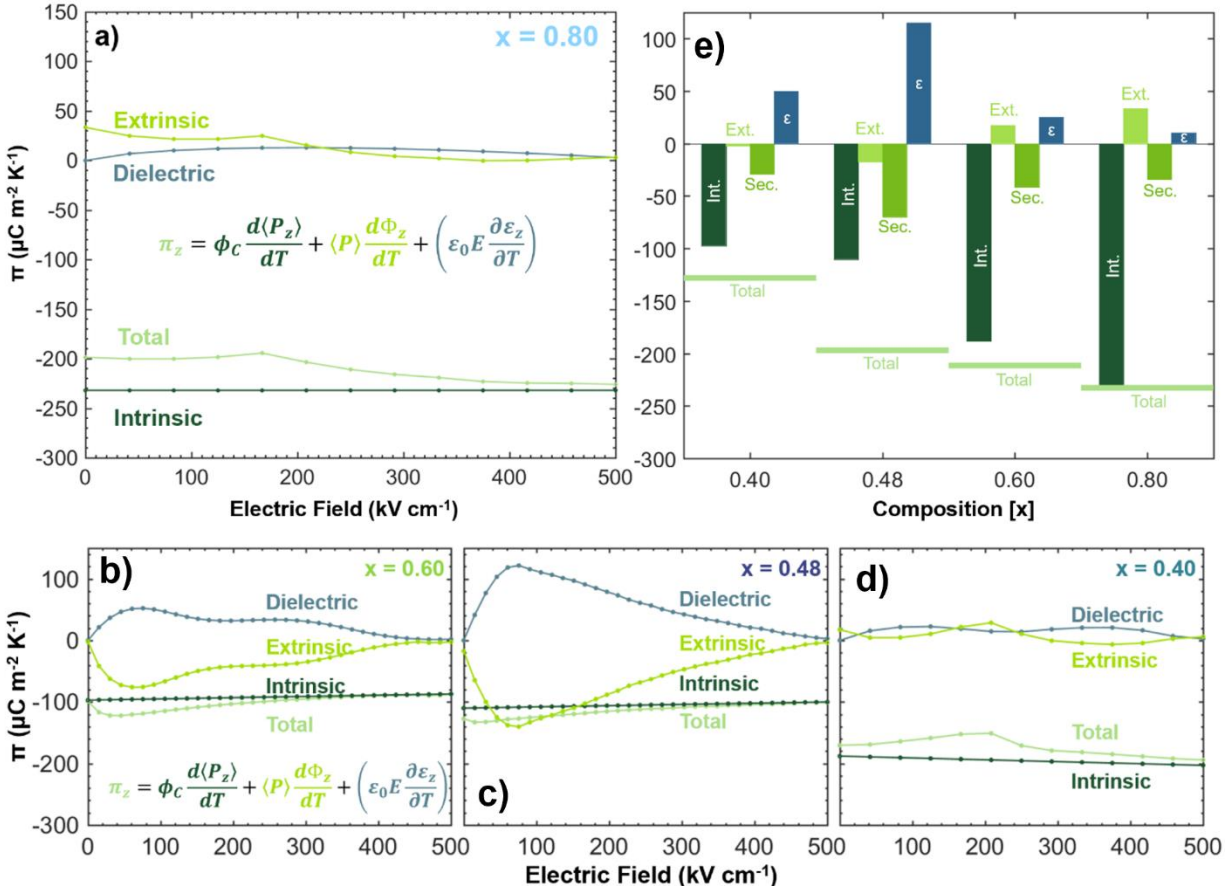

Figure 5.6: Extraction of the various contributions to π for $PbZr_{1-x}Ti_xO_3$ heterostructures. (a) DC-field dependence of the total π and extracted *extrinsic*, *dielectric*, and *intrinsic* π contributions for x = 0.80 heterostructures. Summarized DC-electric field response of the *intrinsic, dielectric, extrinsic,* and *total* π for (b) x = 0.60, (c) x = 0.48, and (d) x = 0.60 heterostructures. Previously calculated *dielectric* contributions (Figure 5.4d) have been smoothed to reduce noise from measured permittivity results. (e) Summary of the *intrinsic*, *extrinsic*, *secondary*, and total π response as a function of composition across the various $PbZr_{1-x}Ti_xO_3$ chemistries studied herein. Due to the opposing signs of the various contributions, the total net π value is indicated via a solid line for each composition. The *dielectric* contribution displayed here is that measured at an applied dc-electric field of 100 kV cm^{-1}.

expansion mismatch is not expected to vary greatly [14,37,38] Following previous phenomenological models [14], the *extrinsic* contribution does decrease as one approaches the MPB from the titanium-rich side and actually undergoes a sign inversion upon proceeding to the zirconium-rich side of the phase diagram and is explained by changes in how the domain structures respond to temperature changes in this regime. Unlike the case for $BaTiO_3$ and titanium-rich $PbZr_{1-x}Ti_xO_3$ where abundant strain-dependent phase diagrams provide insight into the thermodynamic stability of domain phases [39,40], there has been less attention on the zirconium-rich side of the phase diagram. Titanium-rich compositions are known to exhibit an increase in *c*-domain fraction upon heating at compressive strains (*i.e.*, 0 > *extrinsic*) [39], however, this appears to be the opposite for these relaxed zirconium-rich heterostructures. Due to the curvature of the monoclinic phase towards the zirconium-rich compositions and the polar axis remaining in the plane between the [001] and [111], compositions at or near the monoclinic phase of $PbZr_{1-x}Ti_xO_3$ would be expected to have a decrease in out-of-plane polarized domains as the rhombohedral phase is approached [41-43]. Therefore, the $\left(\frac{\partial \phi}{\partial T}\right)$ term would in fact be negative as decreased out-of-plane polarizations are stabilized upon heating, thus directly supporting the total negative pyroelectric response. Naively speaking, one would predict that an enhanced negative *extrinsic* contribution would drive an overall higher magnitude π response, however, with our ability to quantify the *intrinsic* and other contributions, it is clear this is not always the case. For titanium-rich compositions, large dominating *intrinsic* values work against *extrinsic* contributions that are of the opposite sign. Upon crossing the MPB, even though the sign of the *extrinsic* contribution changes to work together with the *intrinsic* response, this coincides with a strong reduction in the *intrinsic* response arising from a symmetry change in the material. The result is a diminished overall response. In order to maximize the total pyroelectric response in the $PbZr_{1-x}Ti_xO_3$ system, a minimally strained (< -0.25%) tetragonal thin film of composition x = 0.80 could be developed to minimize the counteracting positive *extrinsic* response, while maintaining enhanced *intrinsic* contributions relative to the cases where diminished *intrinsic* response follows *extrinsic* sign inversions. The key to pyroelectric susceptibility enhancement lies in the ability to control *intrinsic and extrinsic* contributions via composition and elastic boundary conditions, respectively.

5.8 Conclusions

In total, frequency and DC-bias methodologies have been applied to systematically investigate and directly extract numerous pyroelectric contributions as a function of chemistry across the MPB of the $PbZr_{1-x}Ti_xO_3$ system. Unlike dielectric and piezoelectric susceptibilities which are found to become maximum at the MPB, the pyroelectric response displays a systematic reduction as the titanium content (x) is decreased. This reduction is explained primarily via the reduction of the *intrinsic* pyroelectric contribution, in which the out-of-plane polar axis component is reduced upon transitioning from the tetragonal to the rhombohedral side of the phase diagram. Additionally, an inversion of the sign of the *extrinsic* contribution was found to lie in the vicinity of the MPB in which the temperature dependence of the out-of-plane pointing domain fractions decreases upon heating. In all, the *intrinsic* response accounted for upwards of 99% (|97-232| μC m^{-2} K^{-1}) of the total measured

pyroelectric response, while the *extrinsic* and *secondary* contributions account for ~8% (|2-33| μC m^{-2} K^{-1}) and ~23% (|29-70| μC m^{-2} K^{-1}), respectively. Additionally, following trends in the dielectric susceptibility, the measured *dielectric* contribution ranged from |10-115| μC m^{-2} K^{-1} at an applied electric field of 100 kV cm^{-1} for the respective compositions. This work has not only provided the community with a comprehensive pyroelectric extraction methodology, but elucidated the need to directly characterize and consider all pyroelectric contributions of ferroelectric systems for the thoughtful design of enhanced susceptibility within pyroelectric materials.

Chapter 6
In-plane and Substrate-Released Pyroelectricity in Thin-Film Ferroelectrics

In this Chapter, I study the in-plane pyroelectric response of tetragonal ferroelectric $PbTiO_3$ *via* applied mechanical strain imposed by various underlying substrates. I demonstrate the necessary characterization test platforms and in-plane, applied electric field direction dependence of the dielectric, ferroelectric, and pyroelectric response. Additionally, I introduce the capability of further investigating secondary contributions to thin-film pyroelectric response through substrate-film release processes that minimize mechanical elastic boundary conditions which often degrade pyroelectric response.

6.1 In-Plane Pyroelectricity

Up to this point, the work of this Dissertation has focused solely on the out-of-plane pyroelectric response (π_z, normal to the substrate) in which temperature dependent changes of the out-of-plane polarization (P_z) is captured. Nevertheless, with accompanying anisotropy of crystal structures, π is defined as a first-rank tensor in which pyroelectric response in the two orthogonal in-plane orientations is present as well (*i.e.*, π_x and π_y). Unfortunately, due to the complex, and non-trivial nature of in-plane electrical and thermal characterization, a whole realm of in-plane pyroelectric physics has yet to be explored. For example, as compared to the secondary contribution to π_z response which maintains indirect mechanical coupling (*i.e.*, Poisson's ratio) [1] to the underlying substrate, π_x would be expected to maintain increased susceptibility to substrate clamping due to the direct coupling of the epitaxial thin-film interface. These secondary contribution differences would also manifest as further boundary conditions for the extrinsic domain-wall and dielectric contributions where domain-wall motion and perturbation may be induced *via* in-plane electric fields. Lastly, due to the differences in length scales of out-of-plane thin-film systems (nm) and in-plane test platforms used today (μm) [2], tertiary contributions to pyroelectricity may also need to be considered if homogenous heating cannot be maintained [3].

As previously discussed, a facile route utilized by the community to enhance pyroelectric response is to take advantage of phase competition and polarization instabilities which often accompany such features as the Curie phase transition [4]. To further develop additional routes for pyroelectric susceptibility enhancement and the findings of the extrinsic, mixed-phase pyroelectric response (Chapter 4), I propose the investigation of $(PbTiO_3)_n/(SrTiO_3)_n$ thin-film superlattice heterostructures which have recently been demonstrated to maintain increasingly high field- and temperature-dependent domain-phase competition between coexisting a_1/a_2 and polar-vortex structures (Figure 6.1) [5,6]. At the foundation of these competing, mixed-phase domain configurations is the complex interplay of Landau, gradient, elastic, and electric (electrostatic) energy terms. As a result, the phase competition in this superlattice system can be simultaneously and deterministically tuned *via* superlattice periodicity, applied DC bias, and temperature. Furthermore, one must understand that both the coexisting domain structures maintain only in-plane oriented polarization, thus requiring in-plane characterization methods. Due to the transition from the low-temperature polar vortex to the high-temperature a_1/a_2 phase, new phenomena such as positive pyroelectric coefficient magnitudes ($\pi > 0$), enhanced extrinsic, domain-wall contributions, and switching kinetics, among others, could be realized.

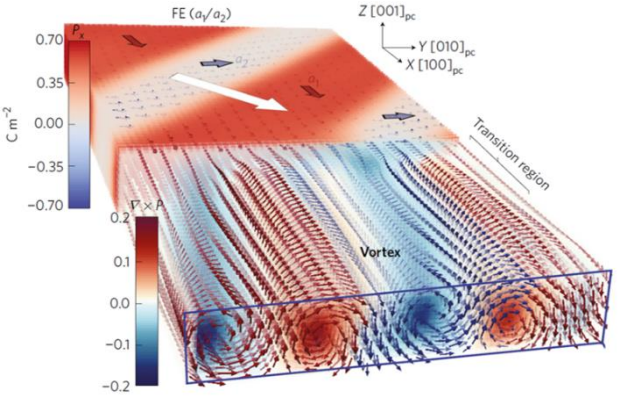

Figure 6.1: Phase-field model depicting the polarization direction and phase interconversion (*i.e.*, a_1/a_2 to polar vortex) region within $PbTiO_3/SrTiO_3$ superlattice [5].

To initially simplify the complex superlattice response and validate the necessary electrothermal in-plane test platforms required for pyroelectric characterization, I chose to first investigate the prototypical tetragonal $PbTiO_3$ system which maintains a rich and accessible set of in-plane oriented domain-configurations [7]. Namely, through epitaxial strain induced by underlying substrates, both compressive and tensile strain regimes can be applied to control *a*-domain density. As such, quantitative in-plane domain fractions from corresponding X-ray diffraction and scanning-probe metrologies could be used to validate the accuracy of the newly developed in-plane pyroelectric metrologies.

6.1.1 Domain Structure Characterization of Thin-Film $PbTiO_3$

To span the strain regime necessary for both pure *c* and *a* domain configurations, I synthesized 100 nm $PbTiO_3$ single-layer films with corresponding misfit strains (ε) upon $SrTiO_3$ 001 ($\varepsilon = -1.3\%$), $DyScO_3$ 110 ($\varepsilon = -0.2\%$), and $SmScO_3$ 110 ($\varepsilon = 0.7\%$) substrates *via* PLD. These substrates allow for both compressive and tensile strains necessary for tuning the *a* domain fraction [7]. Nonetheless, to confirm the domain configurations under the various strain states, I performed X-ray diffraction $2\theta - \omega$ line scans (Figure 6.2) where predominantly *c* domain structures of $SrTiO_3$-based monolayers evolved to *a* domain structures at higher tensile strains on $SmScO_3$ substrates. Specifically, there is a diffraction intensity redistribution from the corresponding *c* domain peak at 44° to the more pronounced *a*-domain diffraction peak near 46.5°. Additionally, evidence of residual *c*-domains remains present within the $SmScO_3$ heterostructure, suggesting strain relaxation and either a *c/a* or mixed-phase *c/a* + a_1/a_2 domain configuration. To probe the domain structure further, on-axis reciprocal space maps were additionally utilized to provide a more detailed structural analysis (Figure 6.3). Specifically, further investigation of the $DyScO_3$-based thin-films demonstrated the presence of both tilted *a* and *c* domains (inset Figure 6.3b). These associated tilts arise to minimize the mechanical elastic interfacial energy near the substrate due differing in-plane lattice constants of the *c* and *a* domains [8].

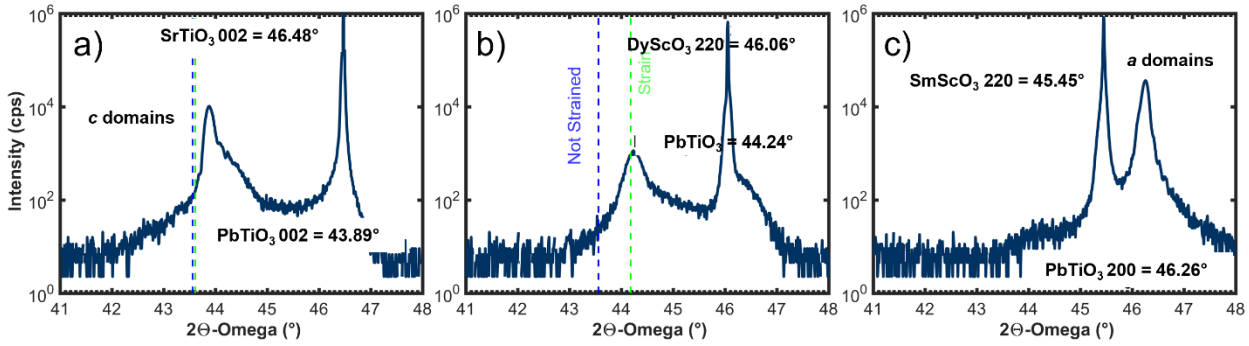

Figure 6.2: a,b,c) X-ray line scans about the $SrTiO_3$ 002, $DyScO_3$ 220, and $SmScO_3$ 220 diffraction condition, respectively. Insets indicate peak locations of the substrate and $PbTiO_3$ thin-film. Additionally, blue and green dashed vertical lines indicate the theoretical bulk and respective strained condition on each substrate.

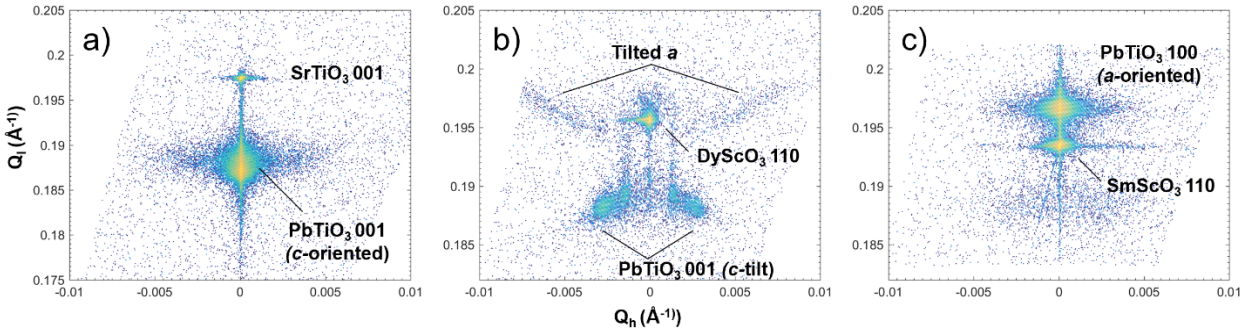

Figure 6.3: a,b,c) Reciprocal space maps about the $SrTiO_3$ 002, $DyScO_3$ 110, and $SmScO_3$ 110 diffraction condition, respectively. Insets indicate peak locations of the substrate and $PbTiO_3$ thin-film domain structures.

Furthermore, the domain architectures of these various thin films were directly imaged *via* piezoresponse force microscopy (PFM). As highlighted (Figure 6.4), a diverse set of vertical (Figure 6.4a-c) and lateral (Figure 6.4d-f) amplitude PFM images depict the complex domain configurations present. With the correctly applied PFM scan axis (left to right) relative to the various substrate orientations, the captured domain structures agree well with previous PFM work [7]. Specifically, both the $GdScO_3$- and $SmScO_3$-based heterostructures exhibit the traditional linear orthogonal features commonly indicative of *a* domains. However, when comparing the lateral and vertical PFM images of the $SmScO_3$-based system, regions of strong vertical response (*i.e.*, white "bead" regions separating striped regions) correspond to purely out-of-plane response (*c* domains), and thus confirm the findings from the X-ray diffraction studies. In all, with the use of X-ray diffraction and scanning-probe studies, the presence of various domain-structures induced *via* elastic strain of the underlying substrates were cross-validated and confirmed to agree with previous studies [7].

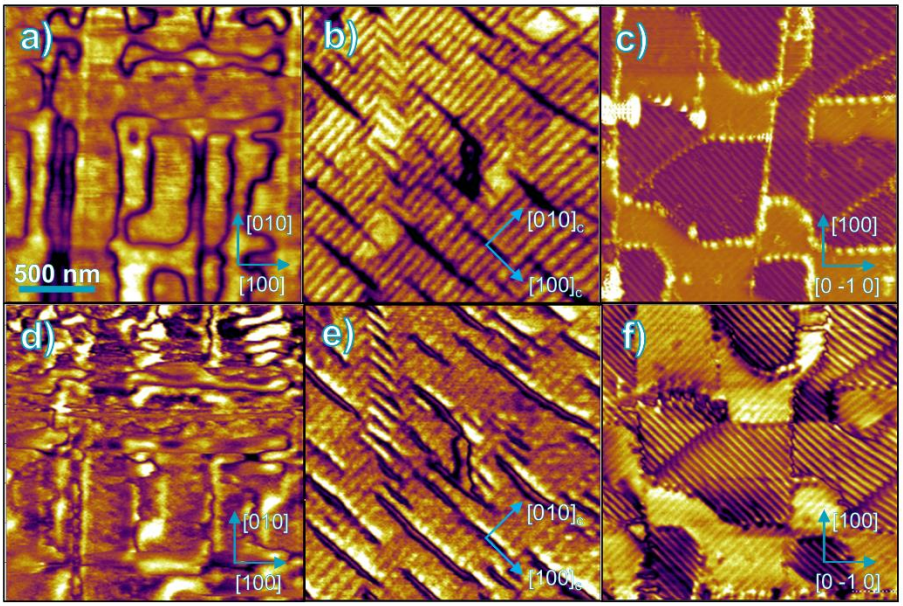

Figure 6.4: a, b, c) Vertical amplitude PFM response from 100-nm-thick $PbTiO_3$ thin-films grown on $SrTiO_3$, $DyScO_3$, and $SmScO_3$ substrates, respectively. d, e, f) Corresponding lateral amplitude PFM response of the $PbTiO_3$ thin-films grown on $SrTiO_3$, $DyScO_3$, and $SmScO_3$ substrates, respectively.

6.1.2 Fabrication of In-Plane Pyroelectric Electrothermal Test Platforms

When initially designing an in-plane pyroelectric electrothermal test platform, I turned to efforts of the dielectric community, where in-plane dielectric response is investigated using interdigitated electrode (IDE) test platforms capable of delivering DC and small signal AC in-plane electric fields. Here, rather than a standard tri-layer (electrode-dielectric-electrode) parallel plate capacitor geometry used for out-of-plane measurements, a single monolayer dielectric is directly deposited to an underlying substrate. Through standard photolithography and metal lift-off processes, a metallic top interdigitated electrode may then be deposited (Figure 6.5). With two global contact pads at the bottom of the IDE (Figure 6.5a), the surface electrodes may be alternatingly biased. In order to capture the in-plane dielectric response of thin-films (ε_f), work by Farnell *et al.* established analytical models using relaxation solutions of Laplace's equation where device geometries and substrate dielectric constants (ε_s) were incorporated to properly account for the electric field distribution lines [2].

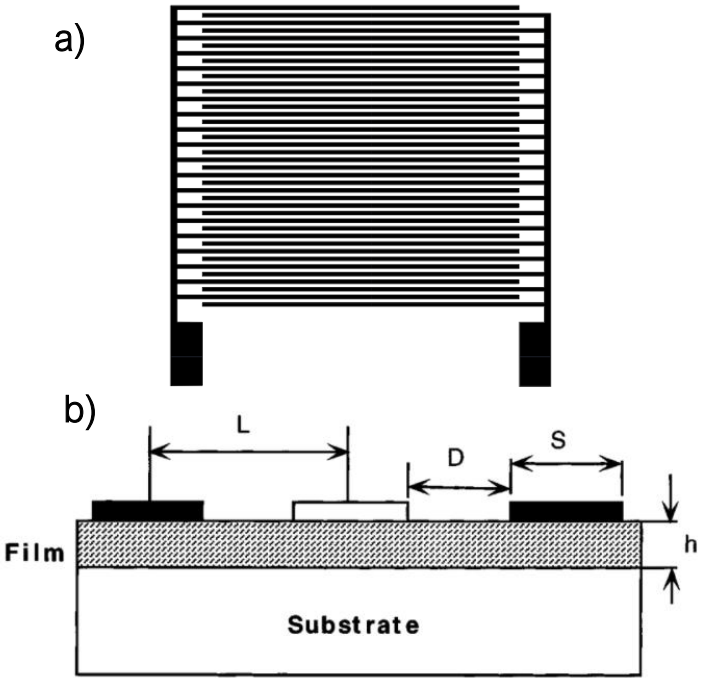

Figure 6.5: a) Top view and b) Cross-sectional view of a typical IDE structure. Here L, D, S, and h refer to center-to-center IDE finger spacing, finger-to-finger spacing, finger width, and film thickness, respectively [2].

$$\varepsilon_f = + \left\{ \frac{C - [K(1+\varepsilon_s)]}{K\left[1 - exp\left(\frac{-4.6h}{L}\right)\right]} \right\} \quad \text{(Eq. 6.1)}$$

Here, C refers to the measured capacitance per electrode section of width L per unit finger length where C_m, FL, and N are the measured capacitance (pF), IDE finger length (m), and half IDE pattern period (*i.e.*, $N = 2P - 1$ where P= No. of IDE finger pairs).

$$C = \frac{C_m}{FL * N} \quad \text{(Eq. 6.2)}$$

Furthermore, K is defined as geometrical factor that incorporates the IDE finger spacing and widths.

$$K = 6.5\left(\frac{D}{L}\right)^2 + 1.08\frac{D}{L} + 2.3 \quad \text{(Eq. 6.3)}$$

As such, I initially incorporated an IDE test structure within the currently used AC, phase-sensitive electrothermal test platform to maintain the ability to separate out, spurious, thermally stimulated currents which are not pyroelectric in nature. As a first step, I deposited a platinum IDE structure (with 40 fingers) on the thin-film ferroelectric with finger spacing (D),

finger widths (S), and finger lengths (FL) of 6 μm, 6 μm, and 500 μm, respectively. Following the IDE deposition, a blanket layer (180 nm) of SiN_x was deposited *via* PE-CVD to act as an electrical insulator from the thin-film resistive heater line, similarly to the standard π_z test platforms (Figure 6.6a). In turn, four-point, 3-Omega heater lines were then deposited before accessing electrical contact to the underlying IDE *via* reactive ion etch of the SiN_x layer (Figure 6.6b). Due to the electrode area scaling of the measured pyroelectric-current response, additional two- and three-line parallel heater line geometries were implemented to maximize pyroelectric-current signals. In all, in-plane AC electrical perturbations and DC electric fields could be applied to thin-film pyroelectrics during AC, periodic heating from top resistive heater lines (Figure. 6.6c).

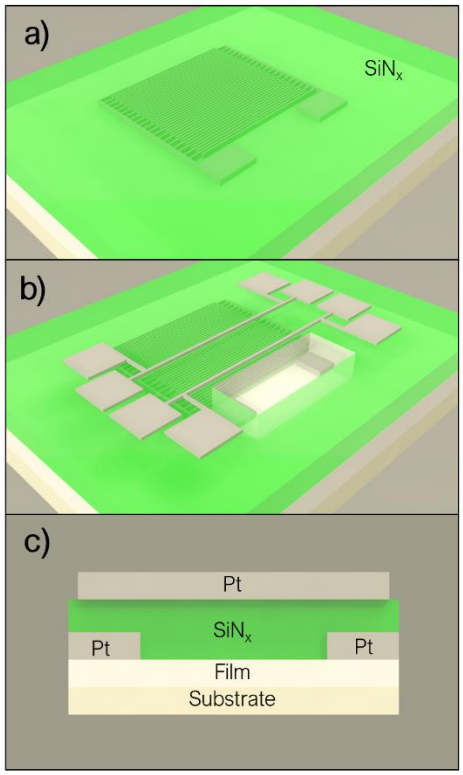

Figure 6.6: Iterative processing steps of the in-plane pyroelectric test platform depicting a) platinum IDE and SiN_x depositions, b) heater line development and IDE contact etch, c) and final cross-section view.

6.1.3 In-Plane Dielectric and Ferroelectric Response of $PbTiO_3$ Thin-Films

With $PbTiO_3$ thin films successfully incorporated within the newly developed electrothermal test platform, I first began the investigation of the dielectric susceptibility. For brevity, I will focus on the heterostructures that maintain in-plane oriented polarization (*i.e.,* $DyScO_3$ and $SmScO_3$ systems). To further capture the orientation dependence of the various in-plane susceptibilities, electrothermal IDE test platforms incorporated a total of 3 different finger orientations (*i.e.*, applied electric field orientations); all 45° relative to each other. Namely, with attention on the $DyScO_3$-based heterostructures, dielectric permittivity (left y-axis) and loss tangent (right y-axis) measurements utilizing the analytical IDE models of Farnell *et al.* exhibit an orientation dependence (Figure 6.7a-c). Insets here denote the relative orientation of the underlying substrate (black), the preferred *a* domain orientation (blue) and the applied electric field (E_{Field}) orientation (red). Due to the anisotropic in-plane lattice parameters of $DyScO_3$, *a* domains within *c*/*a* architectures preferentially align with the longer substrate axis (*i.e.*, $[100]_c$) to minimize elastic energy costs. Similar to out-of-plane dielectric response [9], in-plane domain orientations that lie perpendicular to the applied AC electric field perturbation promote enhanced response, as seen when comparing Figures 6.7a and b. Furthermore, the magnitude of the dielectric permittivity that maintains both parallel and perpendicular *a*-domain components relative to the applied field is seen to exhibit an intermediate valued response (Figure 6.7c). Turning attention now to the $SmScO_3$-based heterostructure, a slightly different trend is present. With *a* domain insets (blue) now referring to the net

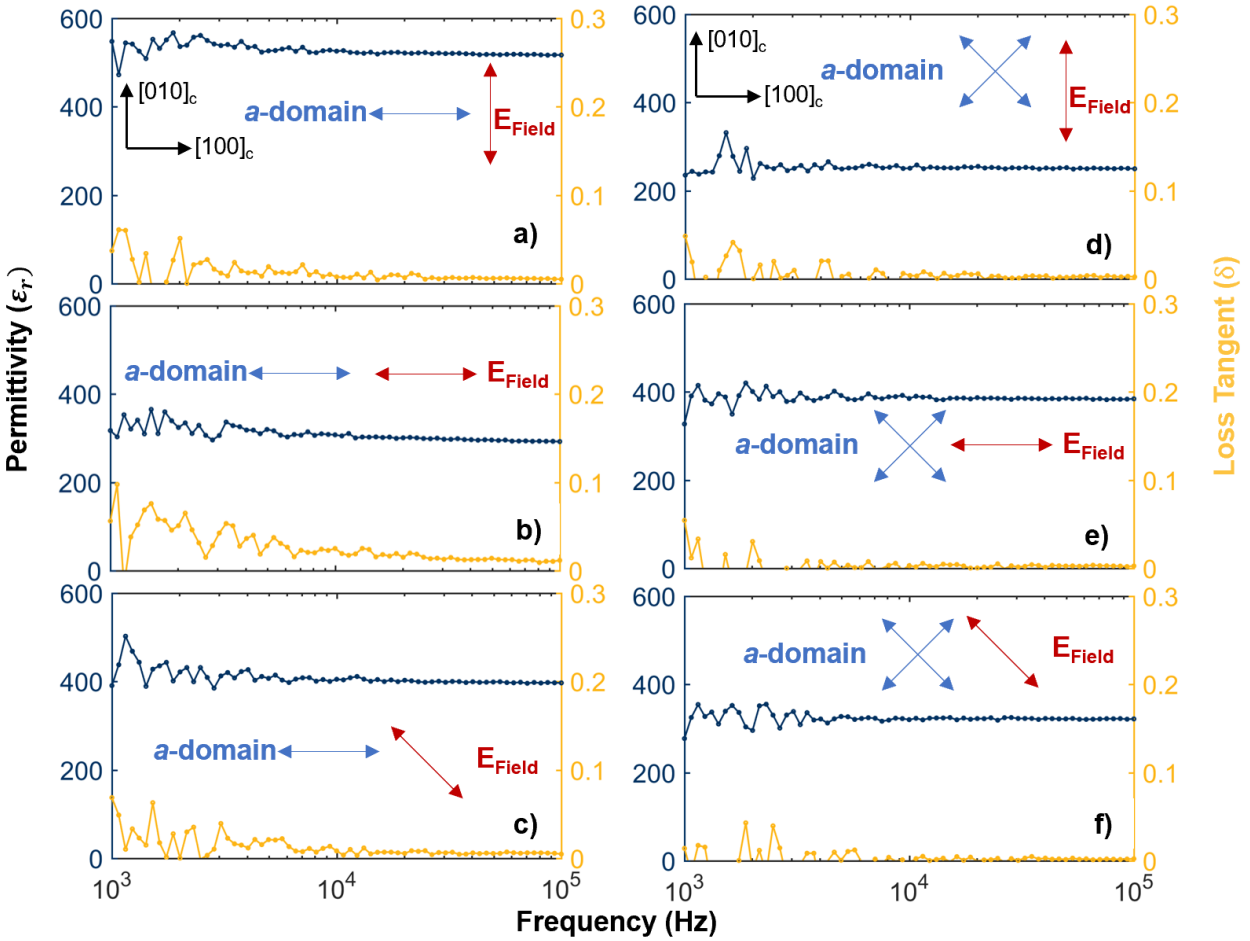

Figure 6.7: Frequency dependence of the dielectric permittivity (left y-axis) and loss tangent (right y-axis) at various applied electric field (E_{Field}) orientations relative to the in-plane polarization components of the thin-film upon a,b,c) $DyScO_3$ substrates and d,e,f) $SmScO_3$ substrates. Insets indicate the substrate orientation (black), *a*-domain orientation (blue), and applied electric field orientation (red). The polarization direction insets for the *a*-domains within the $SmScO_3$ systems indicate the net-polarization directions as a result of the a_1 and a_2 components.

polarization direction of the a_1 and a_2 components, one would expect, from an initial perspective, for perpendicularly applied electric fields (Figures 6.7c and d) to exhibit relatively similar dielectric response magnitudes, however, this is not the case. The current findings suggest that similarly to $DyScO_3$, the a_1 and a_2 domain fractions may not be equivalent, thus prompting the enhancement of one applied electric field orientation over the other. As result, applying the previously defined argument for the $DyScO_3$ structures, intermediate permittivity values would be expected for applied electric fields which capture response from both orthogonally applied fields (Figure 6.7e).

Nonetheless, focus was next turned toward investigating the ferroelectric switching of the in-plane oriented heterostructures. Once again, investigating the $DyScO_3$-based structures with *c*/*a*-domain configurations, a clear trend in measured polarization and PE loop broadening suggests that increasingly parallel-applied electric fields induce ferroelectric switching (Figure 6.8a-c). In the case where *a* domain orientation is minimally aligned to the electric field, standard linear dielectric response is exhibited. In contrast, $SmScO_3$ systems

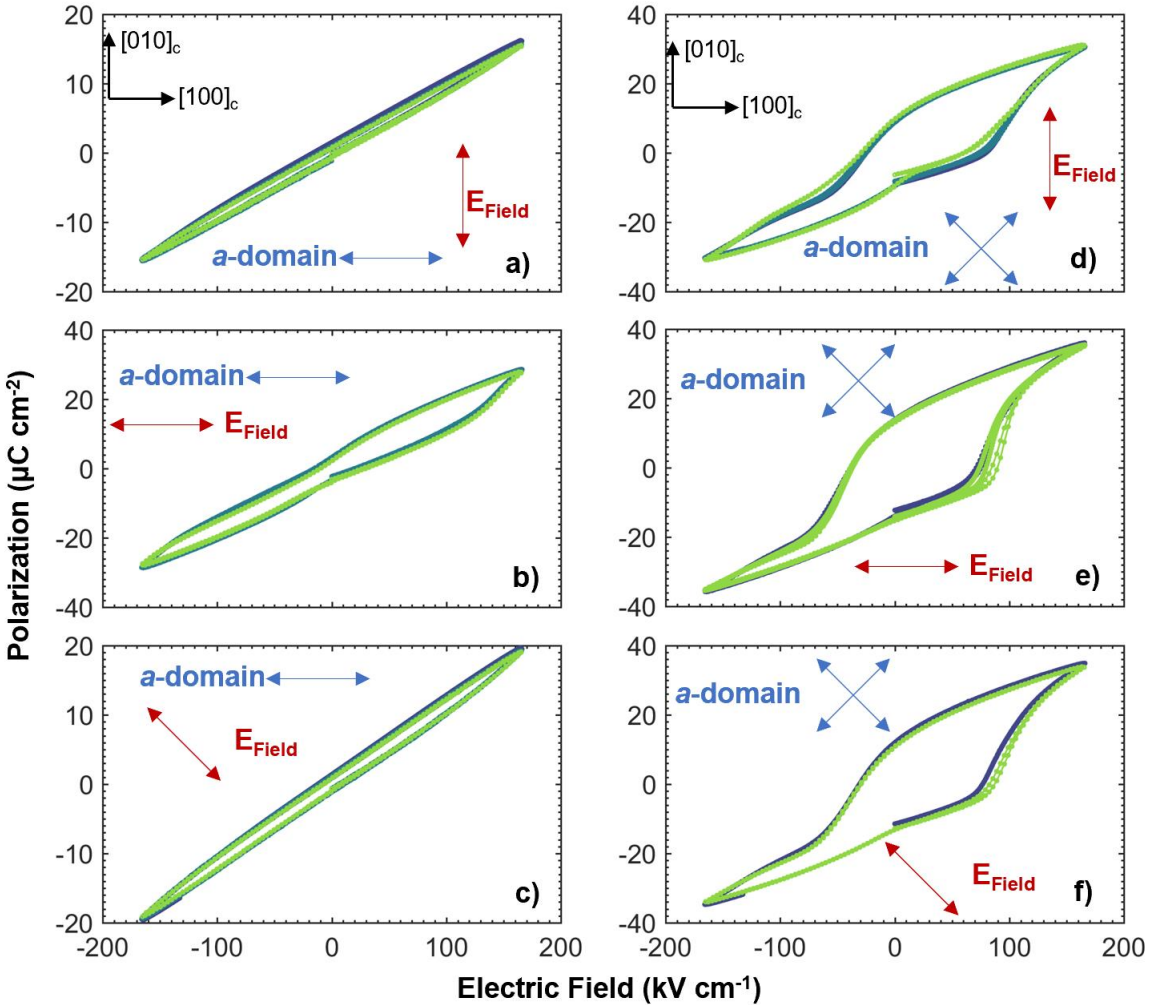

Figure 6.8: Polarization vs. electric field (PE) hysteresis loops at various applied electric field (E_{Field}) orientations relative to the in-plane polarization components of the thin-film upon a,b,c) $DyScO_3$ substrates and d,e,f) $SmScO_3$ substrates. Insets indicate the substrate orientation (black), *a*-domain orientation (blue), and applied electric field orientation (red). The polarization direction insets for the *a*-domains within the $SmScO_3$ systems indicate the net-polarization directions as a result of the a_1 and a_2 components. The overlaid PE loops indicate measurements completed at 1 kHz (turquoise), 5 kHz (purple) and 10 kHz (green).

maintained clear ferroelectric switching in all orientations, confirming the presence of a_1/a_2 domains in all four net polarization directions. It is also noted that a linear dielectric response may be superimposed with the measured PE loops arising from contributions to the underlying dielectric substrate. In summary, the PLD-synthesized 100-nm-thick $PbTiO_3$ thin films demonstrate a range of in-plane polar order, manifesting as differences in the measured ferroelectric and dielectric susceptibilities as a function of applied electric field orientations.

6.1.4 In-Plane Pyroelectric Response of $PbTiO_3$ Thin-Films

Moving forward from the characterization of in-plane dielectric and ferroelectric susceptibility, the $PbTiO_3$ electrothermal test platforms were next investigated for pyroelectric response. With use of (3) simultaneously heated resistive platinum thin-film lines to maximize the order-of-magnitudes reduced signals, the total current response and associated phase difference to the applied heating current was measured for the $DyScO_3$ heterostructures (Figure 6.9). The expected linear trends of total current and phase were not identified, but rather oscillating responses, indicating possible thermal and electrical cross talk during characterization. Unsurprisingly, if the lateral thermal penetration depth λ_x is calculated at the onset of the linear divergence of total pyroelectric current (~0.1-1 kHz), it is found that this distance approximately equates to the lateral spacing of the adjacent parallel resistive heater. Thus, to minimize thermal cross-talk of the test platform, reactive-ion etching was used to remove the blanket layer of electrically insulating SiN_x with use of the top heater lines as the effective positive photolithography mask. Comparing pre- and post-etch current response and utilizing only a single active heater line, the initial oscillating behavior could be corrected, leaving the as expected linear response without parasitic contributions from lateral heat dissipation (Figure 6.10). Nonetheless, to further separate out parasitic contributions to the measured pyroelectric response, electrical cross talk of adjacent IDE fingers was investigated. Namely, since lateral heat dissipation cannot be completely suppressed (even with SiN_x etching), adjacent IDE finger pairs also collect and contribute to the total

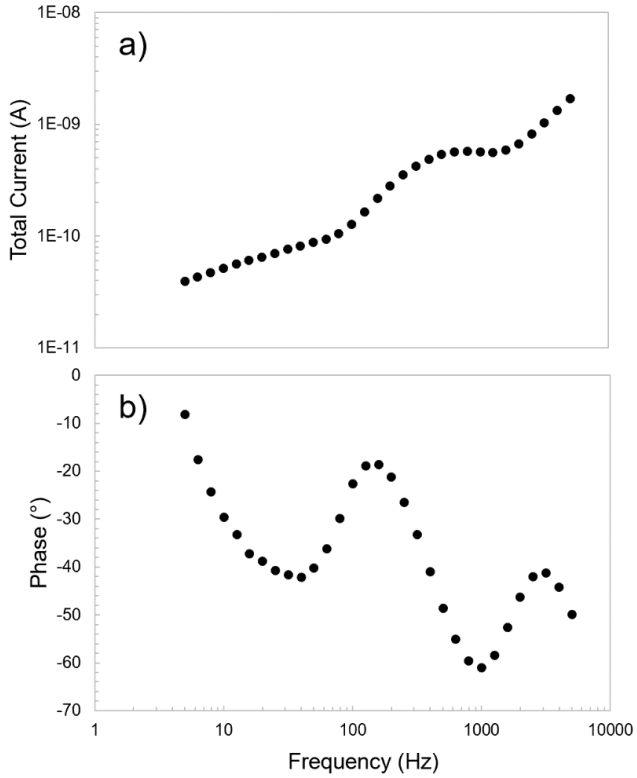

Figure 6.9: a) Total collected pyroelectric current as a function of input heating current frequency. b) Corresponding phase difference between measured pyroelectric current and input heating current signal on thin-film $PbTiO_3/DyScO_3$

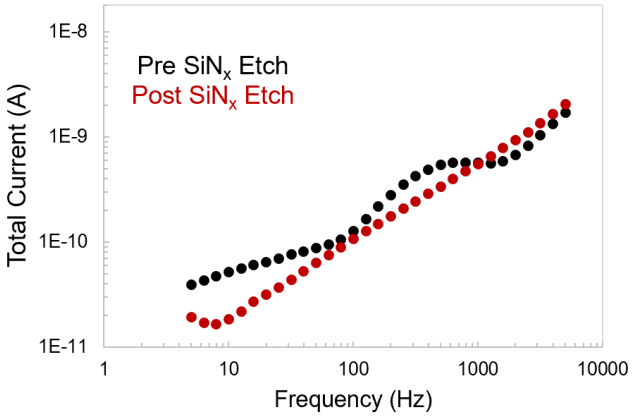

Figure 6.10: Total collected in-plane pyroelectric current using (3) simultaneously heated thin-film resistive heaters and intact SiN_x blanket layer (black). Corresponding post-etch pyroelectric response with use of single active heater line (red).

measured response, however, at an associated delayed phase lag. To further minimize these spurious effects, a single IDE pair can be used rather than the standard 40 finger pairs used for dielectric and ferroelectric characterization. Unfortunately, these necessary simplifications to the test platform come with additional consequences of reduced signal magnitudes. Despite these limitations, the in-plane pyroelectric response was still characterized, albeit using the most highly in-plane polarized heterostructure (*i.e.*, $PbTiO_3/SmScO_3$). Nonetheless, the total pyroelectric current, in-plane pyroelectric coefficient ($\pi_{[010]}$), and associated phase difference between measured response and applied heating current was successfully extracted (Figure 6.11). Beginning with the pyroelectric current response (Figure 6.11a), a few distinguishing features as compared to standard out-of-plane response of tetragonal ferroelectric systems becomes apparent. First, an asymmetry in the measured pyroelectric current manifests as a vertical hysteresis shift. This phenomenon may be attributed to possible a_1/a_2 orientation preference in which the full switching for a given direction is elastically and electrically limited by adjacent in-plane domains. To further support this claim, not only does $\pi_{[010]}$ exhibit enhanced response for a negative voltage polarity, but accompanying phase response demonstrates only a 116° difference between the two polarization states. In standard out-of-plane, AC phase sensitive pyroelectric characterization, this phase lag defines the difference between the incident heating current and resultant pyroelectric current. As a result, if full ferroelectric switching is obtained under DC bias, a phase difference of ~180° would be recorded. Furthermore, the near-zero remanent pyroelectric current (Figure 6.11a) after positive voltage poling indicates an unstable in-plane polarization orientation. Additionally, features such as the non-square and pinched current response may point to atypical, intermediate stable states which have previously been identified in a_1/a_2 domain configurations of $PbTiO_3$ [7]. Lastly, the mirror inversion of the pyroelectric current response about the zero-voltage axis, as compared to typical out-of-plane susceptibility, can also indicate a positive pyroelectric coefficient ($\pi_{[010]}>0$). However, more conclusive, and temperature-dependent studies of polarization would be required to confirm the sign inversion of the coefficient.

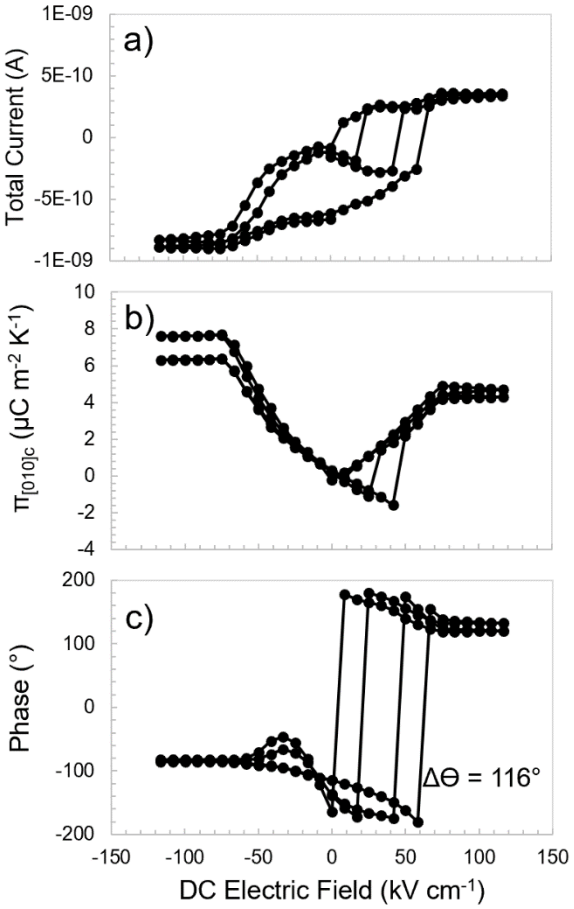

Figure 6.11: a) Total collected in-plane pyroelectric current as a function of applied DC electric field for 100-nm-thick $PbTiO_3/SmScO_3$ heterostructures. b) Extracted in-plane pyroelectric coefficient and c) associated phased difference between the input heating current and measured pyroelectric response.

To further validate the accuracy and learning of this new, in-plane electrothermal characterization method, changes to the current processes are required. First, as compared to the magnitude of purely out-of-plane *c* domain pyroelectric response ($\pi_z \approx 300\ \mu C\ m^{-2}K^{-1}$), the findings of this study indicate a rather modest magnitude ($\pi_{x,y} \approx 6\ \mu C\ m^{-2}K^{-1}$). Assuming no additional differences of secondary contributions (*i.e.*, substrate-induced, thermal lattice mismatch), the out-of-plane monodomain pyroelectric response should align closely to the in-plane a_1/a_2 magnitude. The reason for such a disparity in magnitudes may arise from insufficient modeling of the effective of electrode area. Namely, for the case of standard parallel-plate-capacitor geometries for out-of-plane pyroelectric characterization, the effective heater half-width (b_{eff}) used to translate the pyroelectric current to meaningful π_z values can be defined analytically. Here $\theta(x)$ refers to the temperature amplitude at a given distance x from the midpoint of the heater line. In the limiting case where the heater width is equal to the electrode width, b_{eff} simply becomes equivalent to the heater width.

$$b_{eff} = b_{heater} \frac{\int_0^{b_{electrode}} \theta(x)dx}{\int_0^{b_{heater}} \theta(x)dx} \quad \text{(Eq. 6.4)}$$

In the current design of the in-plane electrothermal test platform, solving for the effective heater width becomes non-trivial due to the fact that the IDE structure lies on top of the thin-film, and may also be collecting pyroelectric response (*i.e.*, dielectric contributions to pyroelectricity) form the underlying substrate which thus introduces increased errors of reported $\pi_{x,y}$. To circumvent these complications, purely in-plane IDE electrodes should be utilized where a clearly defined contact area to the IDE interface (*i.e.,* film thickness x IDE finger length) can be obtained. Using lessons from previous work on MgO hard-mask photolithography processes [10], I propose a new five-step, in-plane IDE process (Figure 6.12). After the blanket layer PLD-deposition of the $SrRuO_3$ bottom electrode (purple) upon a given substrate (white) is completed, a room temperature blanket layer of MgO dielectric (orange) will be deposited (Step 1). After patterning the desired IDE structure with photoresist (red), an H_3PO_4 wet-etch may be used to define the MgO-hard mask (Step 2). Following patterning, an additional $NaIO_4$ wet-etch defines the final $SrRuO_3$-based IDE device structure (Step 3). Furthermore, with exposed substrate between adjacent IDE fingers and top photoresist removed, the ferroelectric (green) thin film is deposited as a blanket layer (Step 4). Finally, the unprotected sidewalls of the MgO layer are wet etched again to deliver the final IDE device geometry (Step 5). Through this process flow, purely in-plane-interfaced electrodes are fabricated to ensure accurate electrode areas for $\pi_{x,y}$ calculations.

To test the viability of the proposed process flow, 100-nm-thick, $PbTiO_3/DyScO_3$ in-plane device structures were processed successfully with subsequent PE hysteresis and PFM response that align closely to previously reported measurements of this Dissertation. These

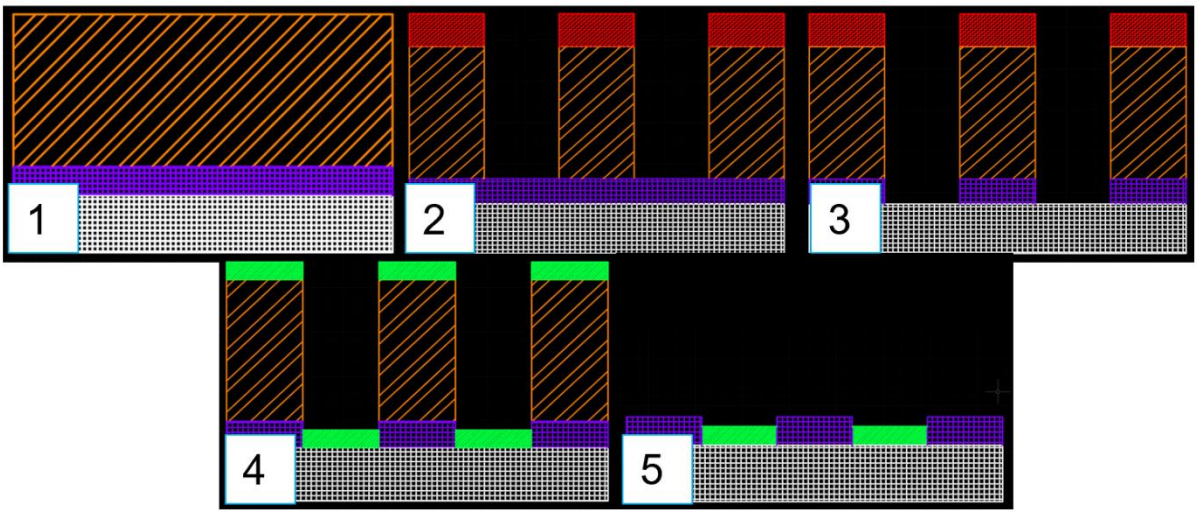

Figure 6.12: Five-step in-plane IDE fabrication process. Step 1) Blanket layer deposition of $SrRuO_3$ (purple) and MgO (orange). Step 2) Photolithography pattering with photoresist (red) to define the MgO hard mask *via* wet-etch. Step 3) Wet etch and definition of the underlying $SrRuO_3$ IDE. Step 4) Blanket layer deposition of the ferroelectric (green). Step 5) Final wet-etch of the MgO hard mask to define the IDE test structure.

preliminary findings suggest that high-quality ferroelectric $PbTiO_3$ can be deposited between MgO hard mask pillars and upon wet-etched surfaces of substrates while still maintaining the desired domain configuration (Figure 6.13). With the use of only single IDE finger pairs to minimize measurement cross talk, heater widths in excess of $2D$ (*i.e.*, twice the IDE finger pair distance) could be utilized to ensure homogenous in-plane heating, and thus reduction of possible tertiary contributions to pyroelectricity. In all, through the comprehensive investigation of in-plane dielectric and ferroelectric response as a function of varying domain architectures, a newly established in-plane pyroelectric metrology allows for the investigation of the relatively underdeveloped $\pi_{x,y}$ response. Additionally, by incorporating the previously established direct, AC phase-sensitive characterization technique, the ability to separate out spurious, thermally stimulated current to in-plane response is maintained. Despite the non-trivial nature of in-plane pyroelectric characterization, newly developed electrothermal test platforms have demonstrated the in-plane pyroelectric susceptibility of $PbTiO_3/SmScO_3$ heterostructures and may provide insights into the highly elastically-coupled switching kinetics of mechanically clamped in-plane ferroelastic domains.

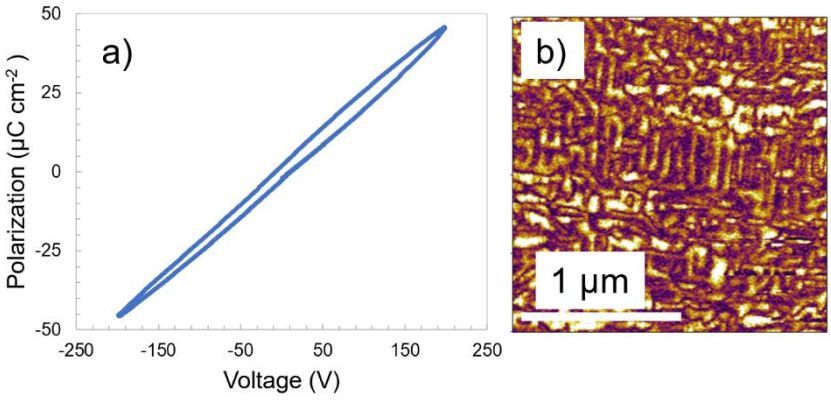

Figure 6.13: a) In-plane PE response of $PbTiO_3/DyScO_3$ device structures using purely in-plane contacted $SrRuO_3$ electrodes. b) Associated vertical amplitude PFM response of 100-nm-thick $PbTiO_3$ thin-film between two adjacent IDE finger pairs.

6.2 Pyroelectric Response in Si Under-Etched $BaTiO_3$ Thin Films

Following the efforts in elucidating novel extrinsic contributions *via* in-plane characterization, I next diverted attention towards further developments in the understanding of secondary contributions to pyroelectricity. Primarily defined as the thermal-mechanical interaction between the film and relatively thick, underlying substrate, secondary contributions and

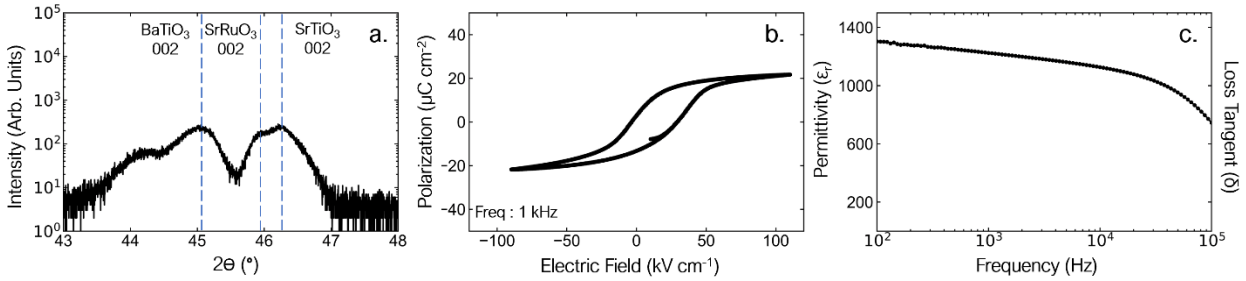

Figure 6.14: a) X-ray diffraction line scan of $BaTiO_3/SrRuO_3$ tri-layer heterostructures grown on 20 nm $SrTiO_3$-buffered Si (001) substrates. b) Polarization-electric field hysteresis loops taken at 1 kHz excitation frequency c) Dielectric permittivity (left axis) and respective loss tangent δ (right axis) under 5 mV AC sensing signal.

associated thermal stresses in thin-films have primarily been limited to only theoretical studies [11-13]. Only until recently have renewed interests and experimental achievements in the fabrication of "substrate-free" thin-films come to light where the clamping elastic boundary conditions induced by the substrate can be relaxed [14]. Subsequently motivated

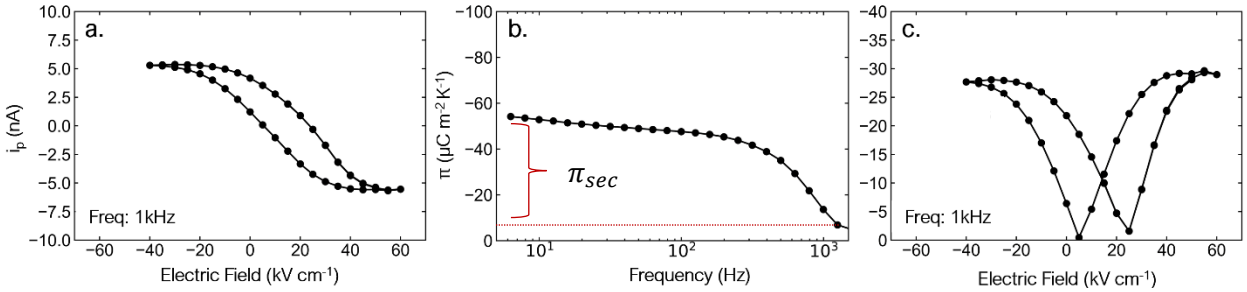

Figure 6.15: a) Pyroelectric current as a function of DC bias b) Frequency dependence of π between 5-1000 Hz applied AC heating current frequency and linearly extrapolated secondary pyroelectric contribution. c) DC bias response of π at 1 kHz AC heating current frequency.

to derive a more critical understanding of secondary pyroelectric contributions, I have developed a Si-based electrothermal test platform which would allow for isotropic etching to effectively relax the in-plane clamping to thin-film pyroelectrics. Although numerous reports have investigated pyroelectric response on Si substrates, results have been limited and convoluted by indirect characterization methods, bulk pyroelectric thicknesses (> 500 nm), elastically constrictive and thick (>1 μm) underlying membranes/buffer layers, limited operational frequencies, and increased processing complexity [15,18]. In order to address these shortcomings, I applied the direct, AC phase sensitive pyroelectric characterization techniques of this Dissertation to 70 nm $SrRuO_3$/ 100 nm $BaTiO_3$ / 20 nm $SrRuO_3$ heterostructures grown on 20-nm-thick $SrTiO_3$-buffered silicon substrates [19]. Due to the large thermal expansion mismatch between $BaTiO_3$ and silicon, this molecular beam epitaxy-

deposited $SrTiO_3$ buffer layer acts to reduce the mechanical stresses which promote polycrystalline, rather than epitaxial growth.

Utilizing the standard nanofabrication processes developed for the electrothermal test platform of this Dissertation (Chapter 3), preliminary structural and electrical properties were investigated (Figure 6.14). As compared to previous reports of thin-film $BaTiO_3$ response, these results align closely to a relatively non-strained $BaTiO_3$ heterostructure with predominantly *c/a* domain configurations [14]. Furthermore, the pyroelectric properties were next investigated as a function of applied electric fields and heating frequency (Figure 6.15). As depicted, the measured pyroelectric-current vs. electric field loops exhibit the expected (although slightly shifted along the field axis) response where the polarization orientation is reversibly switched. Furthermore, the frequency dependence of π demonstrates the prototypical negative slope of response and abrupt drop-off near the frequency regime associated with suppressed secondary contributions. Unlike the case for $PbZrTiO_3$-based systems deposited on single crystal scandate substrates (*e.g.,* $DyScO_3$, $SmScO_3$ etc.), Here the linear extrapolated response used to calculate the effective secondary pyroelectric contribution π_{sec} (*i.e.,* $\pi_{5Hz} - \pi_{1kHz}$) suggests secondary contributions account for almost 90% of the total measured response on Si-based substrates. Finally, the corresponding DC-field dependence of π exhibits the standard "butterfly" loop where minima correspond to the V_c.

In order to adapt the standard electrothermal test platform of this Dissertation, a silicon under-etch is required to partially release the active pyroelectric heterostructure beam (Figure 6.16). Using standard photolithography processes, two adjacent channels to the center pyroelectric beam were developed, exposing the silicon substrate surface (Figure 6.17a). Furthermore, the test platform was then exposed to 7 periodic XeF_2 dry-etch cycles (1 cycle = 32 sec.) to ensure that both lateral and vertical etching would take place (Figure 6.17b). Due to the underlying $SrTiO_3$ buffer layer beneath the pyroelectric active beam, a natural caping layer prevents XeF_2 interaction with the bottom $SrRuO_3$ electrode. To characterize the etch, a profilometer was used to trace the etch profile and confirmed an approximate vertical etch depth of 10 μm (Figure 6.17c). Due to the isotropic nature of XeF_2-Si etching, an accompanying 10 μm lateral etch depth would also be expected. Since the active pyroelectric beam width is on the order of 10 μm, this etch process would be sufficient to fully release the pyroelectric heterostructure. To further confirm the completion of the silicon under-etch, scanning electron microscopy images

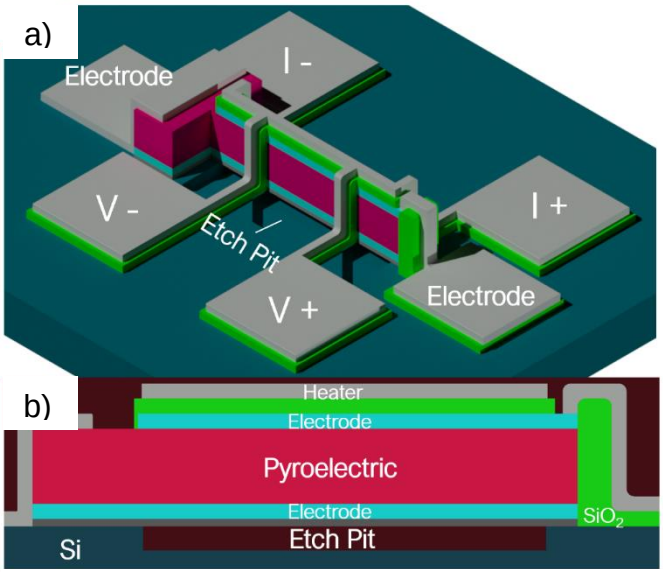

Figure 6.16: a) 3-dimensional schematic of the standard electrothermal test platform used in this study and integrated silicon-based etch pit to partially release the pyroelectric center beam. b) Corresponding cross sectional view of the heterostructure and under-etch silicon region.

were taken of the ferroelectric beam and confirmed that no residual underlying silicon was in contact with the heterostructure (Figure 6.17d). Although a comprehensive investigation of the post-etch pyroelectric response is required, complications arising due to insufficient photoresist protection of the ferroelectric during XeF_2 etch will need to be further addressed. Nonetheless, the thermal circuit was still investigated and confirms the presence of approximately a 2x increase in temperature oscillation amplitudes for under-etched devices (Figure 6.17e). This result can be understood *via* the reduced thermal contact, and thus heat dissipation to the semi-infinite thermally conducting silicon substrate. In all, the preliminary findings of the Si-based electrothermal test platforms confirm comparable crystal structure and ferroelectric/dielectric susceptibilities to lattice-matched substrates, enhanced secondary contributions, and diminished heat dissipation to the underlying substrates after release.

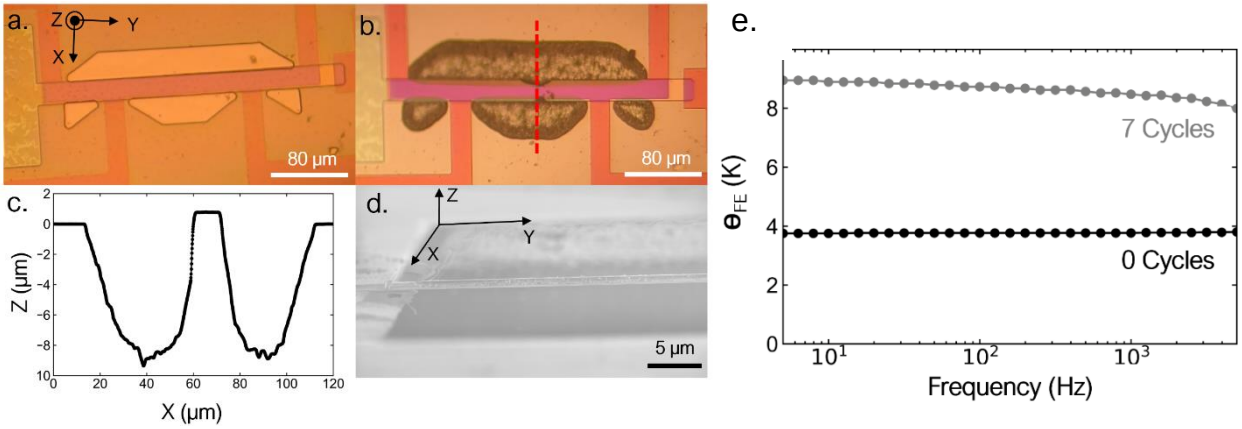

Figure 6.17: a) Optical images of the developed photoresist mask displaying an exposed Si substrate window. b) Post-XeF_2 Si etch after 7 cycles c) Profilometer height line profile (red dashed line Figure 2b) through the Si etch pit across the pyroelectric test platform. d) SEM image of fully under etched pyroelectric beam. e) Ferroelectric temperature oscillation amplitude as a function of heating current frequency and number of XeF_2 under etch cycles.

Chapter 7
Summary of Findings and Suggestions for Future Work

7.1 Summary of Findings

In this section, I summarize the main conclusions from this Dissertation.

1-*Dielectric/piezoelectric susceptibility enhancement design rules to not directly apply to pyroelectrics:* Although a naïve standpoint would initially suggest that routes toward π enhancement would closely align to the previously developed design rules for enhancing dielectric/piezoelectric susceptibilities, a more complex scenario quickly arises upon actually probing such concepts. Within Chapter 5, the development of a comprehensive, high-frequency and applied DC bias pyroelectric characterization methodology allowed me to uncover the compositional dependence of π within the $PbZr_xTi_{1-x}O_3$ system. As a prototypical ferroelectric, $PbZr_xTi_{1-x}O_3$ has decades of previously completed work investigating the dielectric/piezoelectric response as a function of numerous stimuli (*i.e.*, chemistry, strain, domain architectures, temperature, pressure etc.). Among these various control parameters to enhance susceptibility, I turned my attention towards the morphotropic phase boundary (MPB) in which the relatively flat energetic landscape allows for the facile reorientation of polarization under applied electric fields. The MPB (occurring at or near the $PbZr_{0.52}Ti_{0.48}O_3$ chemistry), defined as a compositional phase boundary between the tetragonal and rhombohedral phases of $PbZr_xTi_{1-x}O_3$, has historically been used to maximize both dielectric and piezoelectric response without the limiting consequences of high-temperature operation associated with T_c-based π enhancement. As a result, I demonstrated that the magnitude of π monotonically decreases across the MPB as the zirconium-rich phase is reached. Although specific pyroelectric contributions are maximized at the MPB composition (*e.g.*, secondary and dielectric contributions), the complex competing contribution response works against the total measured π.

2-*Pyroelectric response consists of convoluted and competing contributions.* Associated with highly-functional pyroelectrics is the inevitable, complex material property interplay due to the intrinsically coupled electrical, mechanical, and thermal susceptibilities. As a result, pyroelectric response consists of a convolution of effects arising from the domain configuration, mechanical and thermal coupling to underlying substrates, thermally induced non-pyroelectric currents, and electric-field susceptibility which all work or compete in conjunction. Through comprehensive characterization methodologies, I demonstrated the inherent contribution trade-offs as one traverses the MPB of the $PbZr_xTi_{1-x}O_3$ system. Specifically, as the zirconium-rich phase is approached, both the total and intrinsic pyroelectric response monotonically decrease to zero from negative π values. In contrast, however, the secondary contribution, which is partially dictated by the piezoelectric response of the thin film, exhibits a maximum negative response at the MPB but quickly falls of as one transitions away from the MPB in chemistry coinciding with a reduction in the piezoelectric coefficients. In direct contrast, the dielectric response works against the total π and is once again maximized in the vicinity of the MPB composition. Only after the independent

investigation of the numerous contributions can facile routes for π enhancement be determined. In this case, by maintaining tetragonal symmetry where the intrinsic contribution dominates, other contributions are minimized (even if competing in nature) and thus promotes the greatest electrothermal response.

3- *Extrinsic contributions to pyroelectric response can no longer be neglected:* Although studies have investigated the extrinsic (*i.e.*, domain-wall motion mediated) contribution to dielectric and piezoelectric susceptibility, until recently, extrinsic contributions to pyroelectricity have been neglected or limited to only phenomenological models. To systematically investigate the effects of various domain configurations to the measured pyroelectric response, I utilized compressive and tensile epitaxial strain to alter *c*- and *a*-domain fractions within 120-nm-thick $PbZr_{0.20}Ti_{0.80}O_3$ heterostructures. Through X-ray diffraction, scanning probe, and high-frequency, phase-sensitive pyroelectric characterization methods, I demonstrated that although the π magnitudes aligned with the trend in ferroelectric P_s, a more subtle underlying effect was elucidated. Namely, as the epitaxial strain evolves from the compressive to tensile regimes, a sign conversion of the extrinsic contribution is exhibited. While maintaining primarily *c*/*a*-domain structures under compressive strain, the extrinsic contribution is positive (>0) and thus reduces the overall measured π. In contrast, this is the opposite case for tensile strain regimes where the mixed phase in-plane domain architecture prompts a negative extrinsic contribution (<0) that inevitably works to enhance the already negative total π response. In all, the extrinsic contribution can amount to as much as 35% of the total measured response in certain heterostructures and remains as an available route to tune electrothermal response.

4- *Global utilization of specific comprehensive pyroelectric characterization methods is crucial for the advancement of pyroelectrics.* Unlike the comprehensive and globally applied characterization methodologies of the dielectric and piezoelectric communities, pyroelectric investigation has prompted the development of more than 20 varying metrology techniques over the past three decades. As a result, reported electrothermal findings often introduce contradictions that cannot be clearly attributed to measurements protocols or differing pyroelectric systems. As a result, key to the rapid development of physical pyroelectric insights is the advancement and use of comprehensive characterization metrologies that minimize spurious, thermally stimulated currents and other non-pyroelectric signals that often accompany highly-susceptible ferroelectric systems. By using high-frequency, AC phase-sensitive electrothermal test platforms and accompanying thermal characterization metrologies (3-Omega and TCR), I was able to independently suppress contributions to π and advance the understanding of the various coupled contributions to electrothermal response. Additionally, through the integration of these AC, phase-sensitive techniques within in-plane oriented and under-etched pyroelectric test structures, new insights regarding possible extrinsic and secondary contributions were elucidated.

7.2 Suggestions for Future Work

In this section, I discuss additional investigations needed to promote the developments of this Dissertation in addition to the field of pyroelectrics.

1-In-plane pyroelectric response of $PbTiO_3$-based heterostructures: To continue the development and validation of the in-plane electrothermal test platforms, incorporation of a purely in-plane oriented electrode geometry is needed. From preliminary efforts, it is possible to directly deposit thin-film $PbTiO_3$ onto exposed substrate surfaces which lie between laterally adjacent $SrRuO_3$ IDE fingers. In contrast to prototypical IDE geometries which sit above the blanket layer dielectric, clearly defined electrode contact areas with the pyroelectric thin-film dramatically reduces the complexities of subsequent π calculations. With this updated device geometry, epitaxially strained $PbTiO_3$ thin-films maintaining purely *c* and *a* oriented domain structures would be measured and compared to standard out-of-plane pyroelectric metrologies. Ideally, the purely in-plane oriented domain heterostructures would report π_x magnitudes similar to π_z magnitudes measured on purely out-of-plane oriented domain systems. Lastly, with a validated test platform, the complex in-plane nature of $(PbTiO_3)_n/(SrTiO_3)_n$ superlattices would be elucidated as a function of DC-electric fields, superlattice periodicity and temperature. These three tuning parameters allow one to systematically introduce phase competition and polarization instabilities which have previously been demonstrated to enhance susceptibility. Additionally, by applying comprehensive contribution extraction methodologies (Chapter 5), the various in-plane contributions to pyroelectricty can be quantitatively studied.

2-Novel pyroelectric phenomena from emergent polarization topologies: Progress in the synthesis of nearly-perfect oxide interfaces with unit-cell control has allowed the creation of superlattice heterostructures where emergent phenomena such as new polar topologies (skyrmions and vortex structures) [1,2] are characterized by an additional order parameter: the electric toroidal moment. The toroidal moment, originally proposed for zero-dimensional ferroelectrics [3], should give rise to new phases (ferrotoroidic, antiferrotoroidic), as well as new electromechanical (piezotoroidic) and electrothermal (pyrotoroidic) couplings. The latter emerges from the temperature dependence of the toroidal moment, described by the corresponding pyrotoroidic tensor [4]. The converse effect, the toroidocaloric effect [5], is also possible, where a curl of electric field produces a temperature change in a system with polar vortices. Today we await careful study of these effects.

3-Pyromagnetism and pyro-electric-magnetic effects: The pyromagnetic effect is analogous to the pyroelectric effect – it is the change of the spontaneous magnetization of a material with a change in temperature. The question then arises, can we use the pyromagnetic and pyroelectric effects in tandem to achieve something new? Leveraging advances in materials, pyroelectric measurements, and related fields like multiferroics and magnetoelectrics, the community seems poised to address this question. What one might call pyro-electric-magnetic effects could be possible in multiferroic/magnetoelectric systems wherein one obtains both pyroelectric (from the polar order) and pyromagnetic (from the magnetic order) effects from a single or composite system. This could, in turn, produce larger values of pyroelectric current, provide for new coupling effects, or open the way for novel applications. For example, the field of thermomagnetic conversion has been studied for some years [60] and is, again, analogous to PEC. The idea being that temperature oscillations drive a time-

varying magnetic flux that induces a current in a solenoid. Nonetheless, questions then arise whether composite structure can be designed to leverage these two effects (pyroelectric energy and thermomagnetic conversion) in order to create new record-breaking conversion efficiencies and energy/power densities.

4-Electrocaloric effects leveraging the new measurement platforms: The measurement protocols developed in the last few years for pyroelectrics can also be applied to other effects, such as the electrocaloric effect. The small thermal mass of thin films with respect to the supporting substrates has so far prevented the direct measurement of these temperature changes, which are (like pyroelectricity) primarily obtained indirectly by measuring the temperature dependence of the order parameter and applying Maxwell relations to obtain temperature and entropy changes. In order to be applied correctly, these relations, require knowledge of the temperature and field dependence of heat capacity and careful attention to the boundary conditions (*i.e.*, the stress/strain state of the film) in order to obtain accurate results. The novel electrothermal test devices developed for the accurate measurement of pyroelectric current also provide new direct probe capabilities for electrocaloric temperature changes. Indeed, researchers have [7] registered temperature changes as small as milli-Kelvin for a 150-nm-thick ferroelectric thin film in response to an electric field. Further measurements near phase transitions are required in order to verify the giant electrocaloric response reported for thin films via indirect methods. Other techniques like infrared lock-in thermography [8], may also enable non-contact and spatially resolved studies of caloric responses, provided that the heat transfer to the substrate can be reduced by, for example, fabricating suspended ferroelectric membranes [9-10]. Such "mechanically free" membranes could also enable the study of piezocaloric [11] (polarization-dependent), elastocaloric [12] (strain-dependent), and flexocaloric [13] (strain gradient-dependent) effects where strain is no longer dominated by underlying substrates, but rather the elastic compliance, thickness, and lattice misfit of the various constituent material layers of the heterostrcuture [14]. Such approaches could also allow for unprecedented function of pyroelectric-based thermal imaging/sensing devices – the full implications of these observations, however, remains to be seen as more work is undertaken.

REFERENCES

CHAPTER 2 REFERENCES

[1] S. Baoyuan, W. Jiantong, Z. Jun, Q. Min, *J. Mater. Process*. 2003, *139*, 444.
[2] M. E. Lines, A. M. Glass, *Principles and Applications of Ferroelectrics and Related Materials*. Oxford University Press: New York, United States of America. 1977.
[3] C. Shi, X.-B. Han, W. Zhang, *Coord. Chem. Rev.* 2019, *378*, 561.
[4] C. L. Wang, *Theories and Methods of First Order Ferroelectric Phase Transitions*. Intech: Rijecka, Croatia. 2010.
[5] X. S. Wang, C. L. Wang, W. L. Zhong, *Solid State Commun.* 2002, *122*, 311.
[6] D. K. Das-gupta, *Ferroelectrics.* 1991, *118*, 165.
[7] S.L. Bavina, N. V. Morozovsky, *Ferroelectrics*. 1990, *118*, 217.
[8] Y. Wada, R. Hayakawa, *Jpn. J. Appl. Phys.* 1976, *15*, 2041.
[9] S. T. Lau, C. H. Cheng, S. H. Choy, D. M. Lin, K. W. Kwok, H. L. W. Chan, *J. Appl. Phys.* 2008, *103*, 104105.
[10] Y. Zhang, M. Xie, J. Roscow, Y. Bao, K. Zhou, D. Zhang, C. R. Bowen. *J. Mater. Chem A Energy Sustain.* 2017, *5*, 6569.
[11] A. Safari, B. Jadidian, E. K. Akdogan, *Comprehensive Composite Materials.* 2000, *5*, 533.
[12] W. Yang, F. Fang, D.-N. Fang, *Comprehensive Structural Integrity*. 2003, *2*, 645.
[13] P. Muralt, *Encyclopedia of Materials: Science and Technology*. Pergamon: 2001.
[14] R. W. Whatmore, *Piezoelectric and Pyroelectric Materials and Their Applications.* Springer Science + Business Media: New York, United States of America. 1991.
[15] M. R. Srinivasan, *Bull. Mater. Sci.* 1984, *6*, 317.
[16] L. Pardo, *Power Ultrasonics.* 2015, 101.
[17] D. Damjanovic, *Rep. Prog. Phys.* 1998, *61*, 1267.
[18] H. He, X. Lu, E. Hanc, C. Chen, H. Zhang, L. Lu, *J. Mater. Chem.* 2020, *8*, 1494.
[19] M. D. Aggarwal, A. K. Batra, P. Guggilla, M. E. Edwards, *NASA Tech. Report*. 2010, M-1273.
[20] C. R. Bowen, J. Taylor, E. LeBoulbar, D. Zabek, A. Chauhan, r. Vaish, *Energy Environ. Sci.* 2014, *7*, 3817.
[21] Y. Wang, X. Liu, J. D. Burton, S. S. Jaswal, E. Y. Tsymbal. *Phys. Rev. Lett.* 2012, *109*, 247601.
[22] PH. Ghosez, X. Gonze, J.-P. Michenaud, *Europhys. Lett.* 1996, *33*, 713.
[23] S. Luo, W. a. Daoud. *J. Mater. Chem. A.* 2012, *3*, 8992.
[24] M. Johnsson, P. Lemmens, *Crystallography and Chemistry of Perovskites*. John Wiley & Sons, Ltd.: 2007.
[25] H. D. Megaw, *Proc. Phys. Soc.* 1946, *58*, 133.
[26] R. E. Cohen, *Nature*. 1992, *358*, 136.
[27] G. Venkataraman, *Bull. Mater. Sci.* 1979, *1*, 129.
[28] N. Nakanishi, A. Nagasawa, Y. Murakami, *J. Phys. I.* 1982, *43*, C4-35.
[29] A. W. Hewat, *J. Phys. C.: Solid State Phys.* 1973, *6*, 1074.
[30] Y. Zhang, Z. Chen, W. Cao, Z. Zhang, *Appl. Phys. Lett.* 2017, *111*, 172902.
[31] S. Pandya, G. Velarde, L. Zhang, L. W. Martin, *Phys. Rev. Mater.* 2018, *2*, 124405.

[32] M. Trainer, *Eur. J. Phys.* 2000, *21*, 459.
[33] F. Jona, G. Shirane, *Ferroelectric Crystals.* Dover, New York: United States of America 1993.
[34] X. Wang, A. Gong, Y. Tang, X. He, Q. He, Z. Peng, D. Sun, *Ferroelectrics.* 2010, *403*, 191.
[35] N. Izyumskaya, Y.-I. Alivov, S.-J. Cho, H. Morkoc, H. Lee, Y.-S. Kang, *Crit. Rev. Solid State.* 2007, *32*, 111.
[36] K. Uchino, S. Nomara, *J. Mater. Sci.* 1981, *16,* 569.
[37] P. Regtien, E. Dertien, *Sensors for Mechatronics*. Elsevier Inc.: 2018.
[38] T. Kanda, A. Makino, T. Ono, K. Suzumori, T. Morita, M. K. Kurosawa, *Sens. Actuators A Phys.* 2005, *127*, 131.
[39] R. Waser, U. Bottger, S. Tiedke, *Polar Oxides: Properties, Characterization, and Imaging*. Wiley-VCH: Weinheim: Great Britain 2005.
[40] X.-H. Du, J. Zheng, U. Belegundu, K. Uchino, *Appl. Phys. Lett.* 1998, *72*, 2421.
[41] A. J. Bell, *J. Mater. Sci.,* 2006, *41*, 13.
[42] M. J. Haun, E. Furman, S. J. Jang, L. E. Cross, *Ferroelectrics,* 1989, *99*, 63.
[43] J.-S. Yang, S.-H. Kim, J.-H. Yeom, C.-Y. Koo, C. S. Hwang, E. Yoon, D.-J. Kim, J. Ha, *Integr. Ferroelectr.*, 2003, *54,* 515.
[44] C. A. Randall, D. J. Barber, r. W. Whatmore, *J. Mater. Sci.* 1987, *22*, 925.
[45] J. Ricote, R. W. Whatmore, D. J. Barber, *J. Phys. Condens. Matter,* 2000, *12*, 323.
[46] T. R. Shrout, S. J. Zhang, *J. Electroceram,* 2007, *19*, 111.
[47] B. Noheda, D. E. Cox, G. Shirane, R. Guo, B. Jones, L. E. Cross, *Phys. Rev. B.* 2000, *63*, 014103.
[48] M. Acosta, N. Novak, V. Rojas, S. Patel, R. Vaish, J. Koruza, G. A. Rossetti Jr., J. Rodel, *Appl. Phys. Rev.* 2017, *4*, 041305.
[49] B. Ertug, *Am. J. Eng. Res.* 2013, *2*, 1.
[50] T. Tanaka, *Bull. Inst. Chem. Res. Kyoto Univ.* 1954, *32*, 43.
[51] D. Sitko, W. Bak, B. Garbarz-Glos, A. Budziak, C. Kajtoch, A. Kalvane, *Mater. Sci. Eng.* 2013, *49*, 012050.
[52] K. Uchino, *Advanced Piezoelectric Materials,* Woodhead Publishing: 2017.
[53] S. Roberts, *Phys. Rev.* 1947, *71,* 890.
[54] M. K. Lee, T. K. Nath, C. B. Eom, *Appl. Phys. Lett.* 2000, *77*, 3547.
[55] A. Feteira, D. C. Sinclair, I. M. Reaney, Y. Somiya, M. t. Lanagan, *J. Am. Ceram. Soc.* 2004, *87*, 1082.
[56] D. G. Schlom, L.-Q. Chen, C.-B. Eom, K. M. Rabe, S. K. Streiffer, J.-M. Triscone, *Annu. Rev. Mater. Res.* 2007, *37*, 589.
[57] J. J. Lee, C. L. Thio, S. B. Desu, *J. Appl. Phys.* 1995, *78*, 5073.
[58] L. W. Martin, D. G. Schlom, *Curr. Opin. Solid State Mater. Sci.* 2012, *16*, 199.
[59] L. W. Martin, A. M. Rappe. *Nat. Rev. Mater.* 2017, *2*, 16087.
[60] A. R. Damodaran, J. D. Clarkson, Z. Hong, H. Liu, A. K. Yadav, C. T. Nelson, S.-L. Hsu, M. R. McCarter, K.-D. Park, V. Kravstov, A. Farhan, Y. Dong, Z. Cai, H. Zhou, P. Aguado-Puente, P. Garcia-Fernandez, J. Iniquez, J. Junquera, a. Scholl, M. B. Raschke, L.-Q. Chen, D. D. Fong, R. Ramesh, L. W. Martin. *Nat. Mater.* 2017, *16*, 1003.
[61] R. Xu, J. Karthik, A. r. Damodaran, L. W. Martin, 2014, *5*, 1.

[62] J. C. Agar, A. R. Damodaran, M. B. Okatan, J. Kacher, C. Gammer, R. K. Vasudevan, S. Pandya, L. R. Dedon, R. V. K. Mangalam, G. A. Velarde, S. Jesse, N. Balke, A. M. Minor, S. V. Kalinin, L. W. Martin. *Nat. Mater.* 2016, *15*, 549.
[63] R. E. Jones Jr., P. D. Maniar, R. Moazzami, P. Zurcher, J. Z. Witowski, Y. T. Lii, P. Chu, S. J. Gillespie, *Thin Solid Films,* 1995, *270*, 584.
[64] H. Kohlstedt, Y. Mustafa, A. Gerber, A. Petraru, M. Fitsilis, R. Meyer, U. Bottger, R. Waser. *Microelectron. Eng.* 2005, *80*, 296.
[65] S. B. Lang, *Phys. Today,* 2005, *58*, 31.
[66] A. Hossain, M. H. Rashid, *IEEE Trans. Ind. Appl.* 1991, *27*, 824.
[67] S. T. Liu, D. Long, *P. IEEE.* 1978, *66*, 14.
[68] S. G. Porter, *Ferroelectrics,* 1981, *33*, 193.
[69] G. Sebald, S. Pruvost, D. Guyomar, *Smart Mater. Struct.* 2008, *17*, 015012.
[70] R. B. Olson, D. A. Bruno, J. M. Briscoe, *J. Appl. Phys.* 1985, *58*, 4709.
[71] B. Bhatia, A. R. Damodaran, H. Cho, L. W. Martin, W. P. King, *J. Apple. Phys.* 2014, *116*, 194509.
[72] S. Pandya, J. Wilbur, J. Kim, R. Gao, A. Dasgupta, C. Dames, L. W. Martin. *Nat. Mater.* 2018, *17*, 432.

CHAPTER 3 REFERENCES

[1] R. Eason, *Pulsed Laser Deposition of Thin Films*, John Wiley & Sons, Inc. New Jersey, USA 2007.
[2] J. Mittra, G. J. Abraham, M. Kesaria, S. Bahl, A. Gupta, S. M. Shivaprasad, C S. Viswanadham, U. D. Kulkarni, G. K. Dey, *Mater. Sci. Forum,* 2012, *710*, 757.
[3] M. N. R. Ashfold, F. Claeyssens, G. M. Fuge and S. J. Henley, *Chem. Soc. Rev.*, 2004, *33*, 23-31.
[4] D. H. Lowndes, D. B. Geohegan, A. A. Puretzky, D. P. Norton and C. M. Rouleau, *Science*, 1996, *273*, 898-903.
[5] A. Ichimiya and P. I. Cohen, *Reflection High Energy Electron Diffraction*, Cambridge University Press. Cambridge, United Kingdom 2004.
[6] T. Terashima and Y. Bando, *Phys. Rev. Lett.* 1990, *65,* 2684-2688.
[7] G. J. H. M. Rijnders, G. Koster, D. H. A. Blank and H. Rogalia, Appl. Phys. Lett. 1997, *70*, 1888-1890.
[8] E. Lupi, A. Ghosh, S. Saremi, S.-L. Hsu, S. Pandya, G. Velarde, A. Fernandez, R. Ramesh and L. W. Martin, *Adv. Electron. Mater.* 2020, *6*, 1901395.
[9] H. Guo, Z. Wang, S. Dong, S. Ghosh, M. Sahayezhian, L. Chen, Y. Weng, A. Herklotz, T. Z. Ward, R. Jin, S. T. Pantelides, Y. Zhu, J. Zhang and E. W. Plummer, *PNAS*, 2017, E5062-E5069.
[10] G. Herranz, F. Sanchez, N. Dix, M. Scigaj and J. Fontcuberta, *Sci. Rep.* 2012, *2*, 1-5.
[11] P. Kuppusami and V. s. Raghunathan, *Surf. Eng.* 2006, *2*, 81-83
[12] R. J. Narayan, *Diam. Relat. Mater.* 2005, *14*, 1319-1330.
[13] R. E. Honig, *RCA Review*, 1957, *18*, 295-204.
[14] R. J. Brook, *Concise Encyclopedia of Advanced Ceramic Material*, Pergamon, 1991.
[15] P. Duran and C. Moure, *J. Mater. Sci.* 1985, *20*, 827-833.
[16] X. Wang, Y. Liu, X. Xu, S. Fu, and Z. Cui, *J. Vac. Sci. Technol. A.* 2006, *24*, 1067.

[17] S. Aggarwal, S. R. Perusse, C. W. Tipton and R. Ramesh, *Appl. Phys. Lett.* 1998, *73*, 1973-1975.
[18] S. Aggarwal, S. r. Perusse, B. Nagaraj and R. Ramesh, 1999, *74*, 3023-3025.
[19] A. Piccirillo and A. L. Gabbi, *J. Electrochem. Soc.* 1990, *137*, 3910-3917.
[20] D. G. Cahill, M. Katiyar and J. R. Abelson, *Phys. Rev. B.* 1994, *50*, 6077-6081.
[21] M. E. Marssi, F. Le Marrec, I. A. Lukyanchuk and M. G. Karkut, *J. Apple. Phys.* 2003, *94*, 3307-3312.
[22] P. Zubko, N. Stucki, C. Lichtensteiger and J.-M. Triscone, *Phys. Rev. Lett.* 2010, *104*, 187601.
[23] K. S. Lee, Y. K. Kim and S. Baik, *Appl. Phys. Lett.* 2001, *79*, 2444-2446.
[24] K. Y. Yun, M. Noda and M. Okuyama, *Appl. Phys. Lett.* 2003, *83*, 3981.
[25] H. N .Lee, H. M. Christen, M. F. Chisholm, C. M. Rouleau and D. H. Lowndes, *Nature*, 2005, *433*, 395-399.
[26] C. J. Humphreys, *Acta Crystallogr. A*, 2012, *A69*, 45-50.
[27] A. Monshi, M. R. Foroughi and M. R. Monshi, *WJNSE*, 2012, *2*, 154-160.
[28] H.-J. Liu, C.-W. Liang, Wen-I Liang, H.-J. Chen, J.-C. Yang, C.-Y. Peng, G.-F. Wang, F.-N. Chu, Y.-C. Chen, H.-Y. Lee, L. Chang, S.-J. Lin and Y.-H. Chu, *Phys. Rev. B.* 2012, *85*, 014104.
[29] J. Perriere, *Vacuum*, 1987, *37*, 429-432.
[30] L. R. Doolittle, *Nucl. Instrum. Methods Phys. Res.* 1985, *B9*, 344-351.
[31] D. Rugar and P. Hansma, *Phys. Today*, 1990, *10*, 23-30.
[32] F. Golek, P. Mazur, Z. Ryszka and S. Zuber, *Appl. Surf. Sci.* 2014, *304*, 11-19.
[33] E. Jensen, *Anat. Rec.* 2013, *296*, 179-183.
[34] G. Haugstad, *Atomic Force Microscopy: Understanding Basic Modes and Advanced Applications.* John Wiley & Sons, Inc. New Jersey, USA 2012.
[35] R. Garcia and A. San Paulo, *Phys. Rev. B.* 1999, *60*, 4961-4967.
[36] S. N. Magonov, V. Elings, M.-H. Whangbo, *Surf. Sci.* 1997, *375*, L385-L391.
[37] A. F. Pun, X. Wang, J. B. Meeks and J. P. Zheng, 2004, *96*, 6357-6361.
[38] S. Pandya, A. R. Damodaran, R. Xu, S.-L. Hsu, J. C. Agar and L. W. Martin, *Sci. Rep.* 2016, *6*, 26075.
[39] B. Koo, K. Kim, J. K. Kim, H. Kwon, J. W. Han and W. Jung, *Joule*, 2018, *2*, 1476-1499.
[40] Y. F. Dufrene, T. Ando, R. Garcia, D. Alsteens, D. Martinez-Martin, A. Engel, C. Gerber and D. J. Muller, *Nat. Nanotechnol.* 2017, *12*, 295-307.
[41] A. Gruverman, M. Alexe and D. Meier, *Nat. Commun.* 2019, *10*, 1661.
[42] A.R. Damodaran, J. D. Clarkson, Z. Hong, H. Liu, A. K. Yadav, C. t. Nelson, S.-L. Hsu, M. R. McCarter, K.-D. Park, V. Kravtsov, a. Farhan, Y. Dong, Z. Cai, P. Aguado-Puente, P. Garcia-Fernandez, J. Inigues, J. Junquera, A. Scholl, M. B. Raschke, L.-Q. Chen, D. D. Fong, R. Ramesh and L. W. Martin, *Nat. Mater.* 2017, *16*, 1003-1009.
[43] L. M. Garten, M. Burch, A. S. Gupta, R. Haislmaier, V. Gopalan, E. C. Dickey, S. Trolier-McKinstry, *J. Am. Ceram. Soc.* 2016, *99*, 1645-1650.
[44] J. C. Agar, A. R. Damodaran, M. B. Okatan, J. Kacher, C. Gammer, R. K. Vasudevan, S. Pandya, L. R. Dedon, R. V. K. Mangalam, G. A. Velarde, S. Jesse, N. Balke, A. M. Minor, S. V. Kalinin and L. W. Martin, *Nat. Mater.* 2016, *15*, 549-556.
[45] J. F. Scott, *J. Phys.: Condens. Matter.* 2008, *20*, 021001.

[46] G. Sebald, L. Seveyrat, D. Guyomar, L. Lebrun, B. Guiffard and S. Pruvost, *J. Appl. Phys.* 2006, *100*, 124112.
[47] X. Wang, Z. Gong, Y. Tang, X. He, Q. He, Z. Peng and D. Sun, *Ferroelect.* 2010, *403*, 191-195.
[48] C. Ang and Z. Yu, *Appl. Phys. Lett.* 2004, *85*, 3821-3823.
[49] N. Bassiri-Gharb, I. Fujii, E. Hong, S. Trolier-McKinstry, D. V. Taylor and D. Damjanovic, *J. Electroceram.* 2007, *19*, 49-67.
[50] B. Nagaraj, S. Aggarwal, T. K. Song, t. Sawhney and R. Ramesh, *Phys. Rev. B.*
[51] W. F Leonard and R. L. Ramey, *J. Appl. Phys.* 1966, *37*, 3634-3635.
[52] D. G. Cahill, *Rev. Sci. Instrum.*, 1990, *61*, 802-808.
[53] D. G. Cahill, M. Katiyar and J. R. Abelson, *Phys. Rev. B.* 1994, *50*, 6077-6081.
[54] T. Borca-Tasciuc, A. R. Kumar and G. Chen, *Rev. Sci. Instrum.* 2001, *72*, 2139-2147.
[55] C. Dames, *Measuring the Thermal Conductivity of Thin Films: 3 Omega and Related Electrothermal Methods,* Annu. Rev. Heat Transfer, Beggel House, New York 2013.
[56] G. Weheyer, A. Pickel and W. Hodges, *1 Basic Theory for Classic Bulk 3-Omega.* Berkeley, CA USA, 2015.
[57] H. S. Carslaw and J. C. Jaeger, *Conduction of Heat in Solids*, Clarendon, Oxford 1959.
[58] S. Jachalke, E. Mehner, H. Stocker, J. Hanzig, M. Sonntag, T. Weigel, T. Leisegang and D. C. Meyer, *Appl. Phys. Rev.* 2017, *4*, 021303.
[59] D. W. Denlinger, e. N. Abarra, K. Allen, P. W. Rooney, M. t. Messer, S. K. Watson and F. Hellman, *Rev. Sci. Instrum,* 1994, *65*, 946-959.
[60] S. Pandya, J. D. Wilbur, B. Bhatia, A. R. Damodaran, C. Monachon, A. Dasgupta, W. P. King, C. Dames and L. W. Martin, *Phys. Rev. Appl.* 2017, *7*, 034025.
[61] L. Pintilie, M. Alexe, I. Pintilie and I. Boierasu, *Ferroelectrics*, 1997, *201*, 217.
[62] H. Okino, Y. Toyoda, M. Shimizu, T. Horiuchi, T. Shiosaki and K. Matsushige, *Jpn. J. Appl. Phys.* 1998, *37*, 5137.

CHAPTER 4 REFERENCES

[1] A. J. Moulson and J. M. Herbert, Electroceramics. *John Wiley & Sons Inc., England*, 2003.
[2] R. V. K. Mangalam, J. Karthik, A. R. Damodaran, J. C. Agar and L. W. Martin, *Adv. Mater.* 2013, *25*, 1761-1767.
[3] Z. Zuo, B. Chen, Q.-F. Zhan, Y. Liu, H. Yang, Z. Li, G. Xu and R.-W. Li, *J. Phys. D.: Appl. Phys.* 2012, *45*, 185302.
[4] R. Dinu, M. Dinescu, J. D. Pedarnig, R. A. Gunasekaran, D. Bauerle, S. Bauer-Gogonea and S. Baur, *Appl. Phys. A.* 1999, *69*, 55-61.
[5] J. C. Agar, A. R. Damodaran, G. A. Velarde, S. Pandya, R. V.K. Mangalam and L. W. Martin, *ACS Nano*, 2015, *9*, 7332-7342.
[6] C. Borderon, A. E. Brunier, K. Nadaud, r. Renoud, M. Alexe and H. W. Gundel, *Sci. Rep.*, 2017, *7*, 3444.
[7] Q. M. Zhang, H. Wang, N. Kim and L. E. Cross, *J. Appl. Phys.* 1994, *75*, 454-459.
[8] K. Coleman, S. Shetty, B. Hanrahan, W. Zhu and S. Trolier-McKinstry, *J. Appl. Phys.* 2020, *128*, 114102.

[9] J. C. Agar, R. V. K. Mangalam, A. R. Damodaran, G. Velarde, J. Karthik, M. B. Okatan, Z. H. Chen, S. Jesse, N. Balke, S. V. Kalinin and L. W. Martin, *Adv. Mater. Interfaces,* 2014, *1*, 1400098.
[10] M. Narayanan, S. Tong, S. Liu, B. Ma and U. Balachandran, *Appl. Phys. Lett.* 2013, *102*, 062906.
[11] N. Bassiri-Gharb, I. Fujii, E. Hong, S. Trolier-McKinstry, D. V. Taylor and D. Damjanovic, *J. Electroceram.* 2007, *19*, 49-67.
[12] D. V. Taylor and D. Damjanovic, *Appl. Phys. Lett.* 1998, *73*, 2045-2047.
[13] F. Xu, S. Trolier-McKinstry, W. Ren, B. Xu, Z.-L. Xie and K. J. Hemker, *J. Appl. Phys.* 2001, *89*. 1336-1348.
[14] D.-J. Kim, J.-P. Maria, A. I. Kingon and S. K. Streiffer, *J. Appl. Phys.* 2003, *93,* 5568-75.
[15] F. Li, S. Zhang, Z. Xu, X. Wei, J. Luo and T. R. Shrout, *J. Appl. Phys.* 2010, *108*, 034106.
[16] S. Li, A. S. Bhalla, R. E. Newnham and L. E. Cross, *Mater. Lett.* 1993*, 17*, 21-26.
[17] D. Damjanovic and M. Demartin, *J. Phys. D: Appl. Phys.* 1996, *29*, 2057.
[18] F .Xu, S. Trolier-McKinstry, W. Ren, B. Xu, Z.-L. Xie and K. J. Hemker, *J. Appl. Phys.* 2001, *89*, 1336.
[19] R. E. Eitel, T. R. Shrout and C. A. Randall, *J. Appl. Phys.* 2006, *99*, 124110.
[20] I. S. Zheludev, *Physics of Crystalline Dielectrics*, Plenum Press, New York USA 1971.
[21] L. W. Martin and A. M. Rappe, *Nat. Rev. Mater.* 2017, *2*, 16087.
[22] Y. Wang, H. Zhao, L. Zhang, J. Chen and X. Xing, *Phys. Chem. Chem. Phys.* 2017, *19*, 17493-17515.
[23] M. Mtebwa, A. K. Tagantsev and N. Setter, *AIP Advances*, 2014, *4*, 127150.
[24] J. Liu, W. Chen, B. Wang and Y. Zheng, *Materials*, 2014, *7*, 6502-6568.
[25] A. R. Damodaran, S. Pandya, J. C. Agar, Y. Cao, R. K. Vasudevan, R. Xu, S. Saremi, Q. Li, J. Kim, M. R. McCarter, L. R. Dedon, T. Angsten, N. Balke, S. Jesse, M. Asta, S. V. Kalinin and L. W. Martin, *Adv. Mater.* 2017, *29*, 1702069.
[26] W. Pompe, X. Gong, Z. Suo and J. S. Speck, *J. Appl. Phys.* 1993, *74*, 6012.
[27] L. You, Z. Chen, X. Zou, H. Ding, W. Chen, L. Chen, G. Yuan and J. Wang, *ACS Nano*, 2012, *6*, 5388-5394.
[28] J. C. Agar, A. R. Damodaran, G. A. Velarde, S. Pandya, R. V. K. Mangalam and L. W. Martin, *ACS Nano*, 2015, *9*, 7332-7342.
[29] J. C. Agar, A. R. Damodaran, M. B. Okatan, J. Kacher, C. Gammer, R. K. Vasudevan, S. Pandya, L. R. Dedon, R. V. K. Mangalam, G. A. Velarde, S. Jesse, N. Balke, A. M. Minor, S. V. Kalinin and L. W. Martin, *Nat. Mater.* 2016, *15*, 549-556.
[30] K. Zhu, S. Wu, B. Song, G. Ge, Y. Shi, L. Xu, H. Yan, B. Shen and J. Zhai, *J. Mater. Chem. C.* 2020, *8*, 17114-17121.
[31] C. Dames, *Measuring the Thermal Conductivity of Thin Films: 3 Omega and Related Electrothermal Methods,* Annu. Rev. Heat Transfer, Beggel House, New York 2013.
[32] R. Ma, Z. Zhang, K. Tong, D. Huber, R. Kornbluh, Y. S. Ju, Q. Pei, *Science (80-.).* 2017, *357*, 1130.
[33] S.-G. Lu, Q. Zhang, *Adv. Mater.* 2009, *21*, 1983.
[34] X. Moya, S. Kar-Narayan, N. D. Mathur, *Nat. Mater.* 2014, *13*, 439.
[35] S. W. Choi, R. T. R. Shrout, S. J. Jang, A. S. Bhalla, *Ferroelectrics* 1989, *100*, 29.

[36] F. Le Goupil, J. Bennett, A.-K. Axelsson, M. Valant, A. Berenov, A. J. Bell, T. P. Comyn, N. M. Alford, *Appl. Phys. Lett.* 2015, *107*, 172903.
[37] B. Neese, B. Chu, S.-G. Lu, Y. Wang, E. Furman, Q. M. Zhang, *Science (80-.).* 2008, *321*, 821.
[38] X. Moya, E. Stern-Taulats, S. Crossley, D. González-Alonso, S. Kar-Narayan, A. Planes, L. Mañosa, N. D. Mathur, *Adv. Mater.* 2013, *25*, 1360.
[39] K. J. Choi, M. Biegalski, Y. L. Li, A. Sharan, J. Schubert, R. Uecker, P. Reiche, Y. B. Chen, X. Q. Pan, V. Gopalan, L.-Q. Chen, D. G. Schlom, C. B. Eom, *Science* 2004, *306*, 1005.
[40] A. R. Damodaran, S. Pandya, Y. Qi, S. L. Hsu, S. Liu, C. Nelson, A. Dasgupta, P. Ercius, C. Ophus, L. R. Dedon, J. C. Agar, H. Lu, J. Zhang, M. Andrew, A. M. Rappe, L. W. Martin, *Nat. Commun.* 2017, *8*, 1.
[41] J. H. Haeni, P. Irvin, W. Chang, R. Uecker, P. Reiche, Y. L. Li, S. Choudhury, W. Tian, M. E. Hawley, B. Craigo, A. K. Tagantsev, X. Q. Pan, S. K. Streiffer, L. Q. Chen, S. W. Kirchoefer, J. Levy, D. G. Schlom, *Nature* 2004, *430*, 758.
[42] J. C. Agar, A. R. Damodaran, M. B. Okatan, J. Kacher, C. Gammer, R. K. Vasudevan, S. Pandya, L. R. Dedon, R. V. K. Mangalam, G. A. Velarde, S. Jesse, N. Balke, A. M. Minor, S. V. Kalinin, L. W. Martin, *Nat. Mater.* 2016, *15*, 549.
[43] R. J. Zeches, M. D. Rossell, J. X. Zhang, A. J. Hatt, Q. He, C.-H. Yang, A. Kumar, C. H. Wang, A. Melville, C. Adamo, G. Sheng, Y.-H. Chu, J. F. Ihlefeld, R. Erni, C. Ederer, V. Gopalan, L. Q. Chen, D. G. Schlom, N. A. Spaldin, L. W. Martin, R. Ramesh, *Science (80-.).* 2009, *326*, 977.
[44] J. Karthik, J. C. Agar, A. R. Damodaran, L. W. Martin, *Phys. Rev. Lett.* 2012, *109*, 257602.
[45] J. Karthik, L. W. Martin, *Phys. Rev. B* 2011, *84*, 024102.
[46] C. M. Foster, W. Pompe, A. C. Daykin, J. S. Speck, *J. Appl. Phys.* 1996, *79*, 1405.
[47] W. Pompe, X. Gong, Z. Suo, J. S. Speck, *J. Appl. Phys.* 1993, *74*, 6012.
[48] P.-E. Janolin, *J. Mater. Sci.* 2009, *44*, 5025.
[49] Z. Li, M. Grimsditch, X. Xu, S.-K. Chan, *Ferroelectrics* 1993, *141*, 313.

CHAPTER 5 REFERENCES

[1] Jachalke, A.; Mehner, E.; Stocker, H.; Hanzig, J.; Sonntag, M.; Weigel, T.; Leisegang, T.; Meyer, D. C. How to Measure the Pyroelectric Coefficient? *Appl. Phys. Rev.* 2017, *4*, 021303.
[2] Lines, M. E.; Glass, A. M. Principles and Applications of Ferroelectrics and Related Materials. *Oxford University, New York,* 1977.
[3] Whatmore, R. W. Pyroelectric Devices and Materials. *Rep. Prog. Phys.* 1986, *49*, 1335-1386.
[4] Hadni, A. Applications of the Pyroelectric Effect. *J. Phys. E.* 1981, *14*, 1233-1240.
[5] Mischenko, A. S.; Zhang, Q.; Scott, J. F.; Whatmore, R. W.; Mathur, N. D. Giant Electrocaloric Effect in the Thin Film Relaxor Ferroelectric $0.9PbMg_{1/3}Nb_{2/3}O_3$-$0.1PbTiO_3$ Near Room Temperature. *Science* 2006, *311*, 1270-1271.
[6] Damjanovic, D. Comments on Origins of Enhanced Piezoelectric Properties in Ferroelectrics. *IEEE Trans. Ultrason. Ferroelectr. Freq. Control.* 2009, *56,* 1574-1585.

[7] Fu, H.; Cohen, R. E. Polarization Rotation Mechanism for Ultrahigh Electromechanical Response in Single-Crystal Piezoelectrics. *Nature.* 2000, *403,* 281-283.
[8] Noheda, B.; Cox, D. E.; Shirane, G.; Park, S.-E.; Cross, L. E.; Zhong, Z. Polarization Rotation via a Monoclinic Phase in the Piezoelectric 92%$PbZn_{1/3}Nb_{2/3}O_3$-8%$PbTiO_3$. *Phys. Rev. Lett.* 2001, *86,* 3891-3894.
[9] Damjanovic, D. A Morphotropic Phase Boundary System Based on Polarization Rotation and Polarization Extension. *Appl. Phys. Lett.* 2010, *97,* 062906.
[10] Teowee, G.; McCarthy, F. S.; McCarthy, K. C.; Dietz, B. H.; Uhlmann, D. R. Pyroelectric Properties of Sol-Gel Derived PZT Thin Films with Various Zr/Ti Ratios. *Integr Ferroelectr* 1998, *22,* 431-438.
[11] Yang, J.-S.; Kim, S.-H.; Yeom, J.-H.; Koo, C.-Y.; Hwang, C. S.; Yoon, E.; Kim, D.-J.; Ha, J. Piezoelectric and Pyroelectric Properties of $Pb(Zr,Ti)O_3$ Films for Micro-Sensors and Actuators. *Integr Ferroelectr* 2003, *54,* 515-525.
[12] Xiao, B.; Avrutin, V.; Liu, H.; Ozugur, U.; Morkoc, H.; Lu, C. Large Pyroelectric Effect in Undoped Epitaxial $Pb(Zr,Ti)O_3$ Thin Films on $SrTiO_3$ Substrates. *Appl. Phys. Lett.* 2008, *93,* 052913.
[13] Arora, A. K.; Tandon, R. P.; Mansingh, A. Piezoelectric, Pyroelectric and Dielectric Properties of Lanthanum Modified Lead Zirconate Titanate Ceramics. *Ferroelectrics.* 1992, *132,* 9-25.
[14] Karthik, J.; Martin, L. W. Pyroelectric Properties of Polydomain Epitaxial $Pb(Zr_{1-x}Ti_x)O_3$ Thin Films. *Phys. Rev. B.* 2011, *84,* 024102.
[15] Karthik, J.; Agar, J. C.; Damodaran, A. R.; Martin, L. W. Effect of 90° Domain Walls and Thermal Expansion Mismatch on the Pyroelectric Properties of Epitaxial $PbZr_{0.2}Ti_{0.8}O_3$ Thin Films. *Phys. Rev. Lett.* 2012, *109,* 257602.
[16] Karthik, J.; Damodaran, A. R.; Martin, L. W. Effect of 90° Domain Walls on the Low-Field Permittivity of $PbZr_{0.2}Ti_{0.8}O_3$ Thin Films. *Phys. Rev. Lett.* 2012, *108,* 167601.
[17] Tang, Y.; Zhang, S.; Shen, Z.; Jiang, W.; Luo, J.; Sahul, R.; Shrout, T. R. Primary and Secondary Pyroelectric Coefficients of Rhombohedral and Tetragonal Single-Domain Relaxor-$PbTiO_3$ Single Crystals. *J. Appl. Phys.* 2013, *114,* 084105.
[18] Zook, J. D.; Liu, S. T. Pyroelectric Effects in Thin Film *J. Appl. Phys.* 1978, *49,* 4604-4606.
[19] Kosorotov, V. F.; Kremenchugskij, L. S.; Levash, L. V.; Shchedrina, L. V. Tertiary Pyroelectric Effect in Lithium Niobate and Lithium Tantalate Crystals. *Ferroelectrics.* 1986, *70,* 27-37.
[20] Karthik, J.; Martin, L. W. Effect of Domain Walls on the Electrocaloric Properties of $Pb(Zr_{1-x}Ti_x)O_3$ Thin Films. *Appl. Phys. Lett.* 2011, *99,* 032904.
[21] Li, X.; Lu, S.-G.; Chen, X.-Z.; Gu, H.; Qian, X.-S.; Zhang, Q.M. Pyroelectric and Electrocaloric Materials. *J. Mater. Chem. C.* 2013, *1,* 23-37.
[22] Pandya, S. P.; Wilbur, J. D.; Bhatia, B.; Damodaran, A. R.; Monachon, C.; Dasgupta, A.; King, W. P.; Dames, C.; Martin, L. W. Direct Measurement of Pyroelectric and Electrocaloric Effects in Thin Films. *Phys. Rev. Appl.* 2017, *7,* 034025.
[23] Hanrahan, B.; Espinal, Y.; Nevile, C.; Rudy, R.; Rivas, M.; Smith, A.; Kesim, M.T.; Aplay, S.P. Accounting for the Various Contributions to Pyroelectricity in Lead Zirconate Titanate Thin Films. *J. Appl. Phys.* 2018, *123*, 124104.

[24] Pandya, S.; Damodaran, A.R.; Xu, R.; Hsu, S.L.; Agar, J.C.; Martin, L.W. Strain-Induced Growth Instability and Nanoscale Surface Patterning in Perovskite Thin Films. *Sci. Rep.* 2016, *6,* 26075.
[25] Pandya, S.; Velarde, G. A.; Gao, R.; Everhardt, A. S.; Wilbur, J. D.; Xu, R.; Maher, J. T.; Agar, J. C.; Dames, C.; Martin, L. W. Understanding the Role of Ferroelastic Domains on the Pyroelectric and Electrocaloric Effects in Ferroelectric Thin Films. *Adv. Mater*. 2019, *31,* 1803312.
[26] Damodaran, A. R.; Agar, J. C.; Pandya, S.; Chen, Z.; Dedon, L.; Xu, R.; Apgar, B.; Saremi, S.; Martin, L. W. New Modalities of Strain-Control of Ferroelectric Thin Films. *J. Phys.: Condens. Matter* 2016, *28,* 263001.
[27] Dames, C. Annual Review of Heat Transfer*. Begell House, New York* 2013, *16,* 7-48.
[28] Tong, T.; Karthik, J.; Martin, L. W.; Cahill, D. G. Secondary Effects in Wide Frequency Range Measurements of the Pyroelectric Coefficient of $Ba_{0.6}Sr_{0.4}TiO_3$ and $PbZr_{1-x}Ti_xO_3$ Epitaxial Layers. *Phys. Rev. B.* 2014, *90,* 155423.
[29] Xu, F.; Trolier-McKinstry, S.; Ren, W.; Xu, B.; Xie, Z.-L.; Hemker, K. J. Domain Wall Motion and its Contribution to the Dielectric and Piezoelectric Properties of Lead Zirconate Titanate Films. *J. Appl. Phys.* 2011, *89,* 1336-1348.
[30] Agar, J. C.; Mangalam, R. V. K.; Damodaran, A. R.; Velarde, G.; Karthik, J.; Okatan, M. B.; Chen, Z. H.; Jesse, S.; Balke, N.; Kalinin, S. V.; Martin, L. W Tuning Susceptibility via Misfit Strain in Relaxed Morphotropic Phase Boundary $PbZr_{1-x}Ti_xO_3$ Epitaxial Thin Films. *Adv. Mater. Interfaces* 2014, *1,* 140098.
[31] Ang, C.; Yu, Z. Dielectric Behavior of $PbZr_{0.52}Ti_{0.48}O_3$ Thin Films: Intrinsic and Extrinsic Dielectric Responses. *Appl. Phys. Lett.* 2004, *85,* 3821-3823.
[32] Cahill, D. G. Thermal Conductivity Measurement from 30 to 750 K: the 3ω Method. *Rev. Sci. Instrum.*1990, *61,* 802-808.
[33] Pandya, S.; Wilbur, J.; Kim, J.; Gao, R.; Dasgupta, A.; Dames, C.; Martin, L. W. Pyroelectric Energy Conversion with Large Energy and Power Density in Relaxor Ferroelectric Thin Films. *Nat. Mater.* 2018, *17,* 432-438.
[34] Ye, C-P.; Tamagawa, T.; Polla, D. L. Experimental Studies on Primary and Secondary Pyroelectric Effects in $Pb(Zr_{1-}xTix)O_3$, $PbTiO_3$, and ZnO Thin Films. *J. Appl. Phys.* 1991, *70,* 5538-5543.
[35] Lang, S. Pyroelectric Coefficient of Lithium Sulfate Monohydrate (4.2-320°K) *Phys. Rev. B.* 1971, *4*, 3603-3609.
[36] Kurz, N.; Lu, Y.; Kirste, L.; Reusch, M.; Zukauskaite, A.; Lebedev, V.; Ambacher, O. Temperature Dependence of the Pyroelectric Coefficient of AlScN Thin Films. *Phys. Status Solidi A.* 2018, *215,* 1700831.
[37] Damjanovic, D. Ferroelectric, Dielectric and Piezoelectric Properties of Ferroelectric Thin Films and Ceramics. *Rep. Prog. Phys.* 1998, *61,* 1267-1324.
[38] Haun, M. J.; Furman, E.; Jang, S.J.; Cross, L. E. Thermodynamic Theory of the Lead Zirconate-Titanate Solid Solution System, Part V: Theoretical Calculations. *Ferroelectrics* 1989, *99,* 63-86.
[39] Damodaran, A. R.; Pandya, S.; Agar, J. C.; Cao, Y.; Vasudevan, R. K.; Xu, R.; Saremi, S.; Li, Q.; Kim, J.; McCarter, M.R.; Dedon, L. R.; Angsten, T.; Balke, N.; Jesse, S.; Asta, M.;

Kalinin, S.V.; Martin, L. W. Three-State Ferroelastic Switching and Large Electromechanical Responses in $PbTiO_3$ Thin Films. *Adv. Mater.* 2017, *29,* 1702069.
[40] Pertsev, N. A.; Zembilgotov, A. G.; Tagantsev, A. K. Effect of Mechanical Boundary Conditions on Phase Diagrams of Epitaxial Ferroelectric Thin Films. *Phys. Rev. Lett.* 1998, *80,* 1988-1991.
[41] Noheda, B.; Gonzalo, J. A.; Cross, L. E.; Guo, R.; Park, S.-E.; Cox, D.E.; Shirane, G. Tetragonal-to-Monoclinic Phase Transition in a Ferroelectric Perovskite: the Structure of $PbZr_{0.52}Ti_{0.48}O_3$ *Phys. Rev. B.* 2000, *61,* 8687-8695.
[42] Noheda, B.; Cox, D. E.; Shirane, G. A Monoclinic Ferroelectric Phase in the $Pb(Zr_{1-x}Tix)O_3$ Solid Solution. *Appl Phys Lett.* 1999, *74,* 2059-2061.
[43] Noheda, B.; Cox, D. E.; Shirane, G.; Guo, R.; Jones, B.; Cross, L. E. Stability of the Monoclinic Phase in the Ferroelectric Perovskite $PbZr_{1-x}Ti_xO_3$. *Phys. Rev. B* 2000, *63,* 014103.
[44] Chynoweth, A. G. Dynamic Method for Measuring the Pyroelectric Effect with Special Reference to Barium Titanate. *J. Appl. Phys.* 1956, *27,* 78-84.
[45] Byer, R. L.; Roundy, C. B. Pyroelectric Coefficient Direct Measurement Technique and Application to a Nsec Response Time Detector. *IEEE Trans. Sonics & Ultrasonics* 1972, *3,* 333-338.
[46] Garn, L. E.; Sharp, E. J. Use of Low-Frequency Sinusoidal Temperature Waves to Separate Pyroelectric Currents from Nonpyroelectric Currents. Part I. Theory. *J. Appl. Phys.* 1982, *53,* 8974-8979.

CHAPTER 6 REFERENCES

[1] M. Kahn, *J. Am. Ceram. Soc.,* 1985, *68*, 623-68.
[2] G. W. Farnell, I. A. Cermak, P. Silverster, S. K. Wong, *IEEE Trans. Sonics Ultrason.* 1970, *17*, 188-195.
[3] A. V. Solnyshkin, I. L. Kislova, V. I. Shevyakov, A. A. Golishnikov and A. N. Belov, *Ferroelectrics,* 2019, *550*, 36-41.
[4] C. Mao, S. Yan, S. Cao, C. Yao, F. Cao, G. Wang, X. Dong, X. Hu and C. Yang, *J. Eur. Ceram. Soc.,* 2014, *34*, 2933-2939.
[5] A. R. Damodaran, J. D. Clarkson, Z. Hong, H. Liu, A. K. Yadav, C. T. Nelson, S.-L. Hsu, M. R. McCarter, K.-D. Park, V. Kravtsov, A. Farhan, Y. Dong, Z. Cai, H. Zhou, P. Aguado-Puente, P. Garcia-Fernandez, J. Iniquez, J. Junquera, A. Scholl, M. B. Raschke, L.-Q. Chen, D. D. Fong, R. Ramesh and L. W. Martin, *Nat. Mater.* 2017, *16*, 1003-1009.
[6] G.-Y. Kim, K. Chu, K.-D. Sung, H.-S. Lee, S.-D. Kim, K. Song, T. Choi, J. Lee, J. P. Buban, S.-Y. Yoon, K.-H. Kim, C.-H. Yang and S.-Y. Choi, *APL Mater.* 2017, *5*, 066104.
[7] A. R. S. Pandya, J. C. Agar, Y. Cao, R. K. Vasudevan, R. Xu, s. Saremi, Q. Li, J. Kim, M. R. McCarter, L. R. Dedon, T. Angsten, N. Balke, S. Jesse, M. Asta, S. V. Kalinin and L. W. Martin, *Adv. Mater.* 2017, *29*, 1702069.
[8] H. J. Lee, t. Shinizu, H. Funakubo, Y. Imai, O. Sakata, S. H. Hwang, T. Y. Kim, C. Yoon, C. Dai, L. Q. Chen, S. Y. Lee and J. Y. Jo, *Phys. Rev. Lett.* 2019, *123*, 217601.
[9] Z. Li, M. Grimsditch, X. Xu, S.-K. Chan, *Ferroelectrics*, 1993, *141*, 313.
[10] J. Karthik, A. R. Damodaran, L. W. Martin, *Adv. Mater.*, 2012, *24*, 1610-1615.
[11] Z.-G. Ban and S. P. Alpay, *Appl. Phys. Lett.* 2003, *82*, 3499-3501.

[12] J. Zhang, M. W. Cole and S. P. Alpay, *J. Appl. Phys.* **2010**, *108*, 054103.
[13] M. T. Kesim, J. Zhang, S. Trolier-McKinstry, J. V. Mantese, R. W. Whatmore and S. P. Alpay, *J. Appl. Phys.* **2013**, 114, 204101.
[14] D. Pesquera, E. Parsonnet, A. Qualls, R. Xu, A. J. Gubser, J. Kim, Y. Jiang, G. Velarde, Y.-L. Huang, H. Y. Hwang, R. Ramesh and L. W. Martin, *Adv. Mater.* **2020**, *32*, 2003780.
[15] Y. Guo, D. Akai, K. Swada and M. Ishida, *Appl. Phys. Lett.* **2007**, 90, 232908.
[16] G. E. Stan, M. Botea, G. A Boni, I. Pintilie and L. Pintilie, *Appl. Surf. Sci.* **2015**, 353, 1195.
[17] J.-S. Ko, W. Liu and W. Zhu, *Sensor Actuat. A-Phys.* **2001**, 93, 117.
[18] D. L. Polla, C.-P. Ye and T. Tamagawa, *Appl. Phys. Lett.* **1991**, 59, 3539.
[19] L. Zhang and R. Engel-Herbert, *Phys. Status Solidi RRL,* **2014**, *8*, 917-923.

CHAPTER 7 REFERENCES

[1] S. Das, A. Ghosh, M. R. McCarter, S.-L. Hsu, Y.-L. Tang, A. R. Damodaran, R. Ramesh and L. W. Martin, APL Mater. **6**, 100901 (2018).
[2] S. Chen, S. Yuan, Z. Hou, Y. Tang, J. Zhang, T. Wang, K. Li, W. Zhao, X. Liu, L. Chen, L. W. Martin and Z. Chen, Adv. Mater. 2000857 (2020).
[3] I. I. Naumov, L. Bellaiche and H. Fu, Nature **432**, 737-740 (2004).
[4] S. Prosandeev, I. Ponomareva, I. Naumov, I. Kornev and L. Bellaiche, J. Phys.: Condens. Matter **20**, 193201 (2008).
[5] T. Castan, A. Planes and A. Saxena, Phys. Rev. B. **85**, 144429 (2012).
[6] C.-J. Hus, S. M. Sandoval, K. P. Wetzlar and G. P. Carman, J. Appl. Phys. **110**, 123923 (2011).
[7] S. Pandya, J. D. Wilbur, B. Bhatia, A. R. Damodaran, C. Monachon, A. Dasgupta, W. P. King, C. Dames and L. W. Martin, Phys. Rev. Appl. **7**, 034025 (2017).
[8] A. Greppmair, N. Galfe, K. Amend, M. Stutzmann and M. S. Brandt, Rev. Sci. Instrum. **90**, 044903 (2019).
[9] D. Davidovikj, D. J. Groenendijk, a. M. R. V. L. Monteiro, A. Dijkhoff, D. Afanasiev, H. S. J. van der Zant, Y. Huang, E. van Heumen, A. D. Caviglia and P. G. Steeneken, Nature **3**, 163 (2020).
[10] Y. Ivry, V. Lyahovitskaya, I. Zon, I. Lubomirsky, E. Wachtel and A. L. Roytburd, *Appl. Phys. Lett.* **90**, 172905 (2007).
[11] S. Lisenkov, B. K. Mani, J. Cuozzo and I. Ponomareva, Phys. Rev. B. **93**, 064108 (2016).
[12] Y. Liu, I. C. Infante, X. Lou, L. Bellaiche, J. F. Scott and B. Dkhil, Adv. Mater. **26**, 6132-6137 (2014).
[13] H. Khassaf, T. Patel, R. J. Herbert and S. P. Alpay, J. Appl. Phys. **123**, 024102 (2018).
[14] D. Pesquera, E. Parsonnet, A. Qualls, R. Xu, A. J. Gubser, J. Kim, Y. Jiang, G. Velarde, Y.-L. Huang, H. Y. Hwang, R. Ramesh and Lane W. Martin, *Adv. Mater.* **32**, 2003780 (2020).